NBS TECHNICAL NOTE 1117

U.S. DEPARTMENT OF COMMERCE / National Bureau of Standards

NBS Reactor: Summary of Activities July 1978 to June 1979

NATIONAL BUREAU OF STANDARDS

The National Bureau of Standards[1] was established by an act of Congress on March 3, 1901. The Bureau's overall goal is to strengthen and advance the Nation's science and technology and facilitate their effective application for public benefit. To this end, the Bureau conducts research and provides: (1) a basis for the Nation's physical measurement system, (2) scientific and technological services for industry and government, (3) a technical basis for equity in trade, and (4) technical services to promote public safety. The Bureau's technical work is performed by the National Measurement Laboratory, the National Engineering Laboratory, and the Institute for Computer Sciences and Technology.

THE NATIONAL MEASUREMENT LABORATORY provides the national system of physical and chemical and materials measurement; coordinates the system with measurement systems of other nations and furnishes essential services leading to accurate and uniform physical and chemical measurement throughout the Nation's scientific community, industry, and commerce; conducts materials research leading to improved methods of measurement, standards, and data on the properties of materials needed by industry, commerce, educational institutions, and Government; provides advisory and research services to other Government agencies; develops, produces, and distributes Standard Reference Materials; and provides calibration services. The Laboratory consists of the following centers:

Absolute Physical Quantities[2] — Radiation Research — Thermodynamics and Molecular Science — Analytical Chemistry — Materials Science.

THE NATIONAL ENGINEERING LABORATORY provides technology and technical services to the public and private sectors to address national needs and to solve national problems; conducts research in engineering and applied science in support of these efforts; builds and maintains competence in the necessary disciplines required to carry out this research and technical service; develops engineering data and measurement capabilities; provides engineering measurement traceability services; develops test methods and proposes engineering standards and code changes; develops and proposes new engineering practices; and develops and improves mechanisms to transfer results of its research to the ultimate user. The Laboratory consists of the following centers:

Applied Mathematics — Electronics and Electrical Engineering[2] — Mechanical Engineering and Process Technology[2] — Building Technology — Fire Research — Consumer Product Technology — Field Methods.

THE INSTITUTE FOR COMPUTER SCIENCES AND TECHNOLOGY conducts research and provides scientific and technical services to aid Federal agencies in the selection, acquisition, application, and use of computer technology to improve effectiveness and economy in Government operations in accordance with Public Law 89-306 (40 U.S.C. 759), relevant Executive Orders, and other directives; carries out this mission by managing the Federal Information Processing Standards Program, developing Federal ADP standards guidelines, and managing Federal participation in ADP voluntary standardization activities; provides scientific and technological advisory services and assistance to Federal agencies; and provides the technical foundation for computer-related policies of the Federal Government. The Institute consists of the following centers:

Programming Science and Technology — Computer Systems Engineering.

[1] Headquarters and Laboratories at Gaithersburg, MD, unless otherwise noted;
mailing address Washington, DC 20234.

[2] Some divisions within the center are located at Boulder, CO 80303.

NBS Reactor: Summary of Activities July 1978 to June 1979

Frederick J. Shorten, Editor

Reactor Radiation Division
National Measurement Laboratory
National Bureau of Standards
Washington, DC 20234

t. Technical note.

U.S. DEPARTMENT OF COMMERCE, Philip M. Klutznick, Secretary
Luther H. Hodges, Jr., Deputy Secretary
Jordan J. Baruch, Assistant Secretary for Productivity, Technology, and Innovation
NATIONAL BUREAU OF STANDARDS, Ernest Ambler, Director

Issued April 1980

National Bureau of Standards Technical Note 1117
Nat. Bur. Stand. (U.S.), Tech. Note 1117, 236 pages (Apr. 1980)
CODEN: NBTNAE

U.S. GOVERNMENT PRINTING OFFICE
WASHINGTON: 1980

For sale by the Superintendent of Documents, U.S. Government Printing Office
Washington, D.C. 20402

FOREWORD

The National Bureau of Standards Reactor was built not only to serve the needs of the NBS but also those of other government agencies and the greater Washington Scientific Community. The Reactor Radiation Division was established to operate the reactor and to foster its scientific and technological use. Toward this end, the Division has a small nucleus of scientists experienced in the use of reactors for a wide range of scientific and technical problems. In addition to pursuing their own research and developing sophisticated experimental facilities, they actively seek out and encourage collaboration with other scientists engaged in challenging programs whose work can benefit from use of the reactor, but who as yet do not have the reactor experience necessary to take full advantage of the facilities available. The Division also provides irradiation services to a wide variety of users as well as engineering and other technical services.

The reactor operates at 10 MW and is designed to provide more than 25 experimental facilities ranging from intense neutron beams to extensive irradiation facilities, making it one of the most versatile high flux research reactors in the country. Thus it is able to serve a large number of scientists and engineers in a broad range of activities both within and outside the NBS.

This report attempts to summarize all the work done which is dependent on the reactor including a large number of programs outside the Division. The first section summarizes those programs based primarily on Reactor Radiation Division (RRD) initiatives whereas the second and third sections summarize collaborative programs between RRD scientists and other NBS or non-NBS scientists respectively. The fourth section summarizes NBS work originating entirely outside the RRD which requires no collaboration with RRD scientists. The section entitled, "Service Programs" covers those programs originating outside NBS but for which RRD provides irradiation services. The remaining sections are self-explanatory.

FOREWORD

Appreciation is extended to F. J. Shorten of the Reactor Radiation Division for his extensive contributions to the editing, organization and preparation of this report, and T. Mangum, L. Sprecher, C. Freedman, and S. Long for efforts in typing manuscripts.

R. S. Carter

R. S. Carter
Chief, Reactor Radiation Division
National Bureau of Standards

ABSTRACT

This report summarizes all those programs which depend on the NBS reactor. It covers the period from July 1978 through June 1979. The programs range from the use of neutron beams to study the structure and dynamics of materials through nuclear physics and neutron standards to sample irradiations for activation analysis, isotope production, radiation effects studies, neutron radiography, and nondestructive evaluations.

Key words: Activation analysis; crystal structure; diffraction; isotopes; molecular dynamics; neutron; neutron radiography; nondestructive evaluation; nuclear reactor; radiation.

TABLE OF CONTENTS

TABLE OF CONTENTS

TABLE OF CONTENTS

A. REACTOR RADIATION DIVISION PROGRAMS

HYDROGEN IN METALS

J. M. Rowe and J. J. Rush

and

A. Magerl
(University of Munich, Munich, Germany)

and

A. Maeland
(Allied Chemical Corporation, Morristown, NJ)

We have begun a detailed study of the dynamics of Nb metal containing hydrogen and deuterium. Interest is focussed on both acoustic and optic modes and on the effects of nitrogen and oxygen traps. In addition, we have completed the first experiments to compare the scattering from amorphous and crystalline metals containing hydrogen in an attempt to probe the local environment of the hydrogen atoms. The results, which demonstrate conclusively the great potential of the neutron scattering technique, are shown in figure 1 where the scattering from amorphous and crystalline TiCu are compared. As is obvious from the figure, the neutron spectrum from the optic modes is quite sharp and well defined for the crystalline material, while in the amorphous material this spectrum is broadened considerably, showing the effects of fluctuations in local symmetry. These measurements have been extended to amorphous and crystalline Ti_2CuH_x . In addition, we have measured the diffraction pattern of glassy TiCu and TiCuD up to a momentum transfer Q of 15, to obtain more information on the structure of these prototype glasses. Detailed theoretical analysis of these results is continuing.

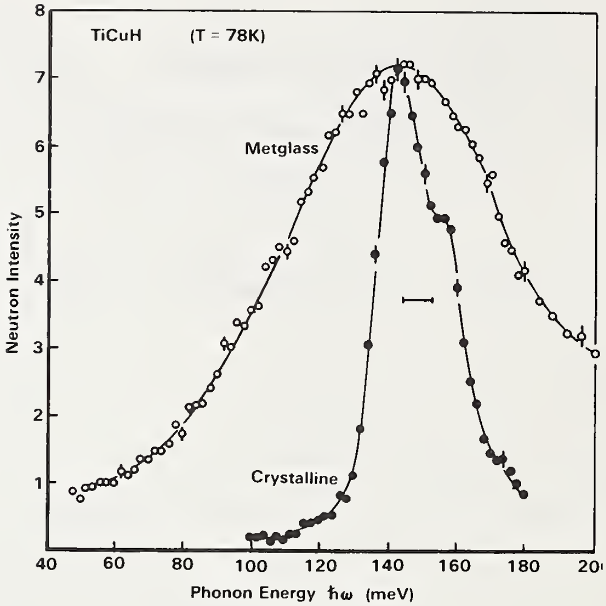

Figure 1. Neutron energy loss spectra for TiCuH glass and polycrystal at 78 °K.

DIFFUSE SCATTERING IN Nb METAL CONTAINING IMPURITIES

J. M. Rowe

and

A. Magerl
(University of Munich, Munich, Germany)

We have completed diffuse elastic scattering measurements on a nominally pure Nb crystal (< 20 ppm by weight) and a Nb crystal containing 225 ppm nitrogen atoms. From these measurements, we conclude that nitrogen impurities lead to strong diffuse scattering at approximately (4/3, 4/3, 4/3) and suggest that earlier observations of such scattering in nominally pure Nb can be accounted for by this effect. Similar effects were observed for Nb crystals loaded with oxygen impurities.

STUDY OF VIBRATIONAL SPECTROSCOPY OF CHEMISORBED SPECIES ON NICKEL BY NEUTRON INELASTIC SCATTERING

J. J. Rush

and

R. D. Kelley, T. E. Madey, and R. Kavanagh
(Surface Science Division)

During the past year we have initiated a program with the Surface Science Division to develop and apply neutron scattering methods for the study of absorbed species and chemical reactions on fine-particle catalysts. This research is aimed at fundamental studies of atomic and molecular species bound on surfaces, as well as studies of reactions under gaseous environments which are relevant in catalytic processes.

In our initial experiments, we have measured neutron spectra between 40 and 180 meV for hydrogen chemisorbed on Raney nickel catalyst, for coadsorbed CO and H_2, for hydrogen reacted with an "activated carbon" surface, and for catalytic fragmentation of ethylene. These results have clearly demonstrated the potential of the neutron scattering method and have allowed us to explore the type, treatment, and purity of nickel-based catalysts required to minimize background peaks in the spectra. Neutron scattering measurements were made using the BT-4 triple-axis spectrometer and a beryllium filter analyzer. Samples were loaded and reacted in gas tight stainless steel sample holders. Background corrected neutron spectra measured at 78 °K for several combinations of surface reactants on Raney nickel ("full" monolayers, approximately 2 at % surface species) are shown in figures 1 and 2. The spectra for chemisorbed H on Ni show three prominent features which are assigned to H bound to 4 Ni atoms on the surface (78 meV), and to 2- or 3-fold coordinated H (peaks at 119 and 141 meV). The relative intensity of the peaks indicates that the H species represented by the 78 meV feature (which is also seen as the prominent feature at 75 meV in electron

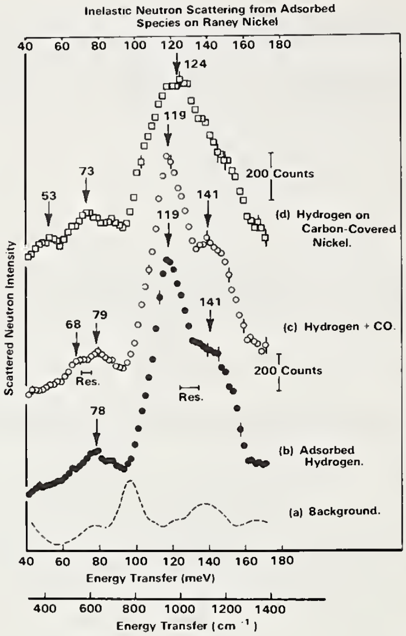

Figure 1. Neutron scattering spectra from adsorbed species on Raney nickel.

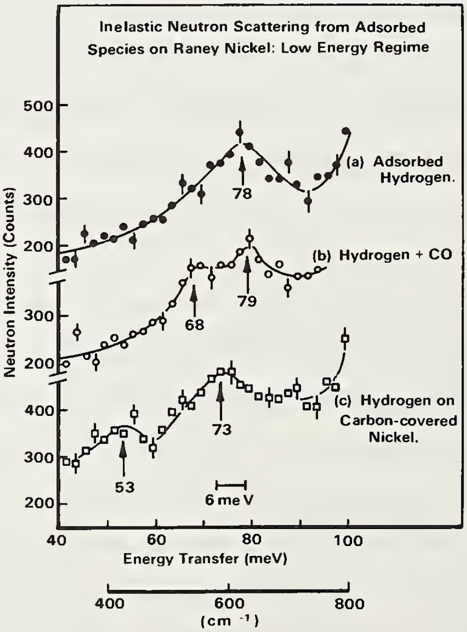

Figure 2. Neutron scattering spectra from adsorbed species on Raney nickel for the low energy regime.

energy loss scattering on the 100 planes of Ni crystals) is a relatively minor fraction of the adsorbed H atoms on the catalytic powder. The high energy regime (> 100 meV) of the spectra for H+CO shows very little change from the pure H monolayer spectrum indicating that a substantial fraction of chemisorbed H is neither perturbed or displaced by CO. The H+ carbon covered nickel spectrum, however, shows significant differences, including a very broad band at higher energies, presumably reflecting a distribution of vibrational frequencies associated with bending and deformation modes of CH_x species produced on the surface.

In figure 2 the low energy region of the neutron spectra is shown. The spectrum for H_2+CO on nickel shows emergence of a second maximum at 68 meV in this regime which provides clear evidence of a CO-H interaction on the surface. The H on carbon-covered Ni spectrum is again distinctly different showing features at 53 and 73 meV which are probably associated with Ni-C stretching vibrations of the Ni-CH_x complexes formed on the surface.

We are currently involved in a considerable expansion of this neutron scattering work on surfaces with the Surface Science Division, including development of a new high-intensity, high-resolution analyzer for neutron spectroscopic studies, design of special temperature controlled sample containment systems for measurements from 5 °K to 500 °K, and preparation of specially treated Ni and other fine-particle catalysts. We are also exploring the use of large and small angle neutron diffraction facilities for in situ studies of catalyst particle sizes and molecular arrangements on the surface.

INELASTIC NEUTRON SCATTERING STUDIES OF MIXED ALKALI HALIDE-ALKALI CYANIDE CRYSTALS

J. M. Rowe and J. J. Rush

and

S. Susman and D. Hinks
(Argonne National Laboratory, Argonne, IL)

and

K. H. Michel
(UIA, Antwerp, Belgium)

We have continued both theoretical and experimental efforts on the mixed KCN-KBr system. Most recently, we have measured the neutron scattering from a crystal of $KCN_{.5}\,KBr_{.5}$ as a function of temperature between 4 K and 300 K. The neutron scattering lineshapes are shown in figure 1. As can be seen, the behavior is similar to that discussed for $KCN_{.25}\,KBr_{.75}$ last year -- namely, the phonon energy decreases as T decreases from 300 to approximately 90 K, then becomes overdamped and increases again from 90 K down to 12 K. At the same time, a peak appears at zero energy transfer and grows in intensity from approximately 100 K down to 12 K.

This behavior is summarized in figure 2 where both the square of the phonon energy and the reciprocal of the elastic intensity are plotted as a function of temperature. When this phenomenon was first observed in $KCN_{.25}\,KBr_{.75}$, we ascribed it to the slowing down of $(CN)^-$ reorientations, which leads to a "slow reorientation" regime at low temperatures, and a strong central peak in the theory of Michel and coworkers. However, more careful analysis of the new data convinces us that this explanation cannot be correct. Although the theoretical analysis of these results is incomplete, it leads us to believe that we are seeing a collective slowing down or "freezing" of $(CN)^-$ orientations in a manner somewhat

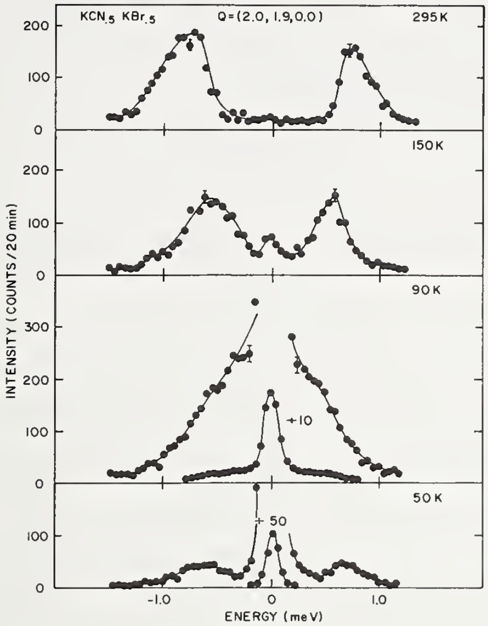

Figure 1. Neutron scattering lineshapes measured for a 100 TA phonon 1/10 the way to the zone boundary in KCN$_{.5}$ KBr$_{.5}$.

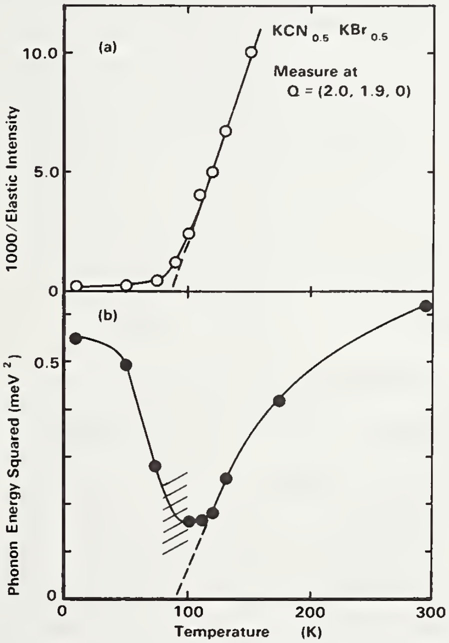

Figure 2. Phonon energy squared and reciprocal elastic intensity in KCN$_{.5}$ KBr$_{.5}$ as a function of temperature.

analogous to the magnetic spin glass. There are, however, significant differences in the two kinds of systems which makes the analysis more complex. Work on this aspect continues.

MODIFICATIONS TO THE RIETVELD POWDER REFINEMENT PROGRAM

E. Prince

The technique of total pattern analysis, developed originally by H. M. Rietveld[1], is a powerful technique for extracting structural information from powder diffraction data. The installation of the 5-detector powder diffractometer made it necessary to make some changes in the original program so it could be used to analyze multidetector data. At the same time a number of other modifications were made to improve the performance of the program.

1. The sum-of-squares that is minimized includes all data from all detectors. The profile preparation program applies the relative scale factor to the observed data, while the profile calculation allows for the small differences in zero correction for the different detectors. The output includes observed and calculated intensities for individual reflections. So that reflections occurring in the overlap regions will not be counted twice, only the last 20° range is included in this computation for all detectors after the first.

2. The original program provided for subtraction of background during preparation of the intensity data. This assumes, in effect, that the background is perfectly known for all points in the pattern. To the extent that the background is not perfectly known, this assumption introduces a bias into the intensity data which will carry over to a corresponding bias in the estimates of the parameters. There will also be a tendency to overestimate the precision of the

diffracted intensity. The program has been modified to include background explicity in the model as a straight line with a finite slope for each of the five detectors. The program will also work for single detector data by dividing the pattern into up to five segments. In order to produce correct output of the diffracted intensity data all segments except the lowest angle one should be shorter than 20°.

3. The original program allowed for the inclusion of constraints on the refined parameters by using the technique of Lagrange undetermined multipliers. This technique, which adds a row and a column to the Hessian matrix for each constraint relation, is computationally inefficient. The program has been modified to apply constraints directly through evaluation of the partial derivatives with respect to the independent parameters. The number of constraints that may be applied is effectively unlimited.

4. The system developed for the application of shape constraints and rigid-body thermal constraints to single crystal refinement[2] has been incorporated in the powder refinement program and used on several problems, with results that indicate that the use of appropriate models can greatly enhance the power of the total pattern refinement technique.

---

1. H. M. Rietveld, *J. Appl. Cryst.*, 2, 65 (1969)

2. L. W. Finger & E. Prince, *NBS Tech Note 854* (1975)

USE OF RIETVELD PROFILE REFINEMENT FOR MAGNETIC SYSTEMS

G. E. Fish, J. J. Rhyne, E. Prince, and A. Santoro

The method of total profile analysis of neutron powder diffraction data has become an extremely important crystallographic tool in the last few years. In many cases, single crystals suitable for diffraction are unavailable, yet the powder pattern is not amenable to conventional analysis using intensities because of severe overlap of adjacent peaks.

The accuracy of the Rietveld method for structural crystallography has been extensively studied by comparison of profile refinements in various laboratories of data taken on identically prepared samples and by comparison with single crystal and conventional powder intensity data. Even though the Rietveld program and its successors allow the simultaneous refinement of crystallographic and magnetic structure, little attention has been paid as yet to the accuracy of magnetic moments thus obtained.

The rare earth intermetallic compounds RM_2 provide an ideal series of test cases for magnetic profile refinement. For a wide variety of metals M, the compounds have the cubic Laves phase (C15) structure in which both R and M occupy special positions. By appropriate selection of R and M, samples can be prepared with either or both species magnetic and magnetic ordering temperatures widely varying. In many cases, accurate magnetic data on both powders and single crystals have been taken by complementary techniques such as bulk magnetization and Mössbauer effect.

We have high-resolution neutron powder diffraction patterns on samples of $HoFe_2$, YFe_2, $LuFe_2$, $HoAl_2$, and $TbNi_2$. Refinement of these data sets using the Rietveld method are in progress. We find that, in general, the magnetic moments determined are strongly correlated with the thermal parameters and with each other in a multi-component system. The case of $HoAl_2$ is illustrative of the problems encountered. Data were taken in both paramagnetic (T=78K) and ordered (T=4K) phases. Bulk magnetization data show ferromagnetic ordering of the Ho spins at $T_c \approx 30K$ with a 4K moment of ∿ 9.3 μ_B. The magnetic moment determined from the intensity of the (111) and (220) powder peaks above and below T_c agreed within 0.15 μ_B. The values of B_{Ho} and B_A at 4K are unphysically large and μ_{Ho} is too small. Both the magnetic form factor and the thermal factors decrease with momentum transfer $Q = 4\pi \sin \Theta/\lambda$, so the observed correlations in the fit are not unexpected.

Studies are in progress to determine if these correlations can be systematically reduced by some different fitting procedure. We are also exploring the possibility that the breakdown of the Gaussian lineshape approximation, known to be most severe at low 2Θ where the magnetic contribution is strongest, may result in the anomalous determination of magnetic moments.

THE 5-DETECTOR NEUTRON POWDER DIFFRACTOMETER

E. Prince and A. Santoro

The multidetector powder diffractometer described in the 1978 progress report[1] was installed at BT-1 in the autumn of 1978. Preliminary calibration of the instrument was carried out using a standard sample of Al_2O_3. Initially a wavelength of about 1.2 A was used so that it would be possible to scan a range of the powder pattern containing a number of intense and well resolved peaks with each of the five detectors in turn. Using this information the relative scale factors and precise corrections to the nominally 20° angles between collimator axes were determined for all detectors. Table 1 is a summary of these calibration values. Next, the instrument was set to a longer wavelength for better resolution of powder patterns and a full powder pattern was collected for Al_2O_3. Analysis of this pattern yielded an accurate value for the wavelength, 1.5420(2) Å. Figure 1 is a photograph of the instrument.

Table 1. Calibration summary.

Detector number	Scale Factor	Angle Correction
1	1.026	-.0390°
2	1.035	.0000°
3	0.976	-.0025°
4	0.968	+.0095°
5	1.000	+.0158°

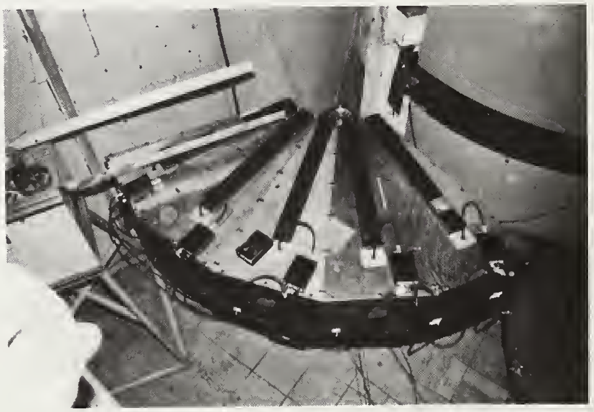

Figure 1. View of the 5 detector powder diffractometer.

---

1. E. Prince and A. Santoro, *NBS Tech. Note* 995, 10 (1979)

STUDIES OF RIBONUCLEASE-A BY X-RAY AND NEUTRON DIFFRACTION

Alexander Wlodawer

Structure of single crystals of ribonuclease-A is being investigated in collaboration with the Laboratory of Molecular Biology, NIAMDD, NIH. This program, initiated in 1975, is now yielding first biologically significant results. Conditions for the growth of large crystals of ribonuclease-A were found by J. Norvell. Crystals used for both x-ray and neutron studies were transferred in stages to synthetic mother liquor containing 55% of fully deuterated tertiary butanol (d_{10}, Aldrich), adjusted to pH = 5.3 with sodium deuteroxide. The mother liquor was essentially hydrogen-free. The soaking time was about 6 months with several complete changes of solvent.

X-ray intensities to 2.5 Å resolution were measured on a diffractometer using ω step-scan and measuring individual backgrounds for each reflection. Two complete data sets were measured, each on one crystal. The data were merged, yielding R = 4.3% ($R = \Sigma|F_1 - F_2|\ \Sigma \overline{F}$).

Neutron diffraction data were collected using the flat-cone diffractometer at the National Bureau of Standards reactor (Prince, Wlodawer, and Santoro, 1978). The neutrons were monochromatized by reflection from a 5 x 10 cm graphite crystal of mosaic spread 40' and the wavelength was 1.68 Å. Neutron flux on the sample, measured by gold foil activation, was 6×10^6 neutrons/cm^2/sec.

Data to 2.8 Å resolution were collected using the diffractometer in equatorial geometry, neglecting intensities falling outside of the equatorial plane of the instrument. Each reflection was measured by ω scan 1.6° wide in 64 steps, with 10 steps on each side used as background. Reflections to 3.2 Å resolution were counted 10 minutes each and to 2.8 Å for 20 minutes. Two standard reflections were monitored with no change in intensity throughout data collection. A substantial number of the Friedel pairs were measured yielding R = 4.4% upon merging. Data were corrected

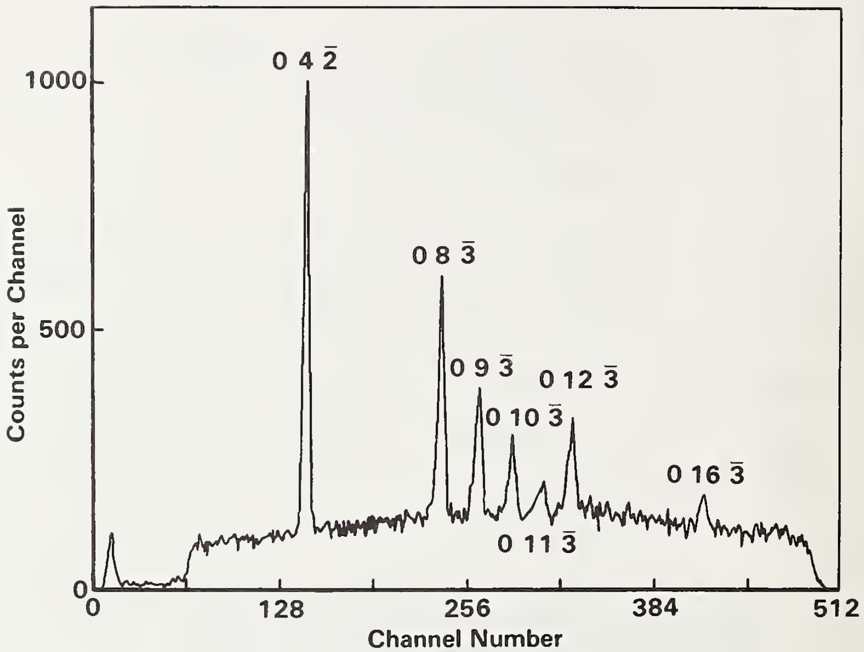

Figure 1. Example of a frame of output of the linear detector in flat-cone geometry. Seven reflections are clearly visible. Resolution for the channel 490 is 2.0 A.

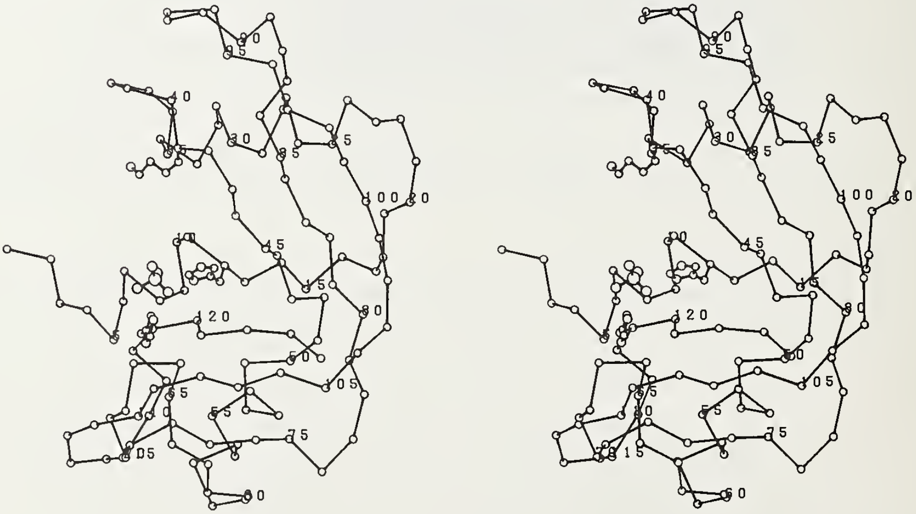

Figure 2. Stereo tracings of C_γ positions and the phosphate near the active site in the final model. Side chains of HIS-12, HIS-119 and LYS-41 are also marked.

for absorption, but the influence of neutrons with half wavelengths was neglected. The number of observed reflections ($F > 2\sigma$) was 2773, 87% of all reflections at 2.8 Å resolutions.

Another data set to 2 Å resolution was collected with the diffractometer operated in flat-cone geometry. Each layer of reflections was collected by rotation of the crystal around a axis, in order to limit the number of necessary scans by measuring the most densely populated planes. A complete 360° scan took 60 hours and ψ was incremented by 0.05° between measurements. Each general reflection was measured twice and special reflections four times. An example of a frame of the detector output is shown in figure 1. These data are still being processed.

Since no refined structure of ribonuclease-A was available, it was necessary to first refine a set of atomic coordinates based on x-ray structure factors. The restrained least-squares conjugate gradient procedure of Hendrickson and Konnert[2], as adapted for a minicomputer by A. Arnone (personal communication) and this author was used. One cycle of refinement for 4061 intensities observed between 10 and 2.5 Å and 951 atoms would take about 30 minutes with the average load on the computer, with a total of 24 hours of computer time necessary for the complete refinement process. Ribonuclease-S coordinates were rotated into the ribonuclease-A unit cell by minimizing the distances between C_α positions, using Carlisle's[3] coordinates as guide-posts. Since the C_α coordinates differed by as much as 15 Å for the residues adjacent to the area of proteolytic cleavage in ribonuclease-S, coordinates for residues 17 - 23 were taken directly from ribonuclease-A. Thirteen cycles of refinement of 3 Å data, followed by four cycles at 2.5 Å resolution lowered the R factor to 30.9%, with the root-mean-square (rms) deviation of bond lengths kept at .055 Å. Since the refinement would not continue from this point without manual intervention, rebuilding of the model was necessary. This was accomplished using computer graphics at the National Institutes of Health computer center. Program BILDER, was used to fit the coordinates to maps calculated using as coefficients either $(2F_o - F_c)$ or $(F_o - F_c)$, with about 8% of the atoms removed from phasing in each map in the latter case. It was necessary to make a number of corrections to the main chain, invert several peptide bonds by 180°, and to adjust many side chains. The process of rebuilding was followed by several more cycles of refinement and the procedure was repeated five times. An overall temperature factor of 6 $Å^2$ was applied throughout the refinement and no attempt to fit solvent molecules was made, even though a number of peaks due to water and/or butanol persisted in difference maps. Only a very obvious peak due to phosphate was fitted at final stages of the refinement.

After 48 cycles of refinement and five of manual chain adjustments the protein model is much improved. The R factor was lowered to 25.2% and the rms deviation of bond lengths from ideality is .042 Å. Only six amino acid side chains (out of 124) did not have sufficient density in (F_o - F_c) maps calculated after their contribution to phasing was removed. Another 30 side chains have minor breaks in density in maps contoured at 25% of the maximum, but could be unambiguously traced, while 88 side chains fit their respective densities very well. Figure 2 shows a stereo tracing of C_α positions of the final model.

Structure amplitudes obtained from deuterated ribonuclease crystals are quite different for the x-ray and neutron cases. Scaling of 2559 reflections observed in the two data sets for the resolution range of 10 - 2.8 Å yields R = 32.7%, with the discrepancies as large as 50% below 6 Å and quite uniform around 31% above that resolution.

Several ways of phasing neutron diffraction data have been proposed in the past. Schoenborn (1969) calculated Fourier maps of myoglobin at 2.8 Å resolution by applying x-ray phases directly to neutron structure amplitudes. It was estimated that the deviation from the "true" phases was 40°. An alternative approach was to calculate phases based on the positions of all non-hydrogen atoms, with the estimated deviation from the "true" phases being the same as in the former case. Both of these approaches were tried with the ribonuclease data. The average phase difference between phases calculated using x-ray and neutron scattering factors was only 16° and the maps calculated using either of the phase sets and observed neutron structure amplitude were virtually identical. These maps were also quite similar to a map calculated using x-ray phases and F's, which is not surprising in view of the predominant importance of phases in map calculations.

The agreement between observed neutron structure amplitudes and those calculated on the basis of non-hydrogen atom positions was fair, with R = 35.4%. This value falls in between the values for the initial and final x-ray model, indicating a good probability of successful refinement, even though almost half of all the atoms in the structure were hydrogens and were not used in structure factor calculations.

While both $F_o \cdot \alpha_c$ and $(2F_o - F_c) \cdot \alpha'_c$ neutron maps looked quite similar to the respective x-ray maps, this was not true for $(F_o - F'_c) \cdot \alpha'_c$ maps, in which F'_c and α'_c were calculated after about 8% of the chain was removed. These maps based on x-ray structure amplitudes were successfully used to adjust the model, but they were very difficult to interpret in the neutron case. Lowering the number of removed atoms did, however, improve the difference maps, and this technique appears to be least susceptible to the bias in the initial phase set. It appears that the most promising approach to the refinement of the neutron structure of ribonuclease is a procedure similar to the one used in the x-ray refinement, namely alternation of automated refinement and corrections based on partial maps. Initial positions of most of the hydrogen atoms can be predicted on the basis of the refined non-hydrogen atoms, and the decision between hydrogen and deuterium can be made by checking the difference Fourier map. Ultimately this can be treated as occupancy problems and the probability that a given atom is either hydrogen or deuterium can be incorporated as a refinable parameter. The refinement of neutron structure of ribonuclease is still in progress and will be reported in detail in the future, with preliminary account available[5].

---

1. Prince, E., Wlodawer, A. & Santoro, A., "Flat-cone Diffractometer Utilizing a Position-Sensitive Detector", *J. Appl. Cryst.* 11, 173-178(1978).

2. Hendrickson, W. A. & Konnert, J. H., "Stereochemically Restrained Cr Crystallographic Least-Squares Refinement of Macromolecular Structures", 1979 *Proceedings of Madras Symposium,* (to be published).

3. Carlisle, C. H. et al., "The Structure of Ribonuclease at 2.5 Å Resolution", *J. Mol. Biol.,* 85, 1-18(1974).

4. Schoenborn, B. P., "Neutron Diffraction Analysis of Myoglobin", *Nature (London)* 224, 143-146(1969).

5. Wlodawer, A., "Studies of Ribonuclease-A by X-ray and Neutron Diffraction", *Acta Cryst.,* submitted, (1979).

ABSORPTION CORRECTION FOR WEISSENBERG DIFFRACTOMETERS

A. Santoro and Alexander Wlodawer

The main problem in extending empirical corrections to Weissenberg methods other than the equi-inclination arises because, in these configurations, incident and diffracted beams of a generic reflection $\underset{\sim}{h}$ do not lie on the same diffraction cone. In these cases, we may adopt two strategies to make the beam directions of the absorption reflection $\underset{\sim}{k}$ as close as possible to the beam directions of the reflection $\underset{\sim}{h}$ under study, i.e., (i) we may choose as reflection $\underset{\sim}{k}$ one for which incident and diffracted beams lie on diffraction cones intermediate to those of the incident and diffracted beams of $\underset{\sim}{h}$, or (ii) we may use two reflections $\underset{\sim}{k}$ to make the correction, one, $\underset{\sim}{k}_i$, such that its diffraction cone is the same as that of the incident beam of $\underset{\sim}{h}$ (or as close as possible to it), and the other, $\underset{\sim}{k}_j$, such that its diffraction cone is the same as that of the diffracted beam of $\underset{\sim}{h}$ (or as close as possible to it). For the flat-cone geometry, therefore, $\underset{\sim}{k}_i$ is located on the level twice that of $\underset{\sim}{h}$, and $\underset{\sim}{k}_j$ is located on a level as close as possible to the level zero.

The extension of the method of North, Phillips, and Mathews[1] to case (i) is trivial. For case (ii), an equation can be written

$$T'\ (\underset{\sim}{h},\omega,\chi,\ \phi) \approx \left[\frac{I_1(\underset{\sim}{k}_I)}{2I_{\max}(\underset{\sim}{k}_i)} + \frac{I_2(\underset{\sim}{k}_j)}{2I_{\max}(\underset{\sim}{k}_j)}\right] C \qquad (1)$$

where $I_1(\underset{\sim}{k}_i)\,[I_2(\underset{\sim}{k}_j)]$ is the intensity of $\underset{\sim}{k}_i\,[\underset{\sim}{k}_j]$ measured for that orientation of the crystal for which the projection of the mean direction of $\underset{\sim}{k}_i\,(\underset{\sim}{k}_j)$ is coincident with the projection of the incident (diffracted) beam of $\underset{\sim}{h}$. The factor C appearing in equation (1) is constant for each level and does not need to be determined if only the intensities in one reciprocal lattice level are being considered. However, if three-dimensional data are corrected with different combinations of $\underset{\sim}{k}_i$ and $\underset{\sim}{k}_j$, then the

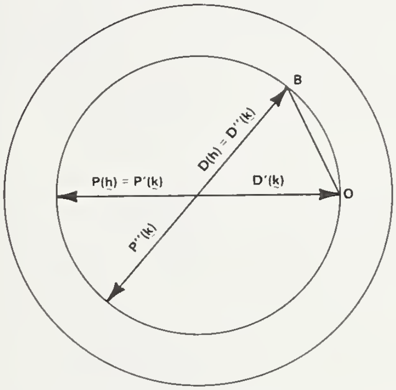

Figure 1. Method of North et al. (1968) for the equi-inclination geometry. The rotation axis of the crystal is perpendicular to the plane of figure at O. $P(\underset{\sim}{h})$ and $D(\underset{\sim}{h})$ are the primary and diffracted beams of the reflection $\underset{\sim}{h}$ under study, corresponding to the reciprocal node B. $P'(\underset{\sim}{k})$ and $D'(\underset{\sim}{k})$ and $P''(\underset{\sim}{k})$ and $D''(\underset{\sim}{k})$ are the projections on the absorption plane of the primary and diffracted beams of the absorption reflection $\underset{\sim}{k}$ for the two orientations of the crystal for which the intensities $I_1(\underset{\sim}{k})$ and $I_2(\underset{\sim}{k})$ are measured.

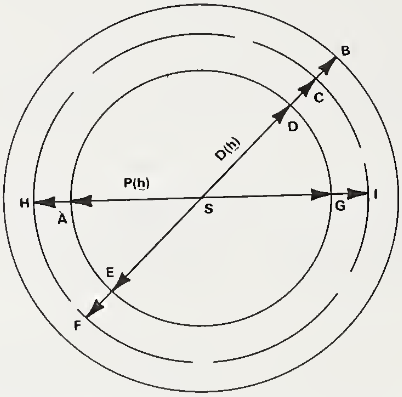

Figure 2. Method of North et al. (1968) for the flat-cone geometry. The rotation axis of the crystal is perpendicular to the plane figure at G. AS and SB are the incident and diffracted beams of the reflection $\underset{\sim}{h}$ under study, located on level ℓ. The empirical transmission is evaluated from the intensities of two absorption reflections. AS and SG are the incident and diffracted beams of the first of them, located on level 2ℓ, and FS and SC are those of the second, located on a level as close as possible to level zero.

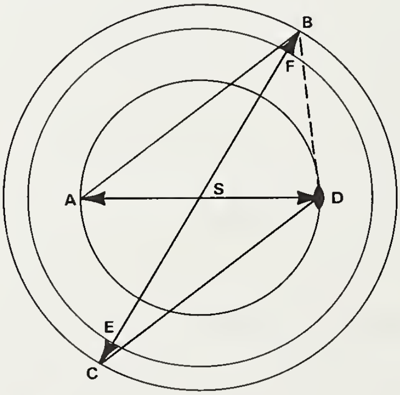

Figure 3. Method of Lee and Ruble (1977) in flat-cone geometry. AS and SB are incident and diffracted beams of reflection $\underset{\sim}{h}$, and DS and SC those of $\underset{\sim}{h}'$, symmetrically equivalent to $\underset{\sim}{h}$. AS and SD are the incident and diffracted beams of the first absorption reflection, and ES and SF those of the second. The levels of the absorption reflections are chosen as in the previous case.

resulting intensities have to be put on the same scale. This can be accomplished with the following procedure.

Let us indicate with $\underset{\sim}{h}_1, \underset{\sim}{h}_2, \ldots, \underset{\sim}{h}_n$ reflections located on levels 1, 2, . . ., n. We may write

$$I_{obs}(\underset{\sim}{h}_s) = T'(\underset{\sim}{h}_s)\, S(\underset{\sim}{h}_s)\, I_o(\underset{\sim}{h}_s) = T''(\underset{\sim}{h}_s)\, C_s\, S(\underset{\sim}{h}_s) I_o(\underset{\sim}{h}_s) \quad (*) \qquad (2)$$

i.e.

$$I_o(\underset{\sim}{h}_s)\, C_s = b_s = I_{obs}(\underset{\sim}{h}_s) /\, T''(\underset{\sim}{h}_s)\, S(\underset{\sim}{h}_s) \qquad (3)$$

The quantities $b_1, b_2, \ldots, b_n$ are known. If we put

$$C_{1r} = C_1/C_r, \ldots, C_{nr} = C_n/C_r \qquad (4)$$

Equation 3 can be written

$$C_r I_o(\underset{\sim}{h}_s) = b_s/C_{sr} \qquad (5)$$

In equation 5, r indicates some convenient level chosen as a reference for the whole set of intensities. Therefore, C_r is a factor by which all intensities are multiplied and, consequently, can be included in the overall scale factor. The quantity C_{sr}, characteristic of level s, can be estimated with the procedure detailed elsewhere[4].

Lee and Ruble[2] have proposed a method of absorption correction which is particularly valuable in those cases in which the procedure of (1) fails because the sample shape does not have two-fold symmetry about the rotation axis. This method is restricted to crystals possessing at least a two-fold axis of crystallographic symmetry and is applicable to the Weissenberg geometry only if the symmetry axis is selected as the rotation axis. If we adopt the approximation given by Kopfman and Huber[3] we may write

$$\begin{aligned} I_{obs}(\underset{\sim}{h}) &= R(AS)\ R(SB)\ S(\underset{\sim}{h})\ I_o(\underset{\sim}{h}) \\ I_{obs}(\underset{\sim}{h}') &= R(DS)\ R(SC)\ S(\underset{\sim}{h})\ I_o(\underset{\sim}{h}) \end{aligned} \tag{6}$$

Let us now choose as absorption reflection $\underset{\sim}{k}_i$ the axial reflection whose beam directions lie on the diffraction cone of AS and SD and let us measure its intensity for that orientation of the crystal for which we may write

$$I_{obs}(\underset{\sim}{k}_i) = R(AS)\ R(DS)\ S(\underset{\sim}{k}_i)\ I_o(\underset{\sim}{k}_i) \tag{7}$$

As absorption reflection $\underset{\sim}{k}_j$ let us select the axial reflection located on the closest level to the level zero and let us measure its intensity so that we may write

$$\begin{aligned} I_{obs}(\underset{\sim}{k}_j) &= R(ES)\ R(SF)\ S(\underset{\sim}{k}_j)\ I_o(\underset{\sim}{k}_j) \\ &\simeq R(SC)\ R(SB)\ S(\underset{\sim}{k}_j)\ I_o(\underset{\sim}{k}_j) \end{aligned} \tag{8}$$

Combining equations (6), (7), and (8), we obtain

$$I_o^2(\underset{\sim}{h}) = \frac{I_{obs}(\underset{\sim}{h})\ I_{obs}(\underset{\sim}{h}')}{I_{obs}(\underset{\sim}{k}_i)\ I_{obs}(\underset{\sim}{k}_j)}\ \frac{S(\underset{\sim}{k}_i)\ S(\underset{\sim}{k}_j)}{S^2(\underset{\sim}{h})}\ I_o(\underset{\sim}{k}_i)\ I_o\ (\underset{\sim}{k}_j) \tag{9}$$

Equation (9) is the equivalent, in flat-cone geometry, of equation (6) derived by (2). The term $I_o(\underset{\sim}{k}_i)\ I_o\ (\underset{\sim}{k}_j)$ is unknown and constant for each level. If the intensities to be corrected belong to different levels, this term has to be evaluated. The procedure to do this is given in (4). Similarly, this reference can be used to calculate the rotations needed to orient the crystal for the intensity measurements required for evaluation equations (1) and (9), as well as numerical tests of the method.

---

1. North A. C. T., Phillips D. C. and Mathews, F. S. (1968) *Acta Cryst.* A24, 351-359.
2. Lee, B. and Ruble, J. R. (1977) *Acta Cryst.* A33, 629-637.
3. Kopfman, G. and Huber, R. (1968) *Acta Cryst.* A24, 348-351.
4. Santoro, A. and Wlodawer, A. (1979) *Acta Cryst.*, submitted for publication.

RESOLUTION CORRECTIONS FOR AN AREA DETECTOR IN SMALL ANGLE NEUTRON SCATTERING

Bernard Mozer

The spectrometer, D-17, at Institut Laue-Langevin, which contains an area detector, was used in a cooperative program on critical phenomena to study small angle scattering from He-4 at the gas-liquid phase transition. It is necessary to obtain corrections that reflect the angular smearing by the incoming neutron beam, the extent of sample volume, and the angular divergence of the elemental areas of the two-dimensional detector in order to achieve the proper structure factor from the measured data. To estimate these correction factors, we can consider the structure factor for ^{4}He in the critical regime to be given by an Ornstein-Zernike (O-Z) expression

$$S(\kappa) \propto (\kappa^2 + \xi^{-2})^{-1}$$

where $\kappa = 4\pi \sin\theta/2/\lambda$ and ξ is the correlation length of the fluctuations.

The O-Z function is a good approximation for critical scattering, and corrections to it are considered small in modern theory. The correction factor can be calculated from the ratio of the average spectrometer smeared scattering function to the scattering function for a perfect system

$$C = N \frac{\int f(\lambda) \int S(\kappa^2)\; dA_s dV dA_D d\lambda}{S^o(\kappa^2)}$$

where $S(\kappa^2)$ is the O-Z function determined from allowable paths of the incoming beam of neutrons of area A_s onto some illuminated parts of the scattering volume V which are scattered to some elemental area A_D of the detector. $f(\lambda)$ is the smearing in wave length of the incoming beam. The incoming beam is considered uniform in space across the area A_s. The detector is assumed to be uniformly efficient for all neutron paths and

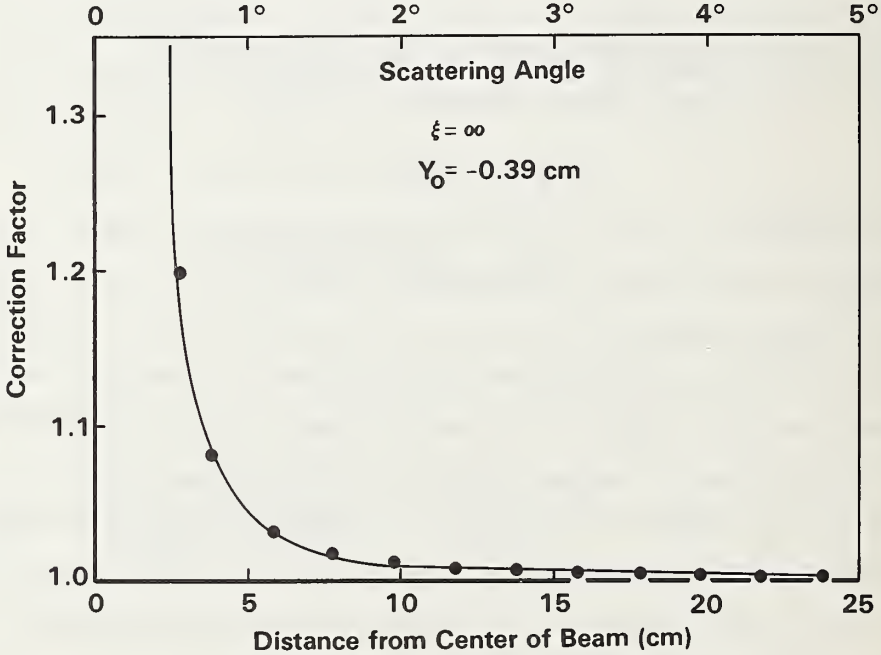

Figure 1. Correction factor for x-y detector along the x direction at a distance y_o = -0.39 cm. from the center of the beam. Calculated points are at the center of the elemental detector areas given by (x, y_o). The correction factor was calculated from an Ornstein-Zernike function for infinite correlation length, (See text).

corrections to its thickness are negligible. S^0 is the O-Z function for a neutron on the center line of the source and scattering volume and scattered to the center of the elemental area A_D of the detector. The integrals were evaluated numerically by an approximation of first order polynomials over the differentials as follows: various sized meshes were set up for the source area, scattering volume, and detector area and $S(\kappa)$ calculated for a path at the centers of the differential meshes. The mesh sizes were varied to estimate the error in the calculation until the results varied less than an allowable error (0.1%). The normalization consists of the total number of paths in the various meshes. The correction factor of the average scattering to the perfect scattering was evaluated for most of the elemental areas of the detector whose center for our experiment is located at a rotation of 6.4^o from the beam center. The accompanying graph shows the correction factor for a line of elemental areas whose centers are located 0.39 cm. below the center of the beam of the source (Y-axis) and vary the distances shown along the horizontal direction (X-axis) from the center of the source. In this calculation the correlation length was infinite and the O-Z function is $1/\kappa^2$. The graph also shows the scattering angle for S^o. The corrections are largest for this case and rapidly approach unity as the ratio of the correlation length to the average wave length approaches 10. One should note that the method can be used for other known scattering functions encountered in small angle scattering. A comparison of this calculation with Monte Carlo methods is being made in collaboration with C. Eisenhauer of CRR, NML, NBS.

NEUTRON SCATTERING FROM COHERENT ADMIXTURES OF PHONONS WITH LIBRONIC EXCITATIONS OF DIATOMIC IMPURITIES

R. C. Casella

The coherent mixed-mode states are represented in an S-matrix formalism. In the small-$\vec{q}$ quasicontinuum region, the phonon field is expanded in terms of vector cubic harmonics, analogues of vector spherical harmonics. Tunneling states of the diatoms in a cubic crystal field are analyzed via group-theoretically projected tight-binding local oscillator states developed by Dick. Plausible level schemes are constructed by joining the strong coupling spectrum they describe to the weak coupling (free-rotator) spectrum. See figure 1. This semi-phenonmenological approach does not depend upon details of the generalized Devonshire hindering potential. It is found that the T-matrix elements connecting the phonons with the libronic or hindered-rotator excitations vanish in lowest nontrivial order unless the latter are of E_g or T_{2g} symmetry. Expressions for estimating the relative strengths of these allowed T-matrix elements are derived. Results are applied to neutron scattering experiments on dilute-impurity $KCl:CN^-$ and $KBr:CN^-$, the latter having been carried out by J. J. Rush and J. M. Rowe at the NBS reactor. Further experimentation was motivated by the present theoretical analysis. Comparisons were also made with optical experiments on these systems. Of the usually considered < 100 > and < 111 > CN^- impurity models for these crystals, my analysis shows that the < 100 > model is eliminated by the neutron data, in agreement with earlier conclusions based upon optical and other experiments. See, also, my earlier analysis of the optical data.[1] Typical libronically excited tunnel-split symmetry states are illustrated in figures 2 and 3.

The absence of a T_{2g} interaction as observed in the neutron experiments presents a difficulty for the < 111 > model if the libronically excited observed E_g and unobserved T_{2g} levels are split by an amount of the order of the ground-state tunnel splitting, i.e., $O(1\ \mathrm{cm}^{-1})$. Under this assumption, the same difficulty exists for the < 110 > model which we are also led to consider. The relative strengths of the T_{2g} to E_g couplings of the phonon to the libronic excitations are estimated for both the < 111 > and < 110 > models. For both models, the computed ratios of T_{2g} to E_g couplings are of order unity under the assumption that the excited tunnel splittings are small. This clearly suffices to rule out the latter assumption if either model is correct. It is concluded that the T_{2g} rotational excitations of the CN^- ions lie considerably above the observed E_g libronic excitations and that the former are lifetime broadened to the extent that formation of coherent mixed modes

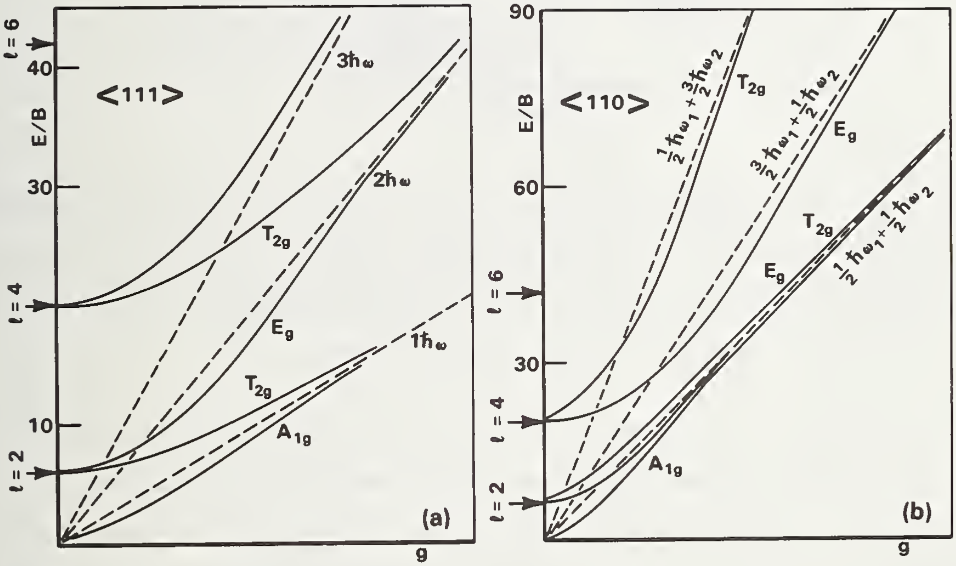

Figure 1. Schematic of ground A_{1g} and low lying E_g and T_{2g} energy levels for (a) the < 111 > model and (b) the < 110 > model vs. generalized coupling to the hindering potential. For each value of g, the zero of energy is chosen at the bottom of the local oscillator well; hence, somewhat unconventially, the curves rise with increasing g for large g. $B = \hbar^2/2\mu d^2$ is the diatomic rotational constant. ℓ is the angular momentum when g = 0. The dashed curves represent asymptotic values approached by the tight-binding local oscillator states in the strong coupling regime. Only qualitative features are illustrated. As pictured in (b), $\omega_2 = 3\ \omega_1$.

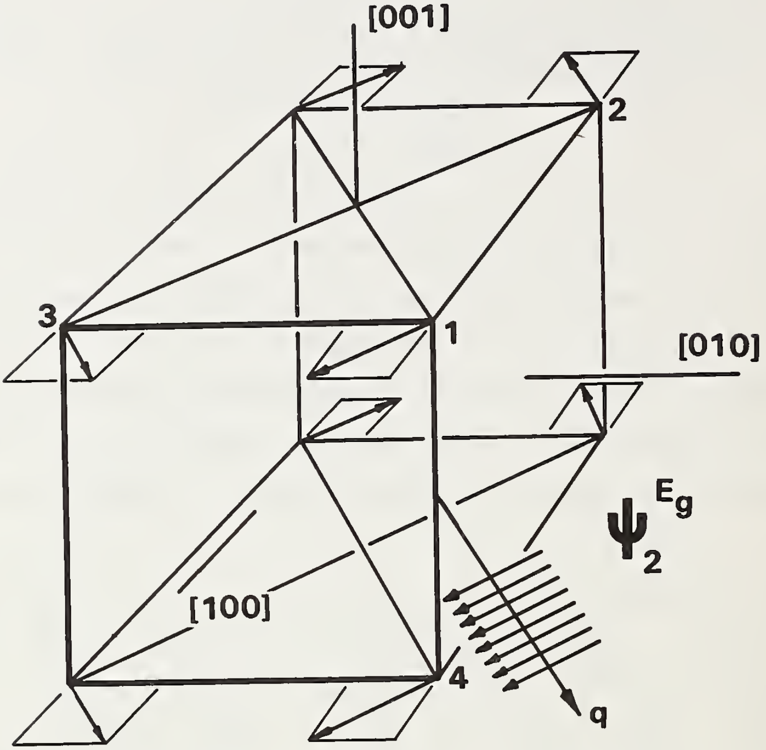

Figure 2. Correlated linear motions of the A ions for the first excitation of the libronic E_g tunneling state $\psi_2^{E_g}$ of the diatomic molecule AB for the < 111 > model. The long wavelength TA phonon with $\vec{q}$ || [110] and $\vec{\xi}$ || [1$\bar{1}$0] is also shown.

does not occur; hence the absence of neutron observed splitting of the phonon modes in the T_{2g} configuration. Our analysis of existing Raman data lends support to this conclusion. Under the assumption of large excited-state splitting, our estimation procedure for the T_{2g}/E_g coupling ratio does not apply and the neutron data are compatible with either the < 111 > or < 110 > models. In the event that future neutron experiments allow the observation of the splitting of the TA phonons via transitions induced between the libronic ground state tunnel-split levels, it may be possible to decide between these two models on the basis of neutron data alone. Earlier optical experiments favor the < 111 > model. This work has been submitted for publication.

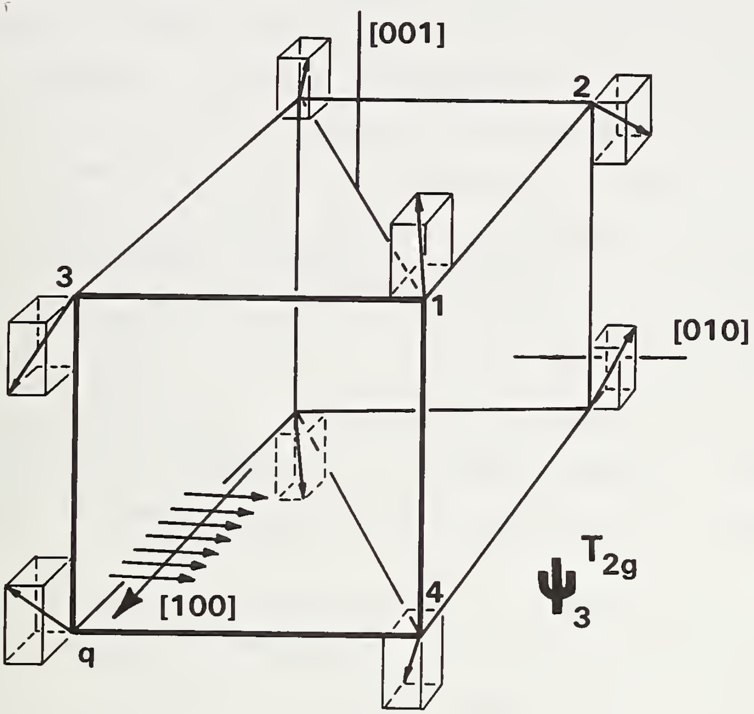

Figure 3. Correlated linear motions of the A ions for the first excitation of the libronic T_{2g} tunneling state $\psi_3^{T_{2g}}$ of the diatomic molecule AB for the < 111 > model. The long wavelength TA phonon with $\vec{q} \parallel [100]$ and $\vec{\xi} \parallel [010]$ is also shown.

---

1. R. C. Casella, *N.B.S. Tech. Note* No. 995, (ed. F. J. Shorten 1979).

BOSE-EINSTEIN CONDENSATION OF EXCITONS

R. C. Casella

Recently it has been reported in the literature that a Bose-Einstein (BE) condensation of excitons, a phenomenon I proposed some years ago,[1] has been discovered experimentally in CuCl.[2] In the past, other mechanisms such as the formation of electron-hole droplets have sometimes been confused with BE condensation so that it may require further experimentation and analysis before the effect is fully confirmed. For many semiconductors it happens that to achieve the critical concentration to attain condensation at, say, T = 2K, the electron-hole system becomes so dense that shielding prevents the formations of excitons (or exciton molecules[1]), yielding instead an electron-hole plasma.[3] Therefore, before considering the possibility of BE condensation one has to be satisfied that excitons or excitonic molecules even exist at the high light excitation levels employed. I have applied the criteria developed in reference 3 to establish that under the experimental conditions reported in reference 2 for CuCl, excitons can indeed exist to form molecules, which then presumably condense.

---

1. R. C. Casella, *J. Chem. Phys. Solids* 24, 19 (1963).
2. L. L. Chase, N. Peyghambarian, C. Grynberg, and A. Mysyrowicz, *Phys. Rev. Lett.* 42, 1231 (1979).
3. R. C. Casella, *J. Appl. Phys.* 34, 1703 (1963).

TIME-DEPENDENT HEAT FLOW

R. S. Carter and R. C. Casella

One of the problems being reviewed as part of the safety analysis for 20 MW reactor operation is that of the unrestricted excursion. A finite ramp insertion rate of reactivity is assumed, and all safety systems are assumed to fail. The power rises exponentially until sufficient boiling occurs in the coolant to shutdown the reactor. Part of this analysis requires estimating the time dependent temperature distributions within the fuel plate. The following idealized calculation is useful in estimating this distribution.

We have considered the response of a thin slab of material to a transient heat current input, $\Delta j(x = 0, t)$, calculating the change in temperature $\Delta T(x = 0, t)$ at the source, assuming the other side of the slab (at $x = L$) is in contact with an infinite heat sink; i.e., assuming $\Delta T(x = L, t) = 0$. For general $\Delta j(0,t)$

$$\Delta T(0,t) = \left(\frac{1}{\pi \kappa c}\right)^{\frac{1}{2}} \int_{0}^{t} dt' \, \frac{\Delta j(0,t')}{(t-t')^{\frac{1}{2}}} \, F_c\left(\frac{t-t'}{\tau_1}\right), \qquad (1)$$

where

$$F_c(x) \equiv \sum_{n=-\infty}^{\infty} (-1)^n \, e^{-n^2/x} \, . \, , \qquad (x>0) \qquad (2)$$

Here, κ is the thermal conductivity of the slab [Watts/cm^2 - K], c is its heat capacity [Joules/cm^3 - K], and τ_1 is a characteristic response time,

$$\tau_1 = L^2 c/\kappa. \qquad (3)$$

For an aluminum slab of thickness L = 0.076 cm (30 mils), $\tau_1 \sim 7 \times 10^{-3}$s. $F_c(x)$ is related to the so called θ-function. It assumes the value, unity, at $x = 0$ and decreases monotonically with increasing x, equaling 0.3 at $x = 1$, 0.01 at $x = 2.5$. It also obeys the sum rule,

$$\int_{0}^{\infty} dx \, x^{-\frac{1}{2}} \, F_c(x) = \pi^{1/2}. \qquad (4)$$

Numerical solutions to Eq.(1) have been obtained for the important special case, where

$$\Delta j(0,t) = j_o(e^{\beta t} - 1). \qquad (0<t<t_f) \qquad (5)$$

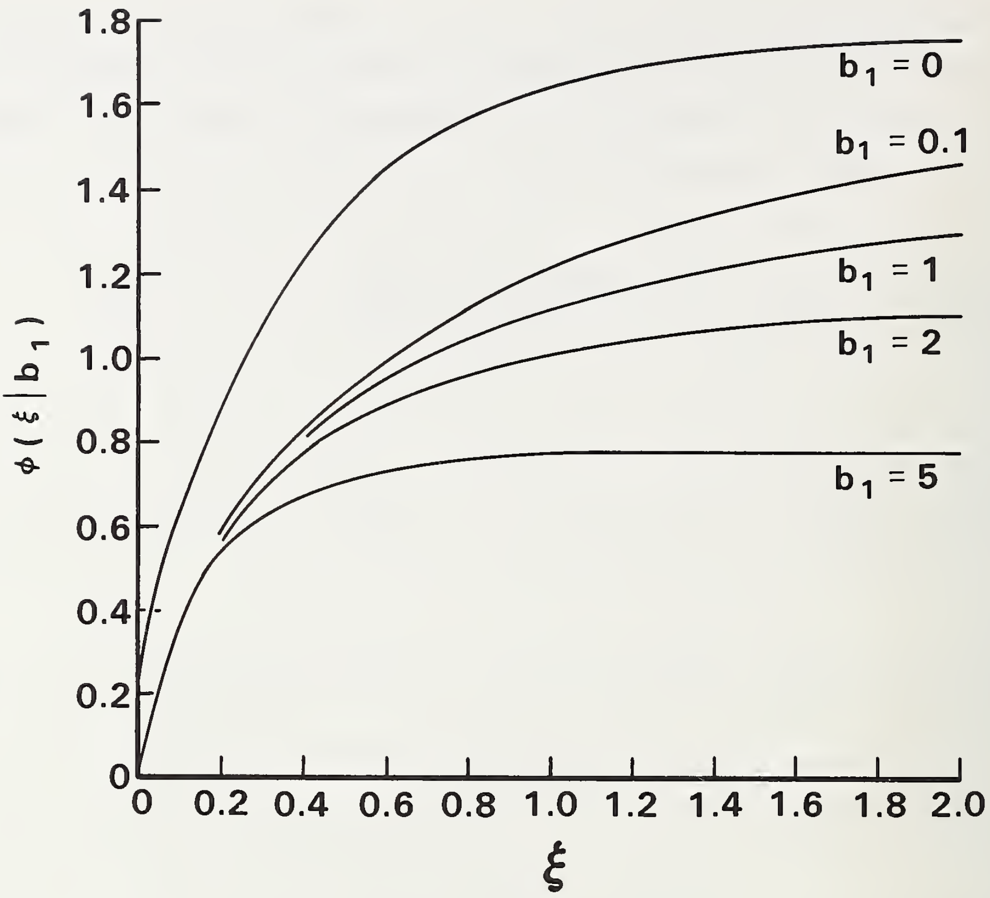

Figure 1. The function $\phi(\xi|b_1)$ for various values of the parameter $b_1 \equiv \beta\tau_1$. $\xi \equiv t/\tau_1$ where t is the time lapse since the onset of the transient and τ_1 is a characteristic response time of the material. β^{-1} is the risetime of the transient. Cf., Eqs.(3), (5) and (6) of text.

Here, j_o is the steady-state heat current density into the slab at x = 0 prior to the onset of the transient (at time t = 0) and β^{-1} is a characteristic rise time for the transient. Eq.(5) is assumed to hold until some time t_f at which time the transient begins to decay. For $t < t_f$, we find

$$\frac{\Delta T(0,t)}{\Delta j(0,t)} = (L/\kappa)(1/\pi)^{\frac{1}{2}} \ \phi(\xi|b_1). \tag{6}$$

Here $b_1 \equiv \beta\tau_1$, $\xi \equiv t/\tau_1$ and $\phi(\xi|b_1)$ is as shown in figure 1. As seen from figure 1, for $\tau_1 << \beta^{-1}$ and $t >> \tau_1$,

$$\Delta T(0,t) \rightarrow (L/\kappa)\, \Delta j(0,t). \qquad (7)$$

That is, for τ_1 sufficiently small, the system responds adiabatically on a time scale large compared with τ_1.

The problem solved is a highly idealized representation of the response of the aluminum cladding in a reactor rod to a transient increase in nuclear power. For example, it completely ignores the complicated boundary conditions at the interface of the cladding with the coolant, replacing them with the condition $\Delta T(L,t) = 0$. Moreover, the heat flow within the active region of the rod is reduced to the current input $\Delta j(0,t)$. Nevertheless, it provides some physical insight with which to view the solutions of complex computer codes which attempt to deal with the actual situation more realistically.

NEW SMALL-ANGLE SCATTERING FACILITY

C. J. Glinka, A. Cinquepalma, J. M. Rowe, and J. J. Rush

Much of the engineering design work has now been completed for a new, state-of-the-art, small-angle neutron scattering (SANS) facility. The fabrication and procurement of various components of the instrument are well underway and installation is expected to begin in September, 1979.

The layout of the new SANS instrument is shown schematically in figure 1. The required collimation of the beam will be achieved by using "pinhole" geometry along an evacuated flight path having a maximum total length of 8 meters from source aperture to detector. Before entering the flight path, the beam will pass through two liquid-nitrogen cooled

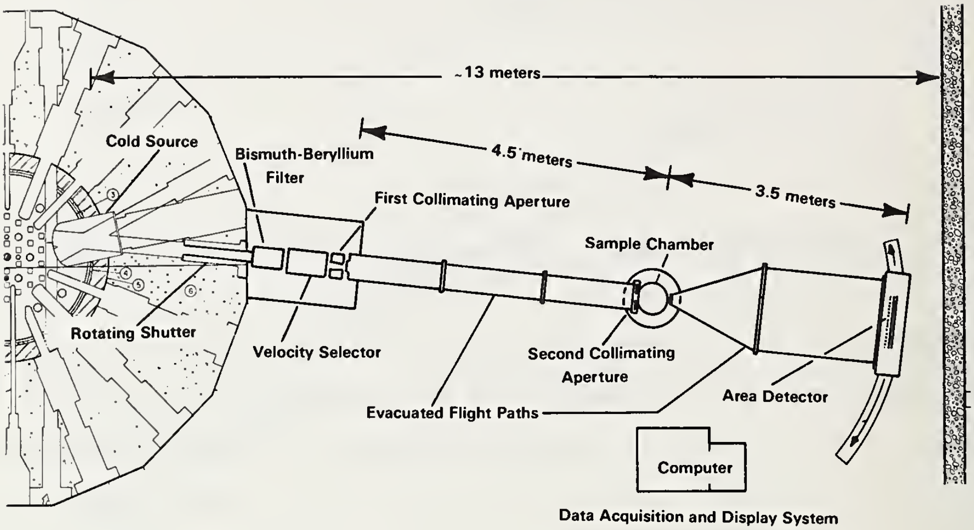

SMALL ANGLE SCATTERING SPECTROMETER

Figure 1. Layout of the new SANS facility.

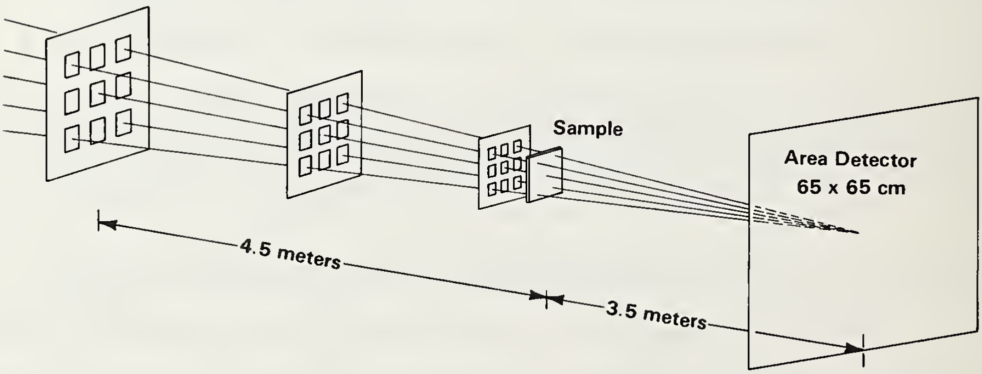

Focussing Collimation System

Figure 2. Principle of the focussed collimation system for the new SANS facility.

filters, ~25 cm of beryllium and 10 to 15 cm of single-crystal bismuth. The total transmission of the filters for wavelengths>4 Å should be ~75% with little contamination from fast neutrons or gamma rays. Following the filters, a helical channel velocity selector will be used to vary the mean incident wavelength between 4 and 12 Å with a wavelength spread $\Delta\lambda/\lambda(\mathrm{FWHM}) \simeq 0.20$.

The sample position will be fixed at a distance of 4.5 meters from the source aperture. The source and sample apertures define the divergence of the incident beam which will be variable from about 5 to 15 minutes of arc. The evacuated flight path after the sample will be segmented to give a choice of sample-to-detector distances of either 2.0 or 3.5 meters. The detector and flight path will mount on an arm which can rotate about the sample position to reach larger scattering angles.

A vacuum sample chamber is planned for the new instrument which will house a multiple sample changer. Sample sizes will range from about 0.25 cm x 0.25 cm to 2 cm x 2 cm. The sample table is being designed to be compatible with existing cryostats and furnaces as well as a horizontal field electromagnet and a vertical field superconducting magnet.

A unique feature of the instrument will be an optional high resolution collimation system for use with larger samples (~1.5 cm x 1.5 cm). The collimator will consist of 9 channels focussed to a point on the plane of the detector. As a result of this focussing, which is depicted in figure 2, neutrons scattered through an angle θ converge to the same point on the detector. Thus the intensity on the sample is increased ninefold with essentially no loss in resolution.

The detector will be a two-dimensional position-sensitive proportional counter of the Borkowski-Kopp type. Delivery is expected on a first detector[1], with an active area of 25 cm x 25 cm and a resolution of 3 to 4 mm in each direction, in the Fall of 1979. This detector will ultimately serve as a back-up for a larger detector with a sensitive area of 65 cm x 65 cm and a resolution element of ~5 mm on a side. Both detectors will have an efficiency of 80% for 5 Å neutrons.

The instrument will be controlled by a dedicated PDP 11/03 computer which will in turn be linked to an existing network consisting of a VAX 11/780 and a PDP 11/40. A color monitor for visual display of the data from the detector will be available at the VAX node.

Under a typical configuration with reasonably high resolution, the new SANS instrument will cover a Q range from 0.003 A^{-1} to 0.10 A^{-1} (with the beam centered on the detector) with a resolution ΔQ(FWHM) at Q_{min} of 0.002 A^{-1}, assuming a wavelength of 6 Å and $\Delta\lambda/\lambda = 0.20$. At this resolution and wavelength, the flux on the sample is expected to be 6×10^4 n/cm^2-sec with the reactor operating at 20MW. Furthermore, this flux will be provided over a sample area of 1.2 cm x 1.2 cm by virtue of the focussed collimation system. Other configurations of higher or lower resolution will allow fluxes on the sample between 10^4 to 10^6 n/cm^2-sec. It is anticipated that the new SANS facility will begin operating in the latter part of 1980.

---

1. Technology for Energy Corp., Knoxville, TN.

THE VISUALIZATION OF RADIOGRAPHS HAVING A RADIOGRAPHIC DENSITY GREATER THAN 7.0

M. Ganoczy

In an effort to obtain maximum contrast from a radiograph film, it is necessary to expose such that the film density is extremely dark. Oftentimes the film is overexposed to a point on the D-Log E curve that the film is unreadable with high intensity viewers. At times, the radiographic exposure cannot be reproduced for reasons, e.g. that the specimen under inspection may become highly radioactive from a second irradiation. As a spinoff of our activities with the neutron-induced autoradiography of paintings project, we were able to retrieve data from radiographs having a density greater than 7.0 by autoradiography of activated silver in overexposed radiographs.

NUCLEAR APPLICATIONS TO ANTIQUITIES

Y. T. Cheng, M. Ganoczy, and D. A. Garrett

The Smithsonian Institution is funding a feasibility study to employ nuclear technology for authenticating reportedly valuable paintings and for dating and possibly attributing to specific artist works of unknown origin. The methods under investigation are neutron-induced autoradiography and high-resolution gamma-ray spectroscopy. The irradiation required for both these techniques renders a painting radioactive for a brief period. The research group will attempt to determine whether the radiation permanently alters the work in any way.

Both methods of analysis are conducted simultaneously: A painting is placed in a thermal neutron field from a nuclear reactor, rendering the elements contained in the painting pigments temporarily radioactive.

Autoradiography is achieved by placing radiographic films in direct contact with the painting at periodic intervals after the irradiation, causing film exposure by beta rays as the radioactive pigments decay to their ground states. By interpreting these autoradiographs, it may be possible to identify within them characteristics which relate to a particular artist, such as methods of applying pigments, brush strokes, and style of painting.

Gamma-ray spectroscopy is being used to quantitatively identify the elemental content of the painting. Such information is useful as dating evidence because elemental content in pigments has continually changed throughout the ages. By incorporating the two techniques, one would be able to relate a particular type of pigment to the specific area in the painting, and because different elements have different half lives, one would also be able to extract the depth informations of the paintings.

The primary concerns in the study of valuable painting is that of the safe handling of those paintings, both in the activation phase and later on in the autoradiography. For the first part, the amount of radiation received by the painting was held to a minimum; a combined neutron and gamma dosage of less than 1000 rads.[1] This is 100-1000 times smaller than the permissible dose.[2,3] The painting received the 1000 rads dose by being exposed to a thermal neutron fluence of ∿ 3 x $10^{12}/cm^2$. The history of this technique is only ten years and is sufficient upon which to base radiation damage contamination if any.

In the feasibility study a 19th century English painting of the size 14" x 17" was activated by such a neutron fluence. It was then placed in a specially designed light-proof film cassette and autoradiograph. The subsequent autoradiographs and the gamma-ray spectroscopy were taken at the NBS site. A private art conservator supervised the safe handling of the painting. The result of the analysis showed the painting possesses a broad background painted with mercury based pigment. The present method was able to identify elements with half lives longer than that of Mn, 2 1/2 hrs. The elements of Na, Cr, Sc, Fe, Co, Zn, Ag, Cs, Ba, Sb, Hg, and Au were identified. The very short lifetime elements could prove to be very interesting. An effort is now being made to obtain such information.

MEASUREMENTS FOR NUCLEAR SAFEGUARDS VERTICAL FACILITY

D. A. Garrett and M. Ganoczy

Considerable manpower effort has been expended during the past year in the design of the vertical facility which would serve the Resonance Neutron Tomography System for the Measurements for Nuclear Safeguards Program, and at the same time, serve the NBS Resonance Neutron Radiography Project for limited resonance neutron radiography applications. The two most important factors to be considered were those of providing access to other experimental parts without removing the system during reactor operation and radiation leakage to the Operations Personnel. The system has been designed so that the first factor has been resolved, and additional modularized radiation shielding can be added if necessary for background reduction.

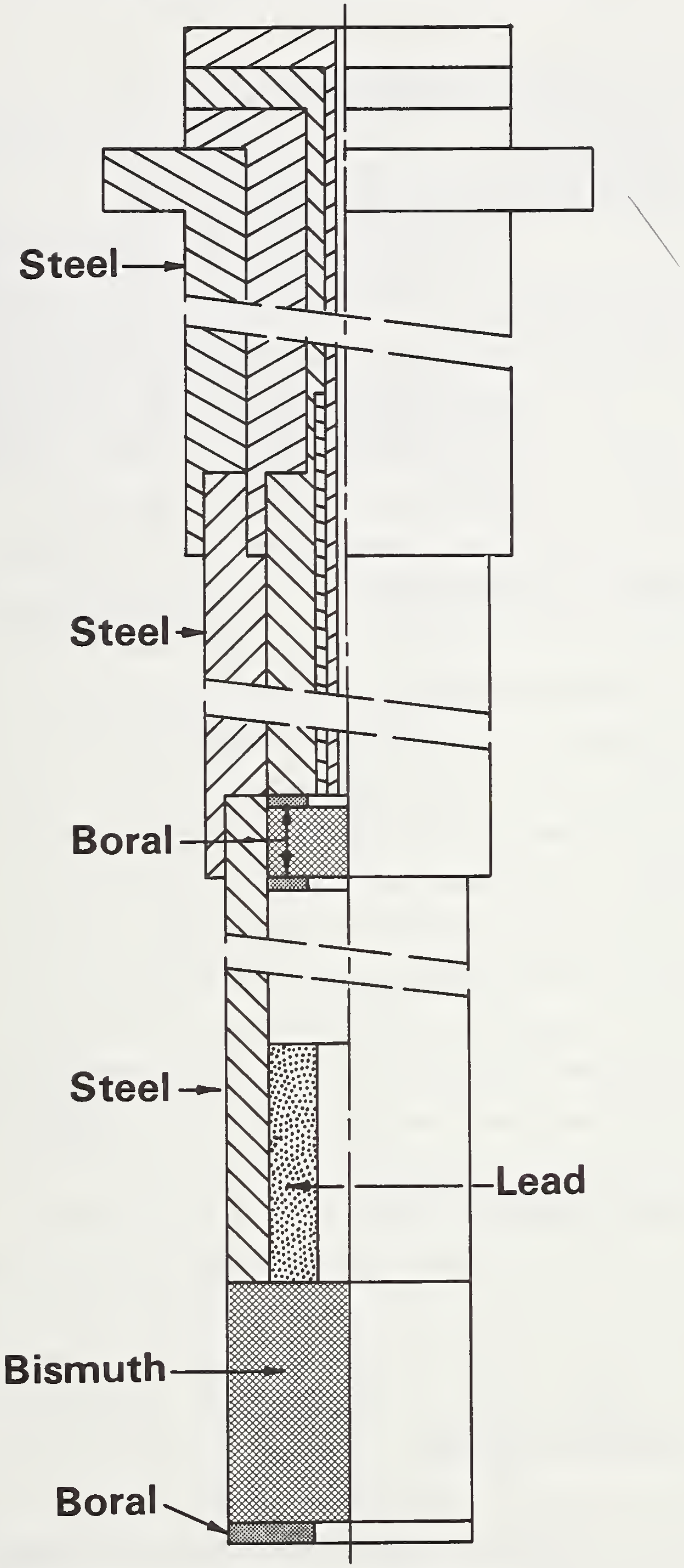

Figure 1. Nuclear Safeguards vertical facility.

NEUTRON RADIOGRAPHIC STANDARDS: MEASUREMENT OF THE L/D RATIO

W. L. Parker
(Reed College, Portland, OR)

and

D. A. Garrett

The purpose of this work is to evaluate a standard method to measure the L/D ratio of a neutron radiographic facility, where L is the distance between the neutron source and the image plane and D is the diameter of the neutron source, assuming that the source possesses a finite diameter. In general, an ideal nuclear reactor-based system consists of the components illustrated in figure 1, i.e., a distributed thermal neutron source consisting of a collimator and a fast source and moderator, a gamma filter, a thermal column, a defining aperture, a neutron collimator, biological shielding, and an imaging system.

Next to the flux, probably the most important parameter to be specified for a neutron radiographic facility is the L/D ratio, since it, to a large extent, determines the quality of the neutron radiographs that can be made. It is the predominant determinant of maximum resolution for any but the thinnest specimens placed very close to the neutron converter. Other factors such as type of converter, type of imaging device, amount of scattered neutrons, fast neutrons and gamma rays in the beam, spatial uniformity of the beam, and beam divergence can, in general, only degrade the quality of the image with the limiting quality being determined by the L/D ratio which determines the solid angle subtended at the image plane by the aperture of diameter D as illustrated in figure 2.

For an ideal, reactor-based neutron radiographic facility in which one defines an aperture such as a circular aperture in a boral plate or gadolinum foil placed against a well-defined, uniform, and isotropic source such as the surface of a graphite thermal column, the determination of L/D should involve only the independent measurement of L and D, two well-defined distances. However, beam nonuniformity and scattered neutrons may combine to give an effective L/D different from the simple geometrical

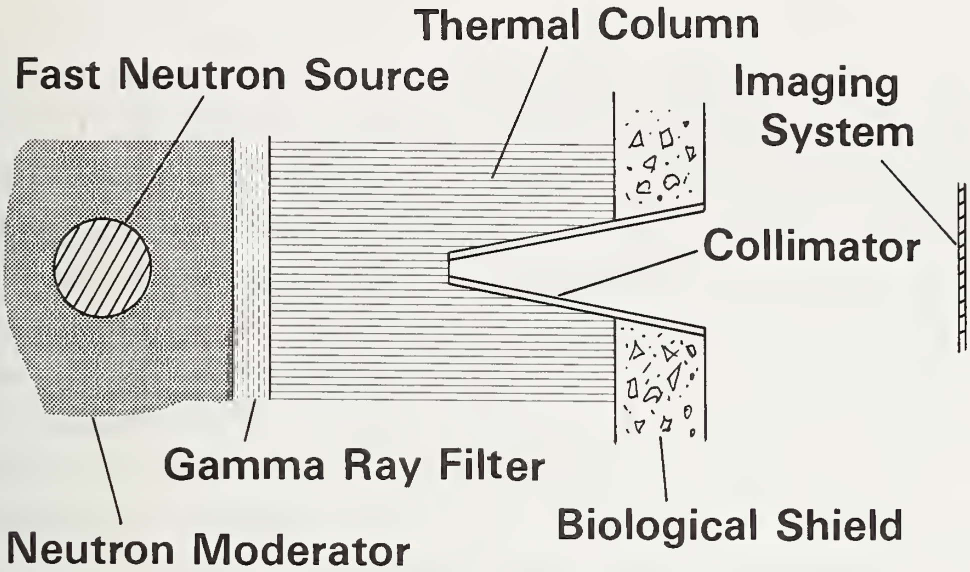

Figure 1. Typical neutron radiography facility.

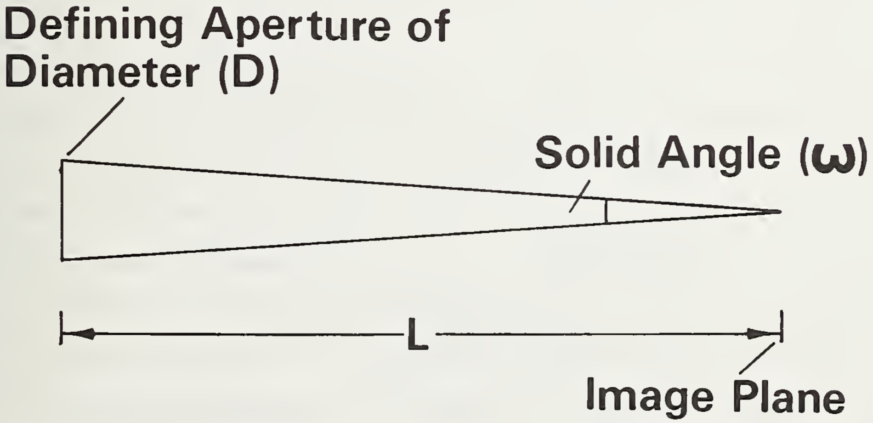

Figure 2. Solid angle ω subtended at image plane by aperture of diameter D.

ratio.

For a transportable portable thermal neutron radiographic facility involving a moderator surrounding an isotopic source or the target of a neutron generator, with the collimator looking at a flux trap, the determination of L/D is not trivial. Not only is the source poorly defined, but also the flux very probably peaks in the center of the trap resulting in a large amount of nonuniformity in the beam. For instance, consider the thermal neutron flux in a thermal column or moderator as a function of distance from the source for various moderators illustrated in figure 3.

The development of an experimental method for the determination of the ratio is important because future neutron radiographic standards will almost certainly contain some specifications for the ratio.

The method employed is a combination of methods developed by groups at Aerotest Operations and the IRT Corporation. It involves measurements of the width of radiographic shadows of neutron absorbing objects of the same width placed at different distances from the cassette holding the converter and the film as illustrated in figure 4.

Consider figure 5 which indicates the shadows cast by three objects of identical width, d_o, placed at different distances, h, from the image plane which is at a distance, L, from the source of diameter, D. For object C, the central position of the shadow, the umbra, "sees" the entire source while the outer portions, the penumbra, sees only a portion of the source. As the object is moved from the image plane toward the source, the width of the shadow increases, while that of the umbra decreases. Object B is at the critical position at which the width of the umbra approaches zero. For an object closer to the source, such as A, none of the shadow is in total "darkness," and the central portion is the region of equal "illumination." The width of the whole shadow (d) and that of the central portion (c) continue to increase as the object is moved away from the image plane.

The Aerotest method is based on determining b, the value of h at which the width of the umbra approaches zero. It is easy to see from

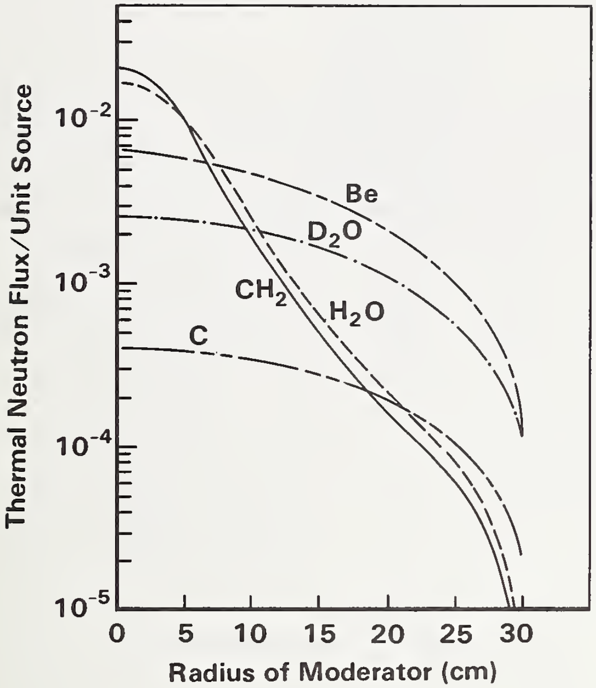

Figure 3. Thermal neutron flux as a function of distance from source in several moderator materials.

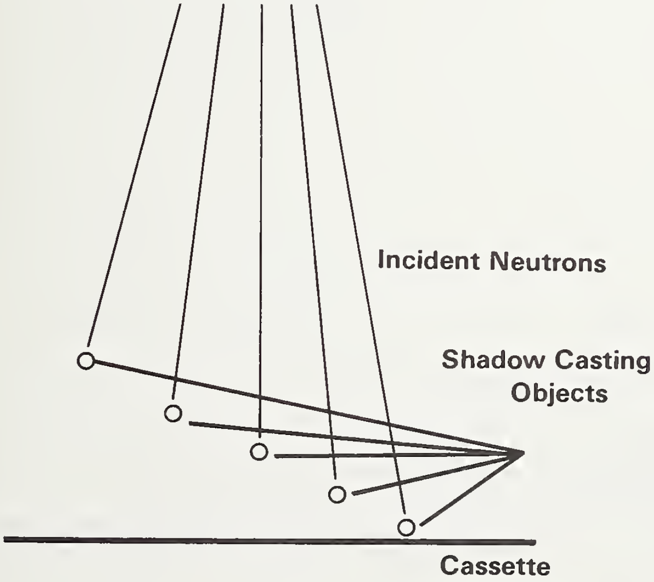

Figure 4. Shadow-producing objects at varing distances from the image plane.

similar triangles that

$$\frac{b}{d_o} = \frac{L}{D} \qquad (1)$$

To determine b, a radiograph is made of a series of cadmium wires, 0.023" diameter, spaced at 2.00 mm intervals for values of h from 0 to 40 mm and at 5.00 mm intervals from 40 to 100 mm. The resulting images of the shadows are then scanned with a recording microdensitometer operated with a 20 x 300 micrometer aperture and a linear magnification of 50 X.

Since the radiograph is a negative, the shadow of an obstacle such as the Cd wire appears on the radiograph as a transmitting slit which becomes broader and more diffuse as the obstacle is moved further from the cassette. It is convenient to use the background (high neutron flux, high radiographic density) as the baseline for the microdensitometer tracings so that the center of the shadow (low neutron flux, low radiographic density) is the top. Ideally we should then have for $h < b$ symmetrical trapezoids of constant height and constant area with the sides being nearly parallel for objects near the cassette. As the object to cassette distance increases, the width of the base (W_d) increases and the width of the top (W_c) decreases until the trapezoid becomes an isosceles triangle when $h = b$. As the object is moved further from the cassette ($h > b$) both W_d and W_c increase; however, the amplitude decreases. Ideally the area of the trapezoid should remain constant.

A typical microdensitometer tracing of the set of shadows of the cadmium rods from a radiograph is illustrated in figure 6. The nominal value of L/D is 40. The linear magnification is 2X and the reproduction has been reduced to about 0.4 of original size. The broad shadows at the ends are of 0.020 inch cadmium plates. At the scanning speed (1.17 in/min) (2.97 cm/min) used, the sharper shadows are reduced in height and artificially sharpened by the mechanical inertia of the pen-density wedge system.

Figure 7 illustrates individual tracings of the four peaks indicated by arrows in figure 6. Rod 1 is closest to the cassette; rod 5 is closest to the position for which $h = b$. Rods 9 and 18 illustrate typical

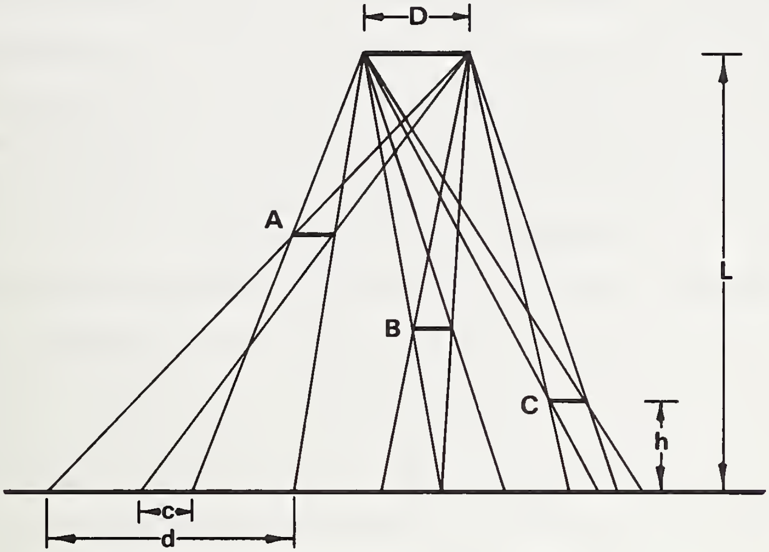

Figure 5. Shadows cast by identical objects.

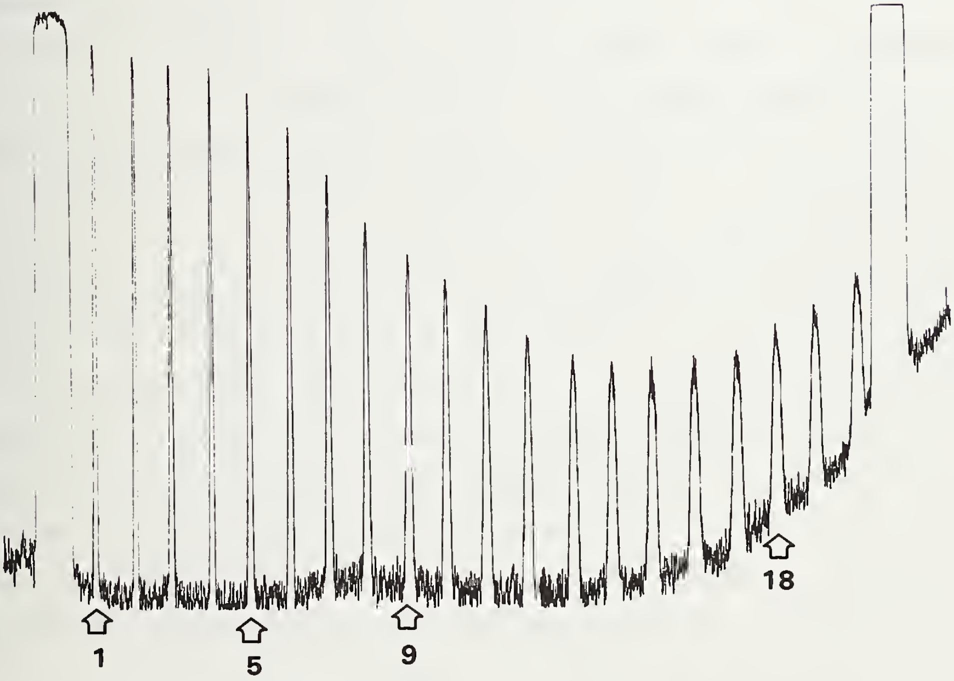

Figure 6. Typical microdensitometer scan.

tracings for $h > b$. Linear magnification on the tracing is 50X, and the reproduction has been reduced to about 0.4 of 2/3 the original size. The scanning speed was 0.155 in/min (0.39 cm/min). Measuring lines have been drawn in. It is apparent that the positions of the top and side lines become less accurately known as h increases, with a resulting increase in the uncertainty of the measurements of W_d and W_c.

It is apparent from figure 7 that the tracings approximate the predicted trapezoidal shape for small values of h, but with rounded corners for large values of h. The rounding of the upper (low radiographic density) corners becomes more pronounced as h increases. The finite width of the aperture certainly contributes to the rounding, but this contribution is much too small to account for the observed curvature at large values of h. We have not investigated the problem analytically, but feel that the rounding of the corners is due primarily to the mechanical inertia of the pen-wedge system and to the non-linearity of the photographic emulsion when used to measure intensity (exposure).

As used by the Aerotest group, the values of W_c as a function of h are extrapolated, using a least-squares fit to a linear function of the data, to find b, and equation (1) is used to find L/D.

The NBS system of analysis uses more of the available data than does the Aerotest method. It also uses measurements of the width of the base of the trapezoid and of the top for $h > b$.

Simple analytic geometry indicates that the measured quantities width of the base, W_d, of the top, W_c, and of the mean width, $\overline{W} = (W_d + W_c)$ when plotted as a function of h, [more accurately as a function of $h(1 - h/L^*)^{-1}$, where L* is an approximate value of L] should give straight lines with the slopes for W_d and for both W_c and $\overline{W}$ for $h > b$ equal to the reciprocal of L/D after correction for magnification factor. The slope of W_c vs. h for $h < b$ should be negative of this slope, and the plot of $\overline{W}$ for $h < b$ should be a horizontal line whose ordinate is the magnification times d_o.

It was possible to obtain the test object from the Aerotest group.

It was mounted on the cassette and a series of eight radiographs made at distances of 70, 90, 103, and 130 in. (177.8, 228.6, 261.6, and 330.2 cm) from the face of the reactor with apertures of 1.00 and 2.50 in.(2.54 cm & 6.35 cm) in diameter. The apertures were placed against the face of the thermal column of the NBS reactor and were 32 in. (81.92 cm) behind the reactor face. The technique of taking radiographs at a series of distances from the reactor was borrowed from the IRT procedure.

An NBS test object has been constructed consisting of two sets of obstacles placed at 0.25 in. (0.64 cm) intervals from 0.25 in. (0.64 cm) to 5.00 in.(12.7 cm) from the cassette. One set consists of 0.023 in. (0.058 cm) diameter cadmium wires; the other gadolinium strips 0.001 in. (0.0025 cm) thick and 0.032 in. (0.081 cm) wide. Both the wires and the strips are free-standing.

The reason for using the Gd strips in addition to the Cd wires is to determine if the circular cross-section of the wires introduces any error as compared to results obtained by using very thin obstacles, i.e., the 0.001 inch Gd strips.

A series of twelve radiographs were made of the NBS test object for distances (L') from the reactor face of 40, 60, 80, 100, 120, and 140 inches and apertures of diameters (A) of 1.00 and 2.50 inches. Exposures were adjusted so as to produce approximately the same density (about 1.6) at the centers of the radiographs. Figure 8 shows plots of W_d, W_c, and $\overline{W} = (W_d + W_c)/2$ vs. h for both the Cd wires and Gd strips as measured on the tracings of four of the radiographs. They are for the smallest and largest distances for both apertures. This encompasses the entire range of L/D for which radiographs were made. The lines were drawn in by eye. The lettered intersections on the plots for radiograph #6 will be referred to later.

The final analysis involves using linear regression to fit the various lines to the equation:

$$W = a_o + a_1 h (1-h/L^*)^{-1} \qquad (2)$$

L* is the approximate value of L which is used for this calculation and is equal to $L_o + L'$. For the NBS reactor L_o is taken to be 32 inches. If desired, the calculations could be repeated once a more accurate value of L_o has been obtained.

Most of the conclusions to be drawn are apparent from visual inspection of figure 6 and are verified by the mathematical analysis of the data. First we note that the apparent parrallelism of the Cd lines and the Gd lines in figure 8 indicates that any effect of the circular cross-section will be at most a second-order one.

As we have seen above, if no artifacts are introduced by our measuring process, the slopes of the various lines (except $\overline{W}$ for $h < b$) should be numerically equal; the reciprocal of the common slope should be L/D. Unfortunately this is far from being the case.

We shall use the following symbols for the slopes of the several lines:

$$a_{1d} = \text{slope for } W_d$$
$$-a_{1c-} = \text{slope for } W_c \ (h < b)$$
$$a_{1c+} = \text{slope for } W_c \ (h > b)$$

What we find is that a_{1c+} is considerably smaller than a_{1c-}, (by 60%) which in turn is generally, but not always, smaller than a_{1d}. For the smaller values of L/D the difference $a_{1d} - a_{1c-}$ can be as much as 25% of $a_{1av} = (a_{1d} + a_{1c-})/2$.

What then is to be taken as the value of L/D? The evidence so far indicates that our most consistent results result if we use the average of a_{1d} and a_{1c-}, i. e. a_{1av} as defined above. Some of the difficulties densitometer and non-linearity of the photographic emulsion. In effect, it is assumed that the artifacts change a_{1d} and a_{1c-} in opposite directions with the effects being about the same. This would seem to be a not-unreasonable assumption.

This means that all values of W_c for $h > b$ are being ignored. It is certainly arguable that values of W_d out of the same range should not be used. This is to be investigated in the future.

What is meant by "consistent results?" Essentially that good straight lines for an aperture are obtained when L/D is plotted vs. L', the distance from the face of the reactor. Figure 9 shows the results from eight radiographs taken of the Aerotest test object. The lines are a least-squares fit to the four sets of data.

If the values of L/D are plotted vs. L, a straight line given by the equation,

$$L/D - L_o/D + L'/D,$$ should result.

The point for L' = 103", D = 1.0" was not used in the calculation. The background density is considerably higher than for the other radiographs.

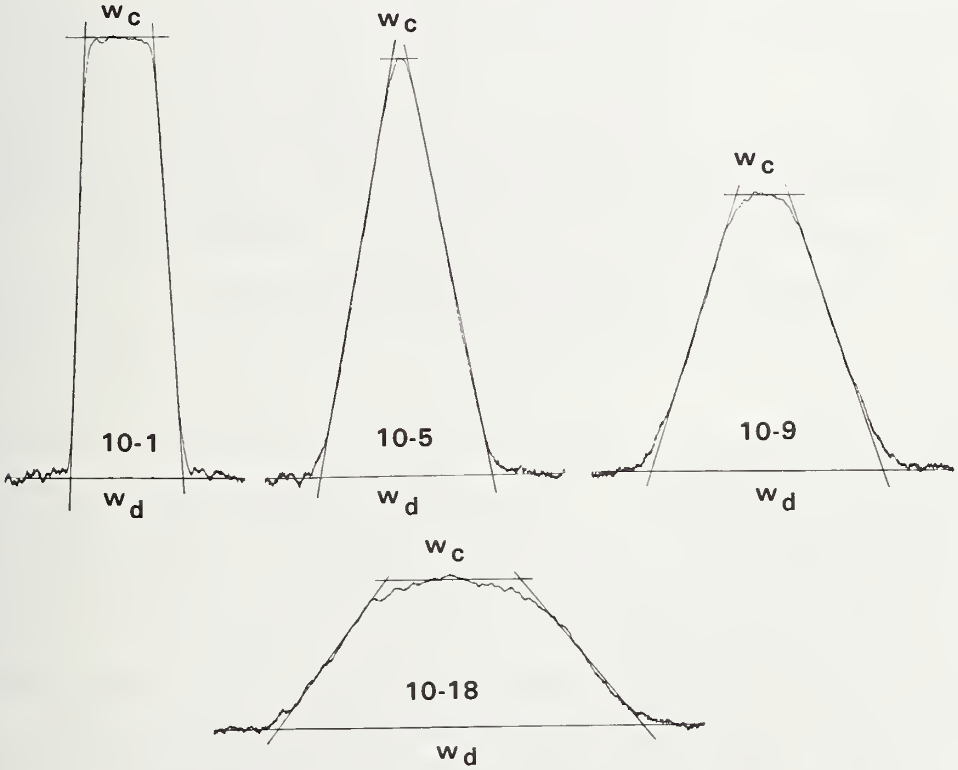

Figure 7. Individual tracings of four peaks.

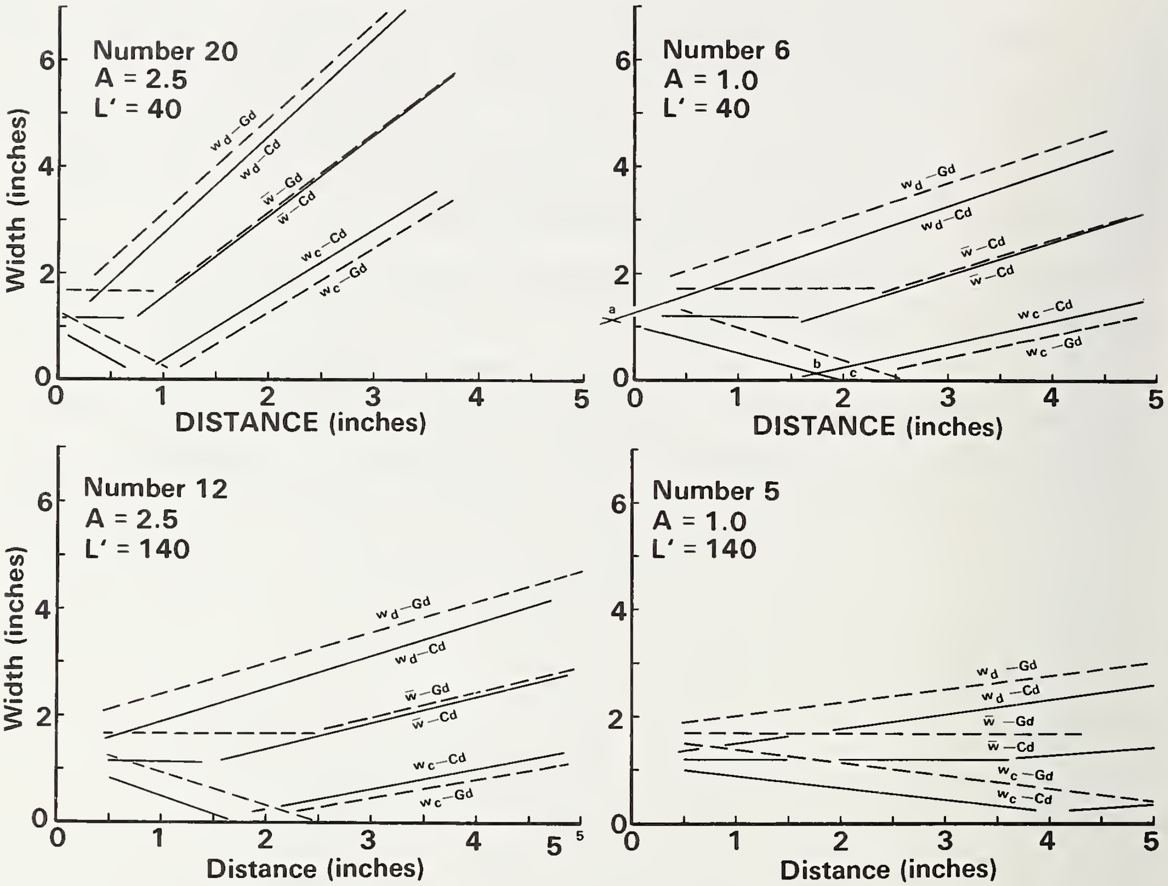

Figure 8. W_d, W_c, $\overline{W}$ vs. h for four typical radiographs.

From the slope and intercept of the plot of L/D vs. L', the values of D and L_o can be determined. The surprising result is that the values of D are about 80% of the actual size of the aperture. The cause of this phenomenon is attributed to the fact that the aperture is circular and the obstacles are linear.

If we take the abscissa of the point labeled c in figure 8 #6, as b and divide by d_o, the result is the value of L/D by the original Aerotest method. Where this has been done the values agree to better than 10% with that of the NBS method, but there does not seem to be as much internal consistency as the NBS method gives.

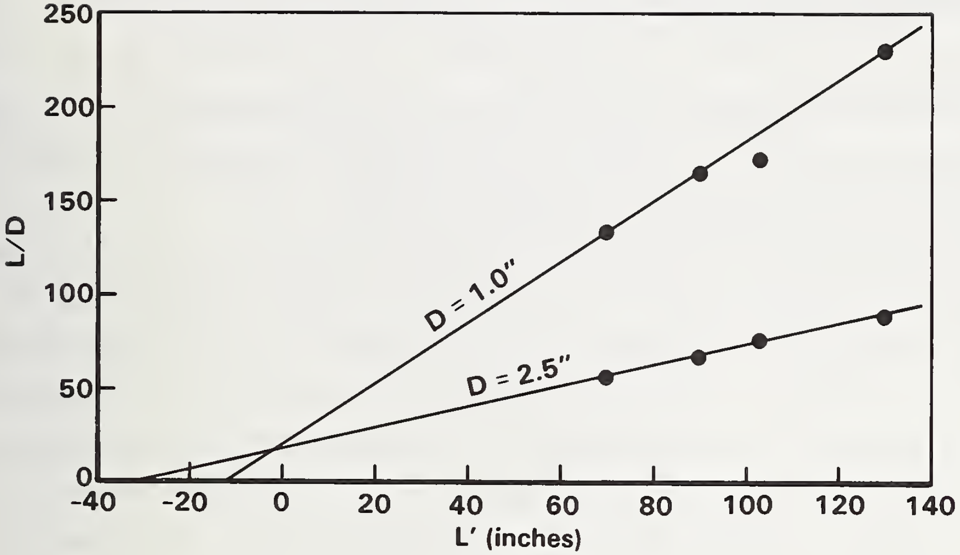

Figure 9. Plot of expeimtal values of L/D vs. L' for Aerotest device.

One of the most interesting results to come out of the study is evidence that the value of L/D obtained by the NBS method is definitely affected by the photographic procedure, primarily the background density of the radiograph. It is planned to investigate this phenomenon thoroughly in the next phase of this study. It may well be that it will be recommended that a value of L/D be quoted for a particular value of the background density.

The ideal way to measure d and c, and thus eliminate the microdensitometer and photographic emulsion, would be to scan the shadows of the absorbers with a neutron counter (a BF_3 tube for example) which has a slit aperture with a width very small compared to d_o (eg. approximately 10 micrometers). Using a recording system with very little inertia, one should be able to get measurements of d and c which are quite accurate. To the best of our knowledge, this has not yet been done. However, as long as neutron radiographs make use of the photographic emulsion, a photographic determination of effective L/D would continue to be useful.

MEASUREMENTS FOR NUCLEAR SAFEGUARDS-NRC SOFTWARE DEVELOPMENT

Y. T. Cheng

A project to develop the methodology for high-accuracy measurements and establish reference standards using resonance neutrons is funded through the Office of Nuclear Safeguards by NRC.

A nuclear waste container consisting of a gallon paint can is to be examined by a pencil neutron beam extended from the reactor core. The NBS double fission ionization chamber will be used to detect the transmitted neutrons. Through the self-indication effect , the isotope content in the waste will be identified. The results will be reconstructed tomographically and presented both in 3-dimensional plotted form and on a color graphic terminal with a different color for each different fissile isotopes, etc.

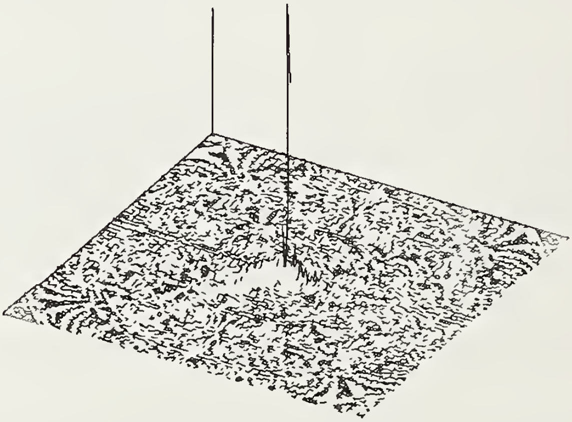

Figure 1. Isometric presentation of a delta function.

Firstly, a count-rate and sensitivity study has been made for the project which helped to decide what best available beam port position in the reactor to use, what ranges of fissile sample thicknesses and sizes that might be examined to an acceptable accuracy and the amount of time needed to gather such data. The results indicate Pu-239 (94% enriched) with thickness up to 60 mils has the greatest self-indication effects.

The usage of various filters is also proved to be necessary to differentiate between various Uranium isotopes. To completely scan the waste container (16.5 cm dia. x 10 cm high) using a 1 cm diameter neutron beam will take about 4 1/2 days to get a 1% counting statistic.

The kind of nuclear wastes we are proposing to study can generally be separated into two types. The first type is the lightly contaminated materials in which the density contrast is low; the other type consists of scraps and chips of fissile materials. The reason for such categorization is that the most suitable mathematical reconstruction techniques can then be employed to satisfy the diverse requirements, e.g. speed of computation, accuracy, etc. The filtered back projection algorithm will be used on the first type of nuclear wastes. The method has been well proven in the x-ray tomography field. This method has the advantage of short computing time and is relatively accurate, provides a optimum filter, is used in the frequency domain. The shortcomings of such algorithm are in the edge detectability, the ability to handle data from limited angles of projections, and the flexability to adopt different constraint conditions. To remedy this, the Iterated Algebraic Reconstruction Technique (IART) is used for the second type of wastes and for the first type when the above mentioned shortcomings come into question. The IART method has been successfully applied to fuel bundle assembly scanning.

The filtered back projection algorithm has been installed on the VAX-11/780 computer, it has been tested with a very high contrast environment - a delta function. This served two purposes, i. e., to determine the point spread function resulting from such a transformation, and to test out the effects of using different frequency filters in this "filtered" algorithm. If one Fourier - transformed a delta function, and then back projected it without filtering it in the frequency domain, one would get a very degraded picture. Instead of a sharp point, it would be like a large hub with many spokes projecting outward. However, even a very simple filter would improve the picture greatly. A ramp filter (high-pass) has been used and the result plotted three-dimensionally on the VERSATEC graphic plotter interfaced to the VAX computer. The result is shown in figure 1. The matrix format is 128 x 128, considering the diameter of the gallon paint can waste container, we have a pixel size about 1.25 mm. The picture shows a sharp peak and a fairly smooth environment which the algorithm handled quite well. The height of the peak is ∿ 76% of the delta function strength, the immediate surrounding noise is in the 25% level. One can also see several ringing artifacts which is caused by the filtering process. Further studies will be on using a filter with a gradual high frequency cutoff to reduce the artifacts while not degrading the contrast.

The Iterative Algebraic Reconstruction Algorithm is being installed on the computer. The two algorithms will be systematically examined and combined with previous count-rate and sensitivity study to stimulate the on-line data taking results.

NEUTRON RADIOGRAPHY OF CARDIAC PACEMAKER BATTERIES

D. A. Garrett and M. Ganoczy

In a project funded by the Food and Drug Administration, scientists in the Neutron Radiography Group are investigating one of the phenomena which occurs in cardiac pacemaker battery electrolyte during rundown. Current batteries must be surgically removed and replaced every 3 to 5 years. The goal of the manufacturer participating in this study is to develop a battery that would power a pacemaker for 15 years.

These new batteries consist of two central anodes of lithium metal with a cathode on either side as shown in figure 1. The space between the anode and electrodes is filled with polyvinyl puridine doped with iodine in a 1/10 mixture. As lithium iodide is formed, an electro-potential is produced between the anodes and electrodes which is employed to power the cardiac pacemaker.

With the use of x-radiography techniques, it was possible to penetrate the stainless steel case and electrodes to visualize on the "high atomic" number components in the electrolyte such as iodine. Thermal neutrons, on the other hand, can more easily penetrate heavy materials such as steel and yet are easily absorbed or scattered by light materials in the electrolyte such as the hydrogen contained in polyvinyl puridine.

Initial neutron radiography conducted on a new battery revealed the electrolyte distribution illustrated in figure 2. Further neutron radiography on a battery, which had been run down on an accelerated basis to 105 percent of its projected lifetime, exhibited what appeared to be areas of high neutron transmission shown as dark areas in figure 3.

In an attempt to better understand the observed phenomenon, three-dimensional neutron laminography was performed on the battery. This technique was first used with neutrons rather than x rays at the Argonne National Laboratory and was later further developed at NBS. Its primary use is to visualize the details of complex objects in three dimensions. In this case, the technique allowed examination of the electrolyte in layers spaced at 0.050 in. (1.27 mm) increments.

Neutron laminography radiographs revealed that areas of high neutron transmission occurred at various depths in the electrolytes as shown in figures 4 through 7 which could be void formation due to shrinkage of the electrolyte.

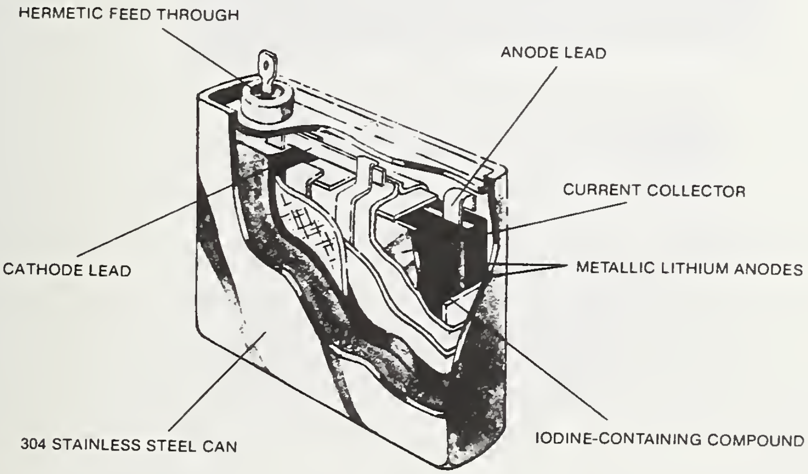

Figure 1. Schematic diagram of lithium-iodide pacemaker battery.

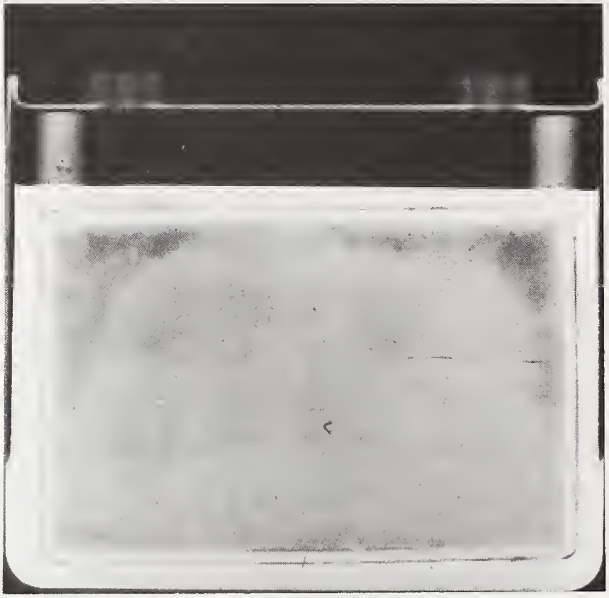

Figure 2. Neutron radiograph of undepleted lithium-iodide battery.

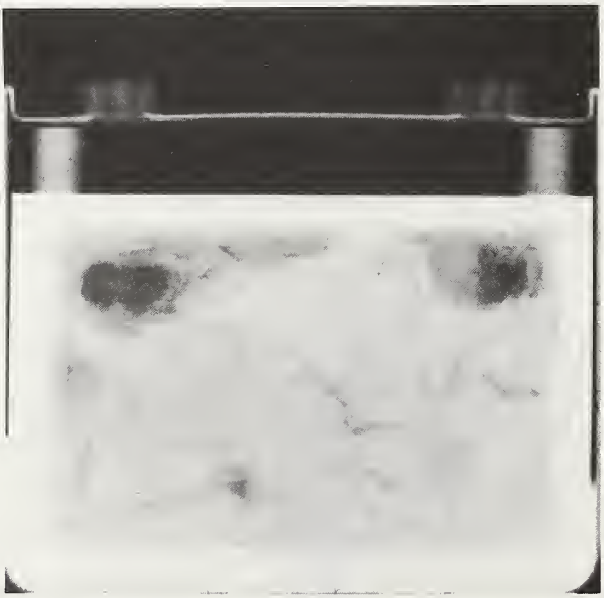

Figure 3. Neutron radiograph of depleted lithium-iodide battery.

Several phenomena could be taking place with battery rundown. Two possible explanations are void formation or selective elemental depletion in the electrolyte. These, however, are only preliminary suggestions. Further experimentation and comparison of neutron and x-radiographic data and destructive analysis of the battery must be carried out. Accordingly, the next step in this project will be to cool the battery to low temperatures, freezing the electrolyte, and slice it into .05 in. (1.27 mm) layers. Visual observations of the battery layers can then be compared with the radiographs for correlation studies in an attempt to explain the chemical kinetics taking place.

CONVERTER SCREEN DEVELOPMENT

D. A. Garrett
and
M. Bevan
(Carnegie-Mellon Institute, Pittsburgh, PA)

The objective of this project is to develop a thermal neutron conversion screen having the following salient features, e.g.

1. High signal to noise ratio.
2. Light emitting upon neutron capture.
3. High speed.

This conversion screen will be employed for field applications in which exposure times must be kept within limits dictated by production rates and satisfactory resolution attained.

The screen which satisfies the second two of the aforementioned criteria is one that employs a physical mixture of Li-6 F and ZnS(Ni) powders held together by either a hydrocarbon or fluorcarbon binder. Although such screens are available commerically, the image produced exhibits a gross grain. In addition, binders have been difficult to obtain since the majority of the vendors consider this material to be proprietary.

A $50^{w}/50^{w}/o$ physical mixture of LiF(∿7% Li-6) ZnS was finely pulverized by hand with a mortar and pessel. An ultraviolet curing adhesive was used as a binder and was able to maintain the physical mixture in suitable suspension during the curing process.

Although much remains to be worked out in the fabrication process, initial experiments have indicated that this basic process results in a light-emitting screen exhibiting appreciably less grain than those commerically available.

Imaging experiments employing Li-6 enriched glass scintillators proved to be disappointing for two reasons. Firstly, these scintillators contain many void pockets, some of which open to the surface. These points act as light scattering centers, causing dark spots to be formed on the radiographic image. The second shortcoming of these scintillators is the light piping which takes place due to the total internal reflections from the smooth scintillator surfaces. It should be noted, however, that if the voids in such scintillators could be eliminated and the surface slightly etched, a high quality conversion screen would result.

B. RRD COLLABORATIVE PROGRAMS

GROUND STATE EXCITATIONS IN $HoCo_2$

J. J. Rhyne

and

N. C. Koon and B. N. Das
(Naval Research Laboratory, Washington, DC)

The Compound $HoCo_2$ crystallizes in the Laves phase C15 structure and orders into a ferrimagnetic spin configuration in a first-order phase transition at 74 K.[1] At low temperatures the measured Ho moment is 9.5 μ_B[2] (essentially equal to the free-ion value of 10 μ_B), and the Co moment[1] is 1.0 μ_B. We have studied the inelastic magnetic scattering at 4 K in the [q, q, 0] and [q, q, q] propogation directions in a single crystal of approximately 0.5 cm using a triple axis spectrometer. The spin wave modes have been analyzed in terms of a RPA pseudo-boson model which allows both the mode energies and intensities to be calculated from the exchange and crystal field interaction parameters. The principal features of the observed inelastic scattering (see figure) are an in-phase spin precession "acoustic" mode with a q = 0 gap of 0.8 meV which is degenerate at the zone boundary with a dispersionless mode of energy 5.8 meV. This latter mode arises from an out-of-phase excitation of the rare earth spins. A second dispersionless mode of lower intensity is observed at 12 meV. These modes are in essential agreement with the model calculation using a Ho-Co exchange field of 2.6 meV, zero Ho-Ho exchange and a ratio of crystal field parameters $A_6/A_4 = .046$. The absence of Ho-Ho exchange is a feature common to both Co and Fe Laves phase systems and results in the flat modes mentioned above. The model further predicts an in-phase mode of the cobalt spins starting from approximately 15 meV at q = 0. This mode has not been observed in these scattering studies nor in previous experiments on $ErCo_2$. It is not known if this is a result of insufficient scattering intensity in this mode or if the mode is highly damped because of Stoner band-like excitations present even at relatively low q.

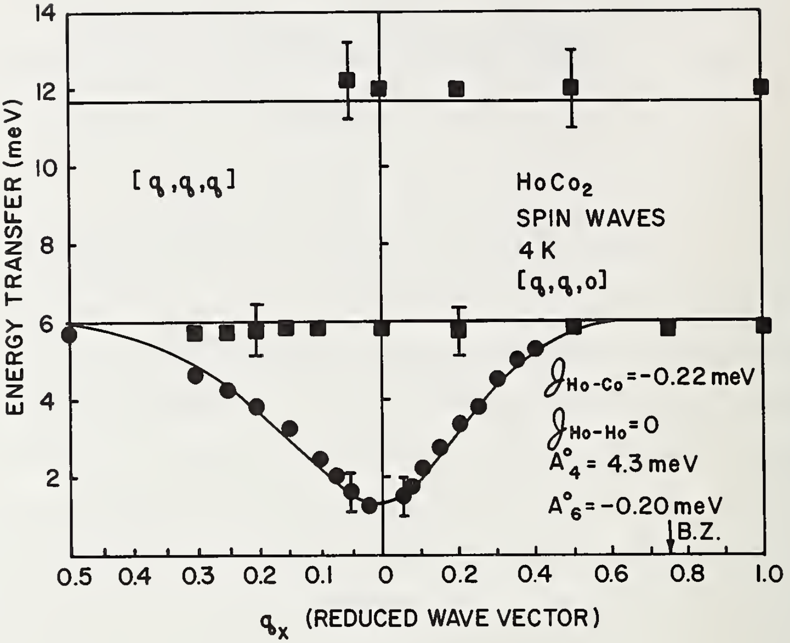

Figure 1. Inelastic magnetic scattering in HoCo$_2$ at 4 K for the [q,q,0] and [q,q,q] propagation directions. The lower mode spin wave groups were measured about the [111] and [220] reflection and the flat modes at the [002] and [222] respectively, as determined from dynamic structure factor considerations. The solid line is the result of a RPA model calculation using the exchange and crystal field parameters shown in the figure.

---

1. D. Gignoux, F. Givord and R. LeMaire, *Phys. Rev. B.* 12, 3878 (1975).

2. R. M. Moon, W. C. Koehler and J. Farrell, *J. Appl. Phys.* 36, 978 (1965).

MAGNETIC EXCITATIONS IN $ErCo_2$

N. C. Koon
(Naval Research Laboratory, Washington, DC)

and

B. N. Das
(Naval Research Laboratory, Washington, DC)

and

J. J. Rhyne

We have measured the magnetic excitation spectrum of $ErCo_2$ at 4.2 K using neutron inelastic scattering and compared the results to a Green's function RPA theory of magnetic excitations in a ferrimagnet with crystalline electric fields. At the zone center [111] two modes are clearly resolved, one at 8.2 meV and another at 11 meV. The width of the 8.2 meV is almost equal to the instrumental resolution, while the 11 meV mode is considerably broader, and about 5 times more intense than the 8.2 meV mode. Both modes exhibit a weak q dependence in the [111] zone. Based on dynamic structure factor considerations we conclude that each of the observed scattering peaks consists of two nearly degenerate excitations, one of which corresponds to out-of-phase precession of the two rare earths in the primitive cell, while the other corresponds to in-phase precession. The in-phase excitations are observed at [111] but not at [002] and have a weak q dependence, while the out-of-phase modes are essentially q independent. By comparing these results with a Green's function RPA theory we are able to determine the Er crystal field parameters as well as the Er-Co mean exchange field. From the lack of dispersion in the out-of-phase modes we conclude that the Er-Er exchange is very weak, just as was found for RFe_2 compounds. The mean field exchange and crystal field constants for the rare earth spins are $gu_B H_{exch}$ = 2.0 meV, A_4^0 = 4.3 meV, and A_6^0 = -0.15 meV. A spin wave mode due mainly to excitation of the Co spins is predicted but not observed, probably due to much weaker scattering intensity than the predominantly rare earth modes.

NEUTRON SCATTERING MEASUREMENTS ON AMORPHOUS $NdFe_2$

H. A. Alperin
(Naval Surface Weapons Center, White Oak, MD)

and

(National Bureau of Standards, Washington, DC)

S. J. Pickart
(University of Rhode Island, Kingston, RI)

and

J. J. Rhyne

Earlier measurement [1,2,3,4,5] on bulk amorphous rare-earth-iron alloys incorporating heavy rare earths showed the following general features: i) A dense random close-packed amorphous structure, ii) Lorentzian neutron scattering above T_c characterized by a correlation length which remained finite at T_c, iii) Below T_c, intense small angle scattering due to the presence of small magnetic inhomogenieties, characterized by a q^{-3} dependence of the intensity on wave vector, q, iv) Large coercive fields, H_c increasing with decreasing temperature. In the present study, the effect of a light rare earth element on these characteristics was investigated.

The sample was a disc 1 mm in thickness and 5 cm in diameter, prepared by rapid sputtering. An incident wavelength of 0.91 A was used to determine the amorphous structure. Small angle scattering was observed between 5 and 400 K with two techniques: a double axis spectrometer with a 10' slit system with 2.38 A neutrons covering the wavevector range $.03<q<.12$ A and a small angle scattering spectrometer with a linear position-sensitve detector with neutrons of 7.2 A for q down to .01 A. Inelastic neutron scattering measurements were made at room temperature with a triple axis spectrometer at 2.36 A.

A diffraction pattern taken at room temperature shows a split first peak and pronounced structure at higher angles; features not present in the patterns for the heavy rare earth alloys which have been explained by a dense random packing (DRP) of iron atoms (with radii of 1.27 A) and rare earth atoms with their 12-fold coordination radii.

The pair correlation function for $NdFe_2$ obtained by Fourier inversion of the diffraction pattern is given in figure 1 and shows first neighbor peaks at 2.54, 3.15, and 4.25 A. The peak at 2.54 A is at the position expected for the nearest neighbor Fe atoms in the DRP model; however, the other peaks cannot be correlated with combinations of the radii of Nd (1.83 A) and Fe atoms as predicted by the DRP model. This lack of agreement is certainly unexpected particularly in light of the other amorphous rare earth alloy results and is not understood at present.

The small angle scattering as a function of temperature taken on the double axis instrument is plotted in figure 2. The critical scattering peak (as determined from a measurement at $q = .03$ with finer temperature control) is well-defined at 305 K and is more pronounced than that seen in any of the heavy rare earth alloys. The intense scattering at low temperatures is comparable in magnitude to that observed in $TbFe_2$,[1] and bacause it is not present above T_c and scales with σ_o^2 it must be magnetic in origin. Above T_c the data can be fitted with a Lorentzian in q, which yields correlation length $\kappa^{-1} \sim 60$ A at 313 K. The intensities at low temperature can be analyzed as an inverse power law dependence on wavevector q $(= 4\pi \sin\theta/\lambda)$. We find approximately that the intensity $I \propto q^{-3}$.

Inelastic neutron scattering was measured at room temperature where σ_o has attained ~ 0.4 of its full value. Nevertheless, no energy broadening of the elastic peak and no well-defined excitations (at wavevectors $0.1 < q < 0.28$ A^{-1}) could be observed. The latter result is not completely unexpected since the wings of the particularly large elastic small angle scattering component can effectively mask the low q spin wave scattering.

The usual negative exchange between the rare earth and iron aligns their spins oppositely. In the heavy rare earth alloys where the total quantum number $J = L+S$, this leads to a ferrimagnetic alignment of the iron and rare earth moments $(\mu_R = g_J J)$, but for light rare earth atoms

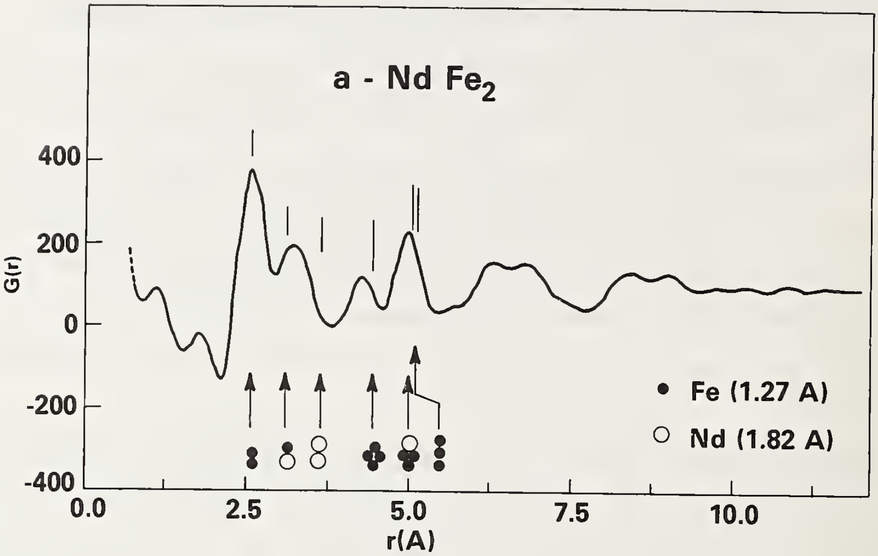

Figure 1. Reduced radial distribution function $G(r) = 4\pi r^2 \rho(r)$, for amorphous $NdFe_2$. The arrows give the calculated positions for some of the atom configurations in a DRP model.

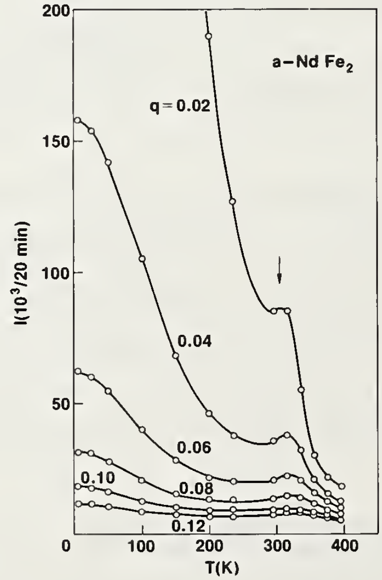

Figure 2. Small angle neutron scattering intensity I vs. temperature, corrected for absorption and background.

where the 4f shell is less than half filled, $J = L - S > 0$ and ferromagnetism results. It is clear, however, that if one takes the iron moment to be 1.6 μ_B (as obtained from amorphous $GdFe_2$), in order to explain the observed net moment of 1.3 μ_B/atom, a neodymium moment of only 0.7 μ_B is required instead of the full Nd^{3+} moment of 3.27 μ_B. This implies a higher degree of disorder of the rare earth moment in $NdFe_2$ than, for example, in $TbFe_2$. In this case the disorder presumably comes from the combination of a very weak Nd-Fe exchange coupling and a strong random direction axial magnetic anisotropy which results in a significant "fanning" or local fluctuation of the moment direction about the direction of the average exchange field.

The high degree of disorder of the neodymium moments apparently does not affect the general features previously found for the heavy rare earth alloys, $TbFe_2$, $HoFe_2$, and $Tb_{.018}Fe_{.982}$ as enumerated above. In particular, the arrested divergence of the correlation length when $T \to T_c$ from above and inhomogeneous clustering of a complicated nature in the ordered state appear to be general features of all amorphous rare earth alloys with large rare earth orbital moments.

---

1. S. J. Pickart, J. J. Rhyne, H. A. Alperin, *Phys. Rev. Letters* 33, 424 (1974).
2. S. J. Pickart, J. J. Rhyne, H. A. Alperin, *AIP Conf. Proc.* 24, 117 (1975).
3. H. A. Alperin, J. R. Cullen, A. E. Clark, E. Callen, *Physica* 86-88B, 767 (1977).
4. S. J. Pickart, H. A. Alperin, J. J. Rhyne, *Phys. Letters* 64A, 337 (1977).
5. H. A. Alperin, S. J. Pickart, J. J. Rhyne, *J. Appl. Cryst.* 11, 648 (1978).

MAGNETIC EXCITATIONS IN $TbFe_2$

J. J. Rhyne

and

N. C. Koon
(Naval Research Laboratory, Washington, DC)

and

H. A. Alperin
(Naval Surface Weapons Center, White Oak, MD)

and

(National Bureau of Standards, Washington, DC)

Magnetic inelastic scattering studies have been performed as a function of temperature on $ErFe_2$[1], $HoFe_2$[2] and $TbFe_2$. All the heavy rare earth iron compounds of composition RFe_2 crystallize in the C15 Laves phase structure with lattice constants $a_o \approx 7.3$ A. They have Curie temperatures in the range 575 K to 700 K and exhibit a ferrimagnetic alignment of iron and rare earth spins. The iron moment is typically 1.5 μ_B, and the rare earth has the full free ion moment at 0 K.

The six atoms in the primitive unit cell give rise to six ground-state spin wave modes, only three of which are at energies low enough to investigate by thermal neutron scattering. A linear spin wave model has been utilized[1] for these compounds which accurately represents these three modes as shown in the previous work on $HoFe_2$ and $ErFe_2$. Figure 1 shows the results of this model calculation compared to the observed excitation groups in $TbFe_2$. The lower "acoustic" mode corresponds to an in-phase precession of all spins with a bandwidth determined principally by the rare earth-iron exchange. The flat mode which, in contrast to $ErFe_2$ and $HoFe_2$, has not been observed in this study of $TbFe_2$, represents an out-of-phase precession of the rare earth spins. The highest steeply-dispersive mode is an in-phase precession of the iron-spins. This mode, which was observed in the previous studies of $HoFe_2$ and $ErFe_2$, has a dispersion ($\omega = Dq^2$) nearly identical to that in iron metal. The absence of scattering in $TbFe_2$ corresponding to the two higher modes is not understood, although it would be expected to be weak due to the small size of the crystal and the relatively higher energy of the modes in $TbFe_2$. The values shown in the figure for the Fe and Tb angular momenta have been determined in a separate magnetic diffraction experiment. The terbium-iron exchange parameter was determined from fitting the model to the observed acoustic-mode data, while the remaining two exchange constants were fixed at values found from the previous $HoFe_2$ and $ErFe_2$ studies.

An anomalous broadening and decrease in intensity of the spin wave groups at all temperatures studied was observed for $q > 0.15$ A^{-1}. For q values larger than those shown, the spin waves were not resolvable.

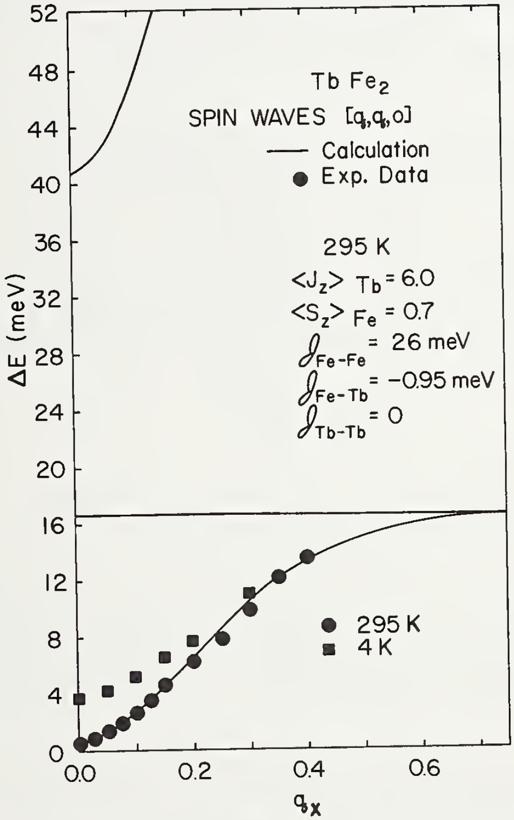

Figure 1. Inelastic magnetic scattering data and model calculation for $TbFe_2$. Acoustic mode results are shown for both room temperature and 4 K where the q = 0 gap is increased to 3.75 meV due to the crystal field anisotropy.

This effect may result from lifetime broadening or by spurious scattering from additional crystallites which effectively make q an invalid quantum number except for $q \approx 0$.

---

1. J. J. Rhyne, N. C. Koon, J. B. Milstein and H. A. Alperin, "Spin Waves in $ErFe_2$," *Physica* 86-88B, 149 (1977) and N. C. Koon and J. J. Rhyne, "Excited State Spin Waves in $ErFe_2$," *Solid State Commun.* 26, 537 (1978).

2. J. J. Rhyne and N. C. Koon, "Magnetic Excitation in $HoFe_2$," *J. Appl. Phys.* 19, 2133 (1978).

MAGNETIC ORDERING AND DYNAMICS IN Tb-Sc ALLOYS

G. E. Fish and J. J. Rhyne

and

B. J. Beaudry and K. A. Gschneidner
(Ames Laboratory, Iowa State University, Ames, IA)

Alloys of the heavy rare earths with each other and with non-magnetic La, Lu, and Y have been shown to obey a universal relationship between magnetic ordering temperature and averaged deGennes factor:

$$T \propto [\sum_i C_i G_i]^{2/3}$$

where C_i is the concentration of the i-th species and

$$G = (g_J - 1)^2 J(J + 1)$$

for each ion with spin J and Landé g-factor g_J.[1] This behavior comes from the indirect, long-range character of the RKKY exchange interaction coupling the magnetic atoms, and results in ordering even in magnetically dilute systems.

The system R_xSc_{1-x}, where R is any heavy rare earth, is anomalous, however, in that $x \sim 0.25$ is required to induce long range ordering. Previous magnetization and Mossbauer effect studies have suggested the possibility of a spin-glass transition for lower concentration. The

Tb_xSc_{1-x} system is ideal for study of these phenomena because of the large free ion moment of Tb ($9\mu_B$) and because large, high quality single crystals are available. Accordingly, we have taken both elastic and inelastic neutron scattering data on samples grown at the Ames Lab with $x = 0.2$, 0.4, and 0.85. Previous work on polycrystalline samples[3] and 0.85. We have confined previous work on polycrystalline samples[3] indicated that for $0.25 \lesssim x \leq 1.0$, Tb_xSc_{1-x} orders in a basal phase spiral (see table 1). For pure Tb, there is also a ferromagnetic transition at $T_c = 221$ K, but we saw no ferromagnetism at 4 K in the $x = 0.85$ sample. For $x = 0.2$, there was no evidence of any long-range magnetic ordering, but weak, satellite peaks $(00\ell\pm)$ begin to develop. From the breadth of these satellites, we estimate that even at 4 K the magnetic correlation lengths are at most a few atomic distances. There is no evidence that the ordering in the $x = 0.4$ sample is anomalous in any way. We also attempted to induce ferromagnetic order in the $x = 0.4$ sample at $T = 8$ K with an applied field. For $H \leq 60$kOe, the spiral phase persists with slight decrease in turn angle, and slight increase in the satellite peak width.

Table 1. Magnetic ordering in Tb_xSc_{1-x}

x	T_N (K)	Turn angle (deg)	T_N (K)	Reference
1.0	230	19.8*	221	a
0.85	189	25.6+	-	a, b
0.4	-	46.1+	-	b
0.2	-	46.8+	-	b

*At 77 K

+At 10 K

a. Child & Koehler, Phys. Rev. 174, 562 (1968).

b. This work.

Inelastic scattering studies are also in progress. Well-defined spin waves have been seen in the ordered state of the x = 0.85 system but not for x = 0.4 or 0.2. These results contrast wtih data on rare earth-Y alloys, in which spin wave dispersion relations have been measured for very dilute systems, e. g. $H_{0.1}Y_{0.9}$, and $Tb_{0.1}Y_{0.9}$.[4] This suggests that the marked reduction in Fermi surface density of states Sc (as compared to Y and the other rare earths) may affect the spin-wave lifetimes.

---

1. Bozorth, R. M., *J. Appl. Phys.* 38, 1366 (1967).

2. Sarkissian, B. V. B., Coles, B. R., *Commun. Phys.* 1 17 (1976) and Abbundi, R., et. al., *Phys. Rev. B.* 18 331 3 (1978).

3. Child, H. R., and Koehler, W. C., *Phys. Rev.* 174, 562 (1968).

4. Wakabayashi, N. and Nicklow, R. M., *Phys. Rev.* B10, 2049 (1974).

SUBLATTICE MAGNETIZATION AND STRUCTURE OF HYDRIDES OF THE LAVES PHASE RARE EARTH COMPOUNDS RFe$_2$

G. E. Fish and J. J. Rhyne

and

S. G. Sankar and W. E. Wallace
(University of Pittsburgh, Pittsburgh, PA)

and

T. Brun, P. J. Viccaro, D. Niarchos, B. D. Dunlap, and G. K. Shenoy
(Argonne National Laboratory, Argonne, IL)

We have used neutron scattering to study the structure and magnetic ordering of a series of hydrides and deuterides of the rare earth-iron compounds RFe$_2$. The parent RFe$_2$'s have the cubic close packed Laves phase (C15) structure for R heavier than Nd and order ferrimagnetically at ∿600 K with the full free ion moment on each R and ∿ 1.6μ_B/Fe (depressed from the $2.2\mu_B$ in Fe metal) at saturation. The stable hydride phases with ~ 2 and ~ 3.5 H(D) per formula unit are known from x-ray and neutron diffraction to retain the C15 cubic structure, with lattice parameters increased by $\sim 5\%$ and $\sim 7\%$.[1,2] The RFe_2H_4 phase is rhombohedrally distorted and is not ordered at 4.2 K[3].

Figure 1 shows the temperature dependences of magnetization of Er and Fe sublattices obtained by neutron scattering for $ErFe_2$, $ErFe_2D_2$, and $ErFe_2D_{3.5}$. These data are typical of results summarized in table 1 for all the RFe_2H_2 and $RFe_2H_{3.5}$'s studied. The Fe moment either is unchanged or is raised by a slight amount (comparable to experimental error), while the coherent R moment drops substantially. The lowering of T_c in the hydrides signals a reduction in the Fe-Fe exchange which is known to dominate in the parent RFe_2's. The R-Fe exchange, weak in RFe_2, is further lowered, particularly in the case of $ErFe_2D_{3.5}$, where the Er sublattice disorders well below the overall T_c.

The sizeable reduction of R moment seen in all the systems studied can arise in two ways. First, it is clear that introduction of H weakens the exchange interaction in these materials, resulting in lowered T_c and in the case of the $ErFe_2$ series, complete disorder of the R spins well below T_c where the Fe sublattice disorders. This may allow the crystal field to significantly perturb the exchange-split J_z states. Alternatively, the colinear spin ordering of R seen in the parent RFe_2's may be broken in the hydrides.

The sublattice moments have also been inferred from measurements of hyperfine fields using Mössbauer spectroscopy.[2,3] These experiments, which are sensitive to the local moment and not the coherent spatial average seen in neutron diffraction, give identical results for the Fe moment, but nearly the full free ion moment for R in both the RFe_2D_2 and $RFe_2D_{3.5}$ phases. This indicates that the crystal field does not significantly perturb the R wavefunctions.

Hence, we conclude that the rare earth spins in the RFe_2 hydrides are not ordered in a unique direction. The random hydrogen site occupancy

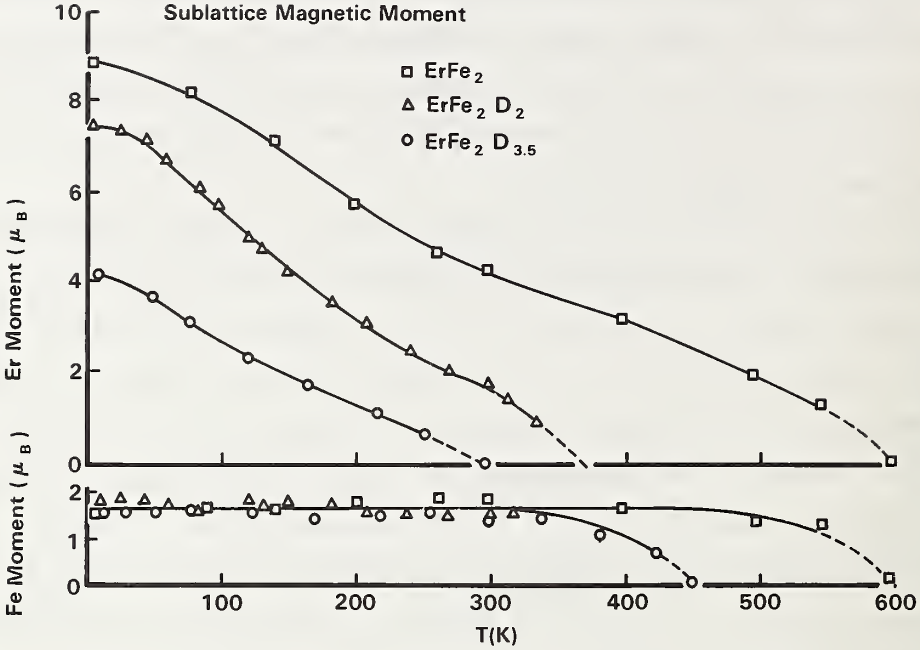

Figure 1. Magnetization of Er and Fe sublattices in $ErFe_2$, $ErFe_2D_2$, and $ErFe_2D_{3.5}$. Curie temperature (T_c) for $ErFe_2$ and $ErFe_2D_{3.5}$ were determined by bulk magnetization. For $ErFe_2D_2$, desorption begins below T_c, so moments were determined using a smooth extrapolation of diffraction peak intensity to the nuclear limit.

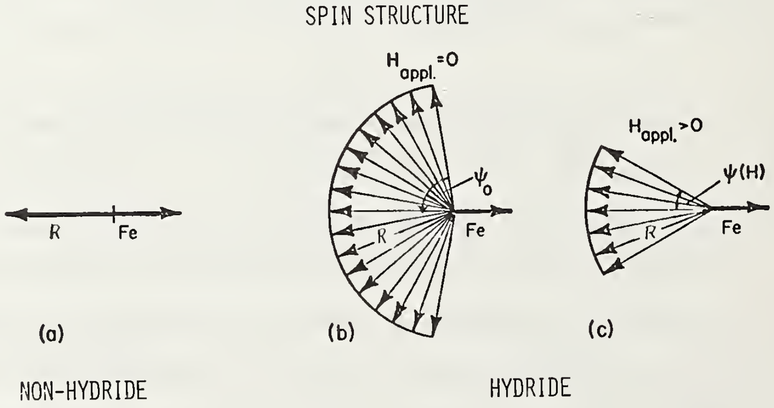

Figure 2. Schematic diagram of spin ordering showing the colinear anti-parallel arrangement in RFe_2 and the fanning of R spins upon hydriding. The disorder increases with higher H content. Application of a magnetic field $\vec{H}$ partially aligns the R spins.

Table 1. Structural and magnetic properties of Laves-phase RFe_2 compounds and their hydrides and deuterides. The saturation moment of the R and Fe sublattices as determined by neutron scattering are shown, along with theoretical free ion moment for each R.

	Lattice Parameter (A)	Bulk Curie Temperature (K)	Rare Earth Moment		Fe Moment (μ_B)
			Free ion	Saturation	
$ErFe_2$	7.28	574	9	8.8	1.6
$ErFe_2D_2$	7.60	(a)	9	7.5	1.7
$ErFe_2D_{3.5}$	7.67	440	9	4.3	1.6
$ErFe_2H_{3.5}$	7.83	450	9	4.9	1.5
$HoFe_2$	7.30	612	10	10	1.7
$HoFe_2D_{3.5}$	7.81	295	10	5.3	1.9
$TmFe_2$	7.25	610	7	7	(b)
$TmFe_2H_{3.5}$	7.77	305	7	3.8	(b)

(a) Desorption of D begins at ∿ 330 K, so that T_c cannot be determined.

(b) Not measured

undoubtedly results in variation in the direction of the local anisotropy field, such as found in amorphous rare earth alloys, which leads to a "fanning" of the individual rare earth **moments** illustrated in figure 2.[4] This would account for the reduction in overall sublattice magnetization and the incomplete saturation in applied fields $\lesssim$ 100 kOe.[5]

---

1. Fish, G. E., Rhyne, J. J., Sankar, S. G., and Wallace, W. E., *J. Appl. Phys.* 50, 2003 (1979).
2. Viccaro, P. J., Friedt, J. M., Niarchos, D., Dunlap, B. D., Shenoy, G. K., Aldred, A. T., and Westlake, D. G., *J. Appl. Phys.* 50, 2051 (1979).
3. Viccaro, P. J., Shenoy, G. K., Dunlap, B. D., Westlake, D. G., and Miller, J. F., *Journal de Phys.* 40, C2-198 (1979).
4. Rhyne, J. J., Schelleng, J. H., and Koon, N. C., *Phys. Rev.* B10, 4672 (1974(.
5. Gualtieri, D. M., Narasimhan, K. S. V. L., and Takeshita, T., *J. Appl. Phys.* 47, 3432 (1976).

LOW TEMPERATURE PHASE TRANSITION IN $Cs_2NaPrCl_6$

G. E. Fish and J. J. Rhyne

and

J. W. Lynn
(University of Maryland, College Park, MD)

and

(National Bureau of Standards, Washington, DC)

and

H. H. Patterson
(University of Maine, Orono, ME)

A single crystal of $Cs_2NaPrCl_6$ has been studied by neutron scattering to characterize the structural phase transition from the high temperature cubic phase (space group Fm3m) to a phase of lower but unknown symmetry at 155 K. The structurally similar system K_2ReCl_6 is known to undergo two second-order transitions driven by softening of the phonon branch which rotates $(ReCl_6)^{2-}$ octahedra, first at the Γ-point (111 K and then at the X-point (103 K).[1] Preliminary inelastic neutron data on $Cs_2NaPrCl_6$ reveal a soft phonon at the Γ-point of ∿ 2 meV and width considerably broader than resolution. Further data are being taken to characterize this phonon and determine if the 155 K phase change is a second-order transition driven by phonon softening analogous to that in K_2ReCl_6.

Table 1. Structural refinements of the high temperature phases $C_{s2}N_aP_rCl_6$ and $K_2R_eCl_6$

Space Group - Fm3m

Positions:	Cs (1/8, 1/8, 1/8), (7/8, 7/8, 7/8)	K (1/8, 1/8, 1/8), (7/8, 7/8, 7/8)
	Na (1/2 , 0, 0), (0, 1/2, 0), (0, 0, 1/2)	
	Pr (0, 0, 0)	Re (0, 0, 0)
	Cl (U,0,0),(00U) (0U0) U = 0.247±0.002	Cl (U00),(0U0),(00U) U= 0.234±0.002
Lattice constant (Å)	10.90	9.835
Temperature:	295 K	175 K
Thermal Parameters:	Cs 3.42±0.19	K 3.01±0.17
	Na 1.55±1.15	
	Pr 0.65±0.63	Re 1.05±0.09
	Cl 1.89±0.20, 5.43±0.14	Cl 1.08±0.11, 3.84±0.09
R-factor	9.00 7.72 (expected)	9.86 8.10 (expected)

A powder sample of $Cs_2NaPrCl_6$ form has been prepared and its 295 K diffraction pattern analyzed using the total profile analysis technique of Rietveld.[2]

Results of this refinement and similar analysis for K_2ReCl_6 are shown in table 1. Of particular interest are the strongly anisotropic thermal factors of Cl. In both systems, the amplitude of vibration along the cubic 4-fold axis (connecting Cl to nearest neighbor Re or Pr) is much smaller than that in the perpendicular directions as expected in the soft phonon model.

---

1. Lynn, J. W., Patterson, H. H., Shriane, and Wheeler, R. G., *Solid State Comm.* 27, 859 (1978).
2. Rietveld, H. M., *J. Appl. Cryst.* 2, 65 (1969).

MAGNETIC PROPERTIES OF CHEVREL PHASE SUPERCONDUCTORS

J. W. Lynn
(University of Maryland, College Park, MD)
and
(National Bureau of Standards, Washington, DC)
and
R. N. Shelton
(Ames Laboratory, Ames, IA)

The ternary Chevrel-phase superconductors, RMo_6X_8 (R-rare earth; X=Se,S), exhibit a variety of unique and interesting phenomena related to the interplay between magnetism and superconductivity.[1] In all these materials the magnetic ordering temperatures are typically 1K or less, so that we may anticipate that the crystal field splittings of the rare earth ions may dominate the magnetic energies and thus determine the magnetic (or nonmagnetic) properties at low temperatures.

To investigate these materials we have carried out neutron scattering experiments on $ErMo_6Se_8$, $TbMo_6Se_8$, $HoMo_6Se_8$ and $HoMo_6S_8$ as a function of temperatures and magnetic field. Figure 1 shows data on $HoMo_6Se_8$ at 4K. An excitation is clearly seen at 4.58 meV, and there is additional scattering at low energies which, under higher resolution, can be identified as

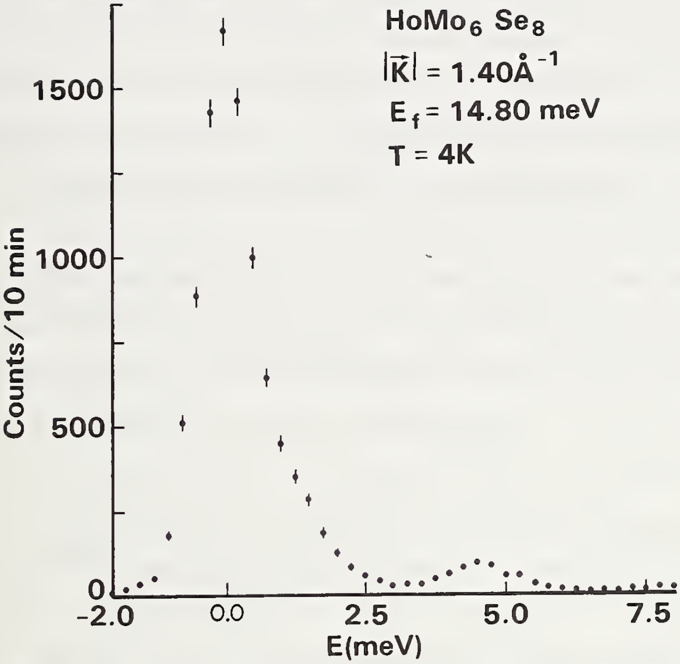

Figure 1. Observed crystal field scattering at low temperatures in $HoMo_6Se_8$. Under high resolution the scattering at low energies is identified as a crystal field transition at 1.06 meV.

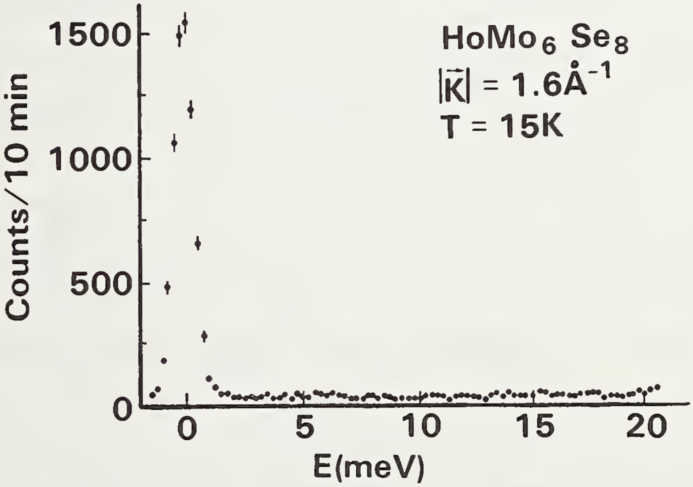

Figure 2. Spectrum at low temperatures for $HoMo_6S_8$, showing that there are no crystal field transitions in this energy range. There are also no transitions observed in the peak at E=0 under high resolution (98 μeV FWHM).

another excitation at 1.06 meV. This scattering has been uniquely identified as crystal field in origin since i) the energy of the scattering is independent of the wavevector transfer $\vec{K}$, ii) the intensity decreases with increasing temperature, in contrast to Bose excitations whose intensity increases with temperature, and iii) the intensity as a function of $\vec{K}$ quantitatively follows the magnetic form factor $f(\vec{K})$.

The observance of crystal-field transitions in $HoMo_6Se_8$ is characteristic of the selenide materials, in which crystal field transitions have been found in all the compounds studied to date.[2] The overall crystal-field level scheme can be described to a first approximation by a cubic crystal field; additional splittings due to the perturbations from cubic symmetry which are present may be treated as second-order effects. A cubic crystal field is indeed capable of explaining the data in each case, and the ground states are found to be magnetic in agreement with specific heat, susceptibility and previous neutron diffraction data.

In contrast to the behavior observed in the selenide materials, figure 2 shows data for $HoMo_6S_8$. No crystal field transitions are observed over this energy range. We conclude from this that either the strength of the crystal field is more than an order of magnitude larger or smaller than the selenide, or that the line-widths are an order of magnitude larger. To determine if the crystal field transitions are unresolved in the peak at E=0, high resolution (0.098 meV FWHM) measurements were carried out; only the scattering at E=0 was observed with a width that was solely instrumental in origin. To establish that the crystal-field splittings were not still unresolved, inelastic measurements were performed in a magnetic field. The intensity of the scattering at E=0 decreased by a factor of three, but still no (Zeeman) transition was observed. The Ho ion therefore does not behave as a J=8 free ion. We remark that essentially the full moment was induced with a field of 20 kOe or larger at 4.5K, while in the selenide materials the moments induced are considerably small than the free-ions values. Figure 3 shows the peak intensity of the {110} Bragg peak as a function of field for $ErMo_6Se_8$. The scattering at H=0 is due to the nuclear Bragg peak plus background. Comparison of the induced magnetic intensity with the nuclear intensity gives an induced moment $\mu_z=3.9\mu_B$ at 70 kOe. Similar data on $HoMo_6Se_8$ gave a moment of $5.9\mu_B$. These field-dependent diffraction data are also a very sensitive technique for determining what, magnetic impurity phases, if any, are present in these samples. For the $REMo_6Se_8$ materials the only significant magnetic impurity phase present is $(RE)_2O_2Se$, at the few percent level in volume. It has been determined that this phase is not responsible for the magnetic phase transitions or crystal field excitations observed in these materials.

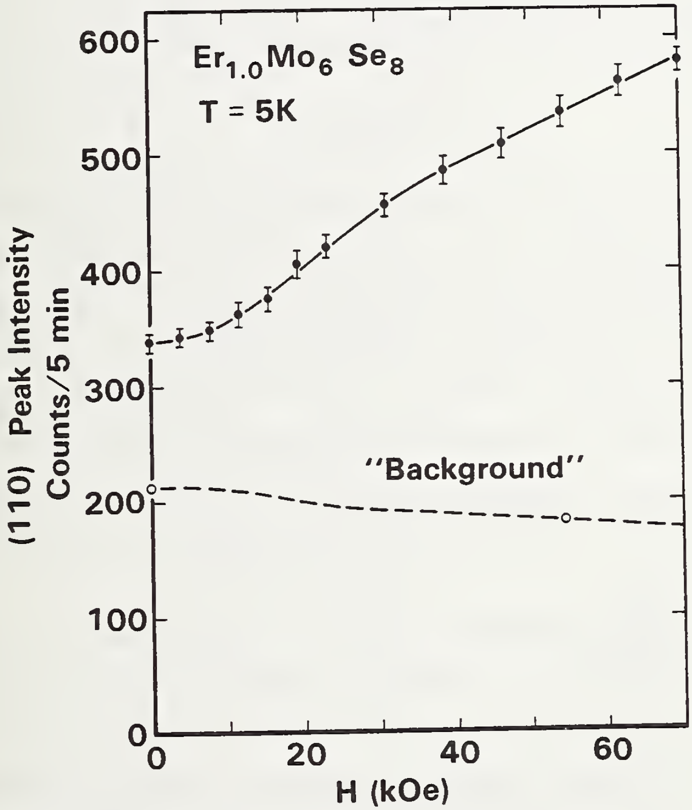

Figure 3. Intensity of the {110} Bragg peak as a function of applied magnetic field for $ErMo_6Se_8$. The observed increase in intensity is due to the induced magnetic moment.

---

1. See, for example, Ø. Fischer, *Appl. Phys.* 16, 1(1978).

2. J. W. Lynn and R. N. Shelton, J. *Appl. Phys.* 50, 1984 (1979).

3. J. W. Lynn, D. E. Moncton, W. Thomlinson, G. Shirane and R. N. Shelton, *Sol. St. Comm.* 26, 493 (1978).

MAGNETIC PROPERTIES OF THE SUPERCONDUCTING ALLOY SYSTEM $(Ce_{1-c}Ho_c)Ru_2$

J. W. Lynn
(University of Maryland, College Park, MD)
and
(National Bureau of Standards, Washington, DC)
and
C. J. Glinka

In the magnetic superconductor system $(Ce_{1-c}Ho_c)Ru_2$, Ho concentrations in excess of 30% are needed in order to completely suppress the superconducting state, while bulk susceptibility data above 27% Ho show distinct maxima as a function of temperature which are suggestive of long range magnetic order[1]. Additional evidence of the coexistence of superconductivity and magnetic order is provided by Mossbauer experiments[2], which reveal the development of a hyperfine splitting below the (extrapolated) magnetic phase boundary in the "coexistence" region of concentration (~27% Ho)[1].

To investigate the microscopic magnetic properties of this system we have carried out elastic and inelastic neutron scattering measurements as a function of temperature and magnetic field. Samples of 10%, 32% and 38% Ho, which cover the range from below to above the coexistence regime, were prepared by arc melting and subsequent heat treatment. Low temperature neutron powder diffraction measurements were employed to establish the concentrations to within 1%; the intensities of 18 peaks were used to refine two parameters, the ratio of Ce to Ho in the C-15 crystal structure and an overall scale factor.

Previous measurements on a 27% Ho alloy revealed the development of ferromagnetic correlations at low temperatures[3]. However, the correlation range was found to saturate at 0.5 K with no transition to long range magnetic order. If this truncation were due to a competition with the superconducting state, than at sufficiently high Ho concentrations, where the superconductivity is suppressed, a conventional ferromagnetic phase transition might occur. To test this conjecture we have carried out small-angle scattering measurements on the 38% alloy. Figure 1 shows that the scattering at small wavevectors increases with decreasing temperature, signaling the development of ferromagnetic correlations.

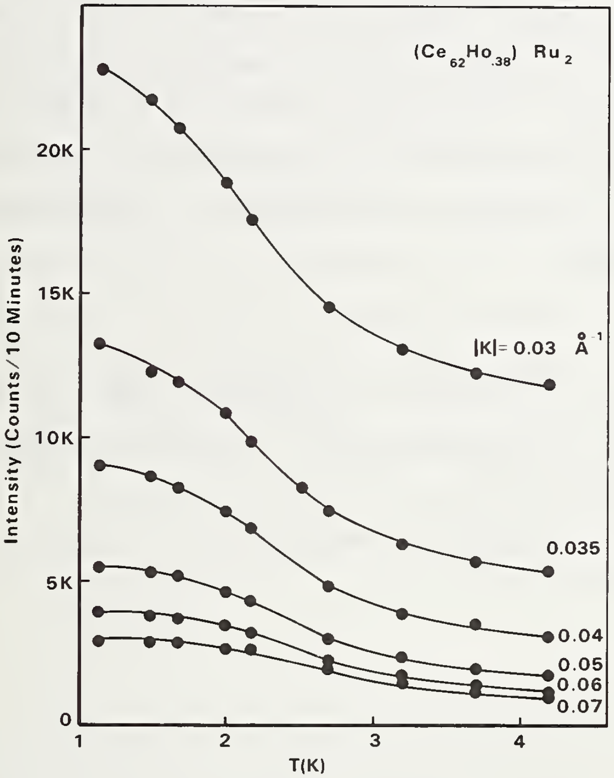

Figure 1. Temperature dependence of the scattering for the 38% Ho alloy at a series of wavevectors.

However, no peak in the intensity as a function of temperature, which would be characteristic of a ferromagnetic phase transition, is found; rather the scattering in the wavevector range 0.05 → 0.14 A^{-1} increases with decreasing temperature down to ∿2K and then shows little further change, while at smaller wavevectors (down to 0.01 A^{-1}, the smallest wavevector measured) the intensity continues to increase slowly. Comparison of the data with an Ornstein-Zernike correlation function suggests that the range of correlations exceeds 100 A at low temperatures, although this form for the correlation function gives a reasonable fit to the data only over a rather limited wavevector range. Thus even at Ho concentrations above the "coexistence" region the system appears to undergo a spin-freezing rather than a conventional ferromagnetic phase transition. We remark, however, that with such a large correlation range it becomes difficult experimentally to distinguish between these two cases. Indeed, for the 38% alloy we observe a small enhancement of the {111} peak below T∿2K.

---

1. M. Wilhelm and B. Hillenbrand, Z. *Naturf.* 26a, 141 (1972)

2. D. J. Erickson, C. E. Olsen and R. D. Taylor, *Mossbauer Effect Methodology* 8, 73 (1973)

3. J. W. Lynn, D. E. Moncton, L. Passell and W. Thomlinson *Phys Rev. B* (to be published)

SPIN WAVE AND DYNAMIC CRITICAL SCATTERING IN AMORPHOUS Fe_{40} Ni_{40} P_{14} B_6

J. W. Lynn
(University of Maryland, College Park, MD)
and
(National Bureau of Standards, Washington, DC)
and
J. J. Rhyne

The magnetic properties of the structurally amorphous ferromagnetic $Fe_{40}Ni_{40}P_{14}B_6$ are of particular interest because of the high permeability and extremely low coercive field this system exhibits. These properties lead not only to important commercial applications but are also interesting from a basic theoretical point of view since they imply nearly ideal isotropic behavior. The isotropy of the system has important implications with regard to the nature of the magnetic excitations in the system, namely that at long wavelengths these excitations are of the traditional spin wave type with a dispersion relation which approaches zero as the wavevector approaches zero (Goldstone's theorem).

To investigate these excitations we have carried out inelastic neutron scattering measurements using the triple-axis technique. In the small wavevector region the dispersion relation is expected to follow

$$E_{SW} = D(T) \; |\vec{K}|^2 \qquad (1)$$

where D(T) is the spin wave stiffness coefficient, which is temperature dependent. In the range of wavevectors $\vec{K}$ accessible ($0.06 \rightarrow 0.14$ A^{-1}) we find equation 1 is indeed obeyed. Figure 1 shows D as a function of temperature, and we find that above room temperature D(T) can be well represented by

$$D = D_o \left|\frac{T_c - T}{T_c}\right|^x \qquad (2)$$

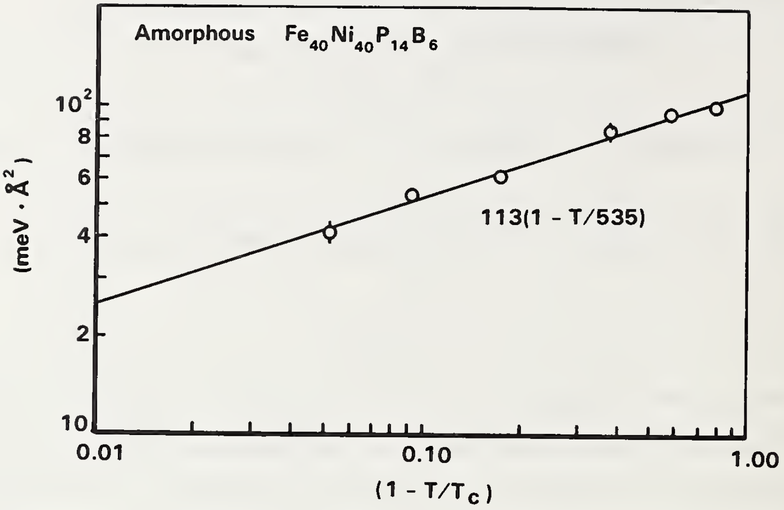

Figure 1. Temperature dependence of the spin wave stiffness coefficient.

with $T_c = 535$ K and $X \simeq 0.33$. As with other isotropic ferromagnets, we find the approximate relation $X \simeq \beta$, where β is the critical exponent describing the collapse of the order parameter. This is not the exponent expected from dynamic scaling theory, but in view of the relatively large wavevectors that the data represent, this cannot be viewed as a failure of the theory. We also searched for a longitudinal component to the susceptibility below T_c; no evidence for this component was observed, as is the case in other isotropic ferromagnets (except for CoS_2 only).

HIGH DENSITY LIPOPROTEIN RECOMBINANTS: EVIDENCE FOR A BICYCLE TIRE MICELLE STRUCTURE OBTAINED BY NEUTRON SCATTERING AND ELECTRON MICROSCOPY

A. Wlodawer
and
J. P. Segrest
(University of Alabama Medical Center, Birmingham, AL)

We have studied the size and shapes of discoidal complexes of Apo

A-I, the major protein of high density lipoproteins (HDL) and dimyristoyl phosphatidilcholine (DMPC), by the techniques of neutron scattering and electron microscopy. In order to simplify the experiment, we changed contrast by using deuterated (d-DMPC) and hydrogenated (h-DMPC) lipids to form recombinants, and did all of the scattering experiments in D_2O.

Negative stain electron microscopy of the 40:1 (M:M) recombinants showed discoid structures. The h-DMPC:A-I recombinants measured 99 ± 9 Å (standard deviation, n = 150) in diameter and 32 ± 3 Å (n = 50) in thickness; the d-DMPC:A-I recombinants measured 98 ± 10 Å (n = 150) by 33 ± 5 Å (n = 50).

In the first neutron scattering experiments, h-DMPC:A-I recombinants were studied at concentrations of 5.75, 11.5, and 23 mg dry weight lipid per ml. Calculation of the radii of gyration showed no concentration dependence, within experimental error.

Figure 1 shows Guinier plots of low-angle scattering from h-DMPC and d-DMPC recombinants. Radii of gyration calculated from the slopes were 33.5 ± 0.2 Å for h-DMPC and 38.0 ± 0.5 Å for d-DMPC. The normalized square roots of zero-angle intensity were 3.8 and 1.0, respectively. The electron microscopic studies indicate that this difference in radii of gyration cannot be explained simply by different diameters of the h- and d-particles.

Data obtained from the Guinier region cannot determine uniquely the structure of particles. However, their consistency with other data may be examined using models based on geometric parameters and the scattering densities of the components. A-I:DMPC discs may be described in terms of three parts, with the scattering density of each assumed homogeneous. The lipids have no readily exchangeable hydrogens, and the average scattering densities calculated for their non-polar parts are -0.008×10^{-14} cm/Å^3 (h-DMPC) and 7.3×10^{-14} cm/A^3 (d-DMPC). The scattering density of the polar head group is 0.76×10^{-14} cm/Å^3 in each case.

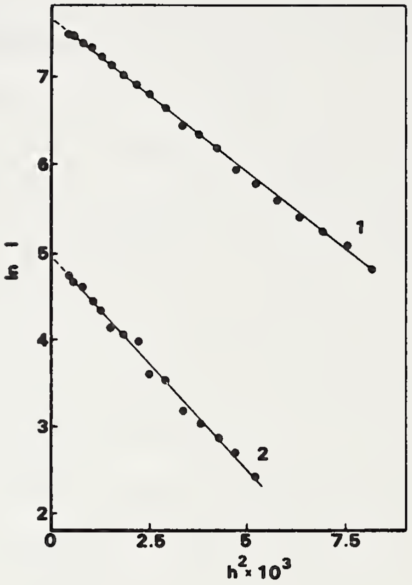

Figure 1. Guinier plots for apo A-I recombinants containing h-DMPC (curve 1) and d-DMPC (curve 2). Intensity is measured in arbitrary units, but is scaled for the two samples. h = 4π sinΘ/λ. Concentrations of recombinant were 24 (curve 1) and 30 mg/ml (curve 2).

The scattering density for a protein is more difficult to calculate because of uncertainties in hydration and hydrogen exchange. We arrived at the value to be used here by considering the scattering intensity at zero angle. The square root of intensity is proportional only to the sum of scattering lengths of all atoms in the complex, less the sum for displaced solvent molecules; it is not influenced by the distribution of atoms. If the level of hydration of protein is 0.4 g/g, it follows that the volume fraction of protein in the complex is 0.5, that of nonpolar part of the lipid is 0.375, and that of the polar lipid is 0.125. With these values, the scattering density of A-I can be calculated from the zero angle intensity as 5×10^{-14} cm/A^3. This corresponds to exchange of 30% of hydrogen atoms for deuterium, in good agreement with a figure of 25% obtained from the amino acid composition.

The larger radius of gyration for d-DMPC (in which the scattering density of the non-polar lipid closely resembles that of D_2O) clearly indicates that the protein resides in the outer part of the complex. Using the above values for the volume fractions and scattering densities of the components, we searched for model structures in best agreement with the experimental radii of gyration. We considered models based on spherical, spheroidal, and cylindrical geometries with either three separate scattering regions or protein uniformly dispersed throughout the lipid polar head regions. Predicted dimensions for the deuterated and hydrogenous recombinants were in best agreement for a three-component cylindrical model (figure 2) with $R = 49$ Å and $H = 16.3$ Å ($R_1 = 34.6$ A, $H_1 = 10.9$ Å). Good agreement was not obtained with spherical or mixed protein-lipid models. The best spheroidal model had dimensions similar to those of the optimal cylindrical one, but the fit was not as good. Thus the AI:DMPC recombinant can be approximated by a disc with diameter of 98 Å and height of 33 Å, in excellent agreement with the dimensions determined by negative stain electron microscopy. In this model the A-I protein forms an outer rim 15 Å

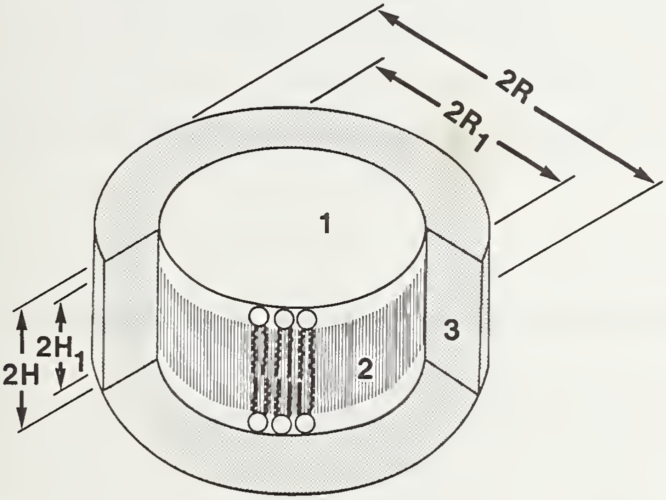

Figure 2. A model for apo A-I: DMPC discoid recombinants. Region 1 is occupied by DMPC polar head groups, region 2 by DMPC fatty acyl chains, and region 3 by apo A-I. Detailed discussion in text.

thick, the polar DMPC head groups are on the top and bottom and the non-polar fatty acid chains are buried inside.

High resolution negative stain electron microscopy shows two additional features compatible with the bicycle tire model. First, when the discoid particles orient with their flat faces parallel to the plane of the grid, contrast rims can be seen around the perimeters of the discs. Second, examination of discs oriented edgewise (the usual manner of orientation) reveals two parallel electron-lucencies running the length of the disc rim. These parallel lucencies are each approximately 16 Å thick. As evidence against artifact, both features are seen independently of the grain size or level of focus of the micrographs; however, artifact cannot be ruled out absolutely.

The electron microscopic features and neutron scattering data are compatible with a molecular model consisting of a unilamellar lipid bilayer disc 68 Å in diameter (at the 40:1 DMPC:A-I ratio), whose rim is lined with A-I. The dimensions of the protein rim ($R-R_1$ = 15 Å; 2H = 33 Å) indicate two A-I molecules per recombinant consistent with cross-linking studies reported earlier.

A STUDY OF METHYL GROUP LIBRATION IN NITROMETHANE

S. F. Trevino
(Energetic Materials Division, LCWSL, ARRADCOM, Dover, NJ)

and

E. Prince

and

C. R. Hubbard
(Ceramics, Glass, and Solid State
Science Division)

Nitromethane, CH_3NO_2 freezes at -30°C, forming an orthorhombic structure in space group $P2_12_12_1$ with Z=4. Neutron powder diffraction patterns were obtained from a deuterated sample at six temperatures from 4.2K to 125K. Quasielastic neutron scattering showed that the methyl groups undergo hindered rotation with a potential barrier corresponding to a temperature of 118K. A librational motion would be expected with substantial amplitude even at the lowest temperature. The structure was refined by profile analysis using a constrained model in which the methyl group was allowed to librate around the C-N vector, and also was required to have three-fold symmetry around that vector. At the lowest temperature the libration has a zero point amplitude consistent with the energy levels inferred from neutron spectroscopy. As the temperature is raised, the amplitude increases monotonically in good agreement with theoretical expectations. Even at 125K the hydrogen equilibrium positions are well defined, although the standard deviations are higher at the higher temperatures.

AN OBSERVATION OF ONE-DIMENSIONAL REORIENTATION AND TUNNEL SPLITTING OF THE GROUND AND FIRST EXCITED STATE IN A LOW BARRIER SYSTEM: SOLID NITROMETHANE

S. F. Trevino
(Energetic Materials Division, LCWSL, ARRADCOM, Dover, NJ)
and
(National Bureau of Standards
Washington, DC)

In this communication, we report the complete characterization of the structural and dynamical properties of a simple one dimensional rotor with the lowest known barrier to rotation in the solid state.

The molecule of nitromethane (CH_3NO_2) has, in the gas phase, one of the lowest known barriers (6 cal/mole) to reorientation of the methyl group about the C-N bond.[1] The barrier to reorientation in the solid will, therefore, be dominated by the crystalline forces. Quantum mechanical effects exhibited as tunnel splitting of the torsional levels are extremely sensitive to the barrier height, decreasing rapidly as the barrier height increases. A model compound in which the barrier is low would thus be very desirable for the study of such phenomena.

The crystal structure of nitromethane has been determined[2] to be orthorhombic with space group $P2_12_12_1$ and containing one molecule in the asymmetric unit. The positions of the carbon, nitrogen and oxygen atoms were determined by a single crystal X-ray diffraction measurement and the position and anisotropic temperature factors of the deuterons by a neutron powder diffraction study of CD_3NO_2. The three deuterons are related by three-fold symmetry about the C-N bond and the major axis of their thermal ellipsoid corresponds to rotation about the three-fold axis.

Quasielastic neutron scattering has been used to investigate the reorientation of the methyl group at temperatures comparable to the barrier height. Under these conditions it has been shown[3] that the methyl group motion can be very well described by a jump reorientation model in which it reorients between equilibrium positions after a mean residence time τ. The structure of the solid suggests that the reorientations occur by 120° jumps about the C-N bond. This model predicts the following incoherent neutron scattering function from a polycrystalline sample:[4]

$$S(Q,\omega) = \exp\ (-Q^2u^2) \left\{ \frac{1}{3} \left[1 + \frac{2\sin(Qd)}{Qd} \right] \delta(\omega) + \frac{2}{3\pi} \left[1 - \frac{\sin(Qd)}{Qd} \right] \frac{3/2\tau}{(3/2\tau)^2 + \omega^2} \right\}$$

where d is the jump distance, u^2 is the mean squared amplitude of vibration of the H atoms; Q is the momentum transfer, and ω is the frequency transfer in the scattering. A triple axis spectrometer was used in the quasielastic and inelastic scattering measurements. In figure 1 is presented one measurement of the quasielastic scattering at 78 K and a Q of 2.88 $\mathring{A}^{-1}$. The fit is obtained with a τ of 2.15×10^{-12} sec. The Q dependence of the relative contributions of delta function and Lorentzian over a Q range of 1 to 4 $\mathring{A}^{-1}$ are correctly predicted. The temperature dependence of τ from 50K to 150K is well described by an Arrhenius relation with an activation energy of 230 cal/mole. The tunnel splitting of the ground state of a one-dimensional three-fold rotor with such a low barrier is expected to be a large fraction of 100 μeV.[5] An attempt was made to measure the transition between the tunnel split ground state with a resolution of 55 μeV. Figure 2 presents the results of this measurement at a temperature of 4.2K. The upper figure presents the data and the instrumental resolution. There is clear evidence of broadening. This additional scattering cannot be attributed to quasielastic scattering due to thermally activated reorientation, since the broadening would be much smaller than the instrumental resolution. The lower figure presents a fit of the data with three gaussians, one centered at zero energy transfer and two side bands centered at ±45 μeV energy transfer. We believe these result from transitions between the tunnel split ground state. This conclusion will be confirmed when a higher resolution instrument becomes available in the near future. A three-fold cosine potential[5] which predicts a ground state tunnel splitting of 45 μeV produces one bound tunnel

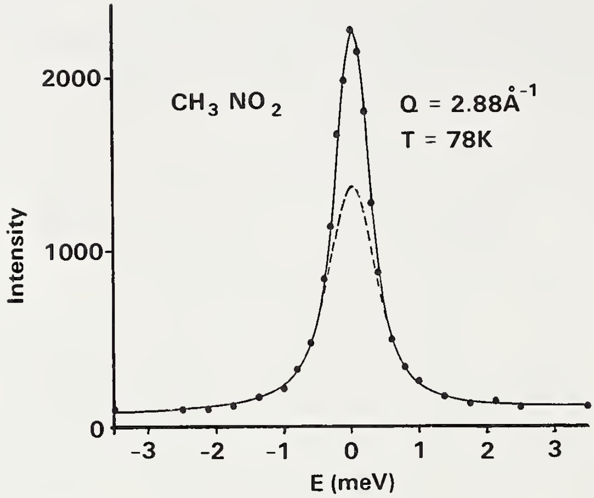

Figure 1. The measured and calculated quasielastic neutron scattering spectrum for solid nitromethane at 78K and Q = 2.88 Å^{1}. The resolution of the instrument is .44 meV. The solid line is a fit obtained to the data as described in the test and the dashed line is the Lorentzian contribution.

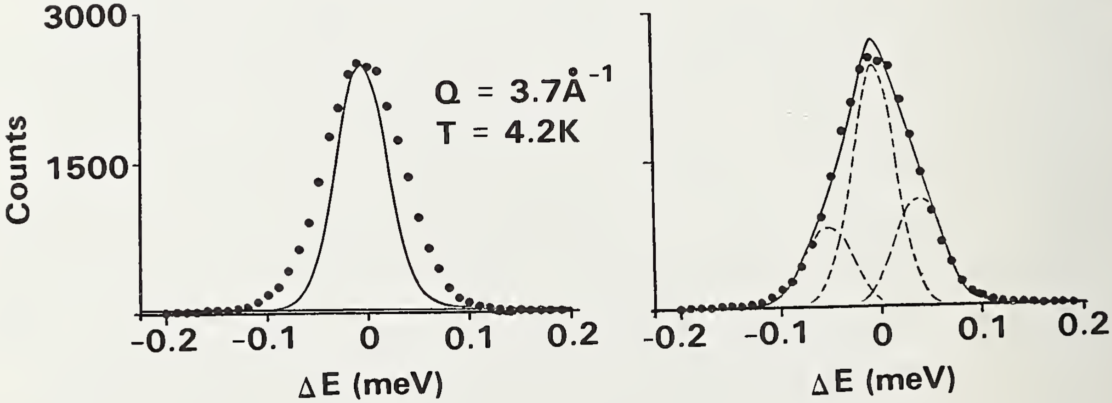

Figure 2. In elastic scattering spectrum of CH_3NO_2 at 4.2K and Q = 3.7 Å^{1}. The upper figure presents the data and the measured gaussian resolution of 55 μeV. The lower figure presents the fit to the data obtained with three gaussians (dashed curves) as discussed in the text.

split (by .75 meV) excited state whose splitting substantially narrows and whose average energy shifts down by a factor of 1.38 upon deuteration. Features in an inelastic spectrum due to librations are expected to be the most intense, for these produce the largest amplitude motions. Figure 3 presents inelastic scattering data on both CH_3NO_2 and CD_3NO_2 (at 4.2K). The libration spectrum of the hydrogenous sample can be fit by two very broad gaussian peaks whose average energy is 7.4 meV and which are split by .8 meV; the spectrum of the deuterated sample shows a narrow peak at 5.3 meV. The broadening of the peaks observed in the CH_3NO_2 reflects life time effects due to the fact that the levels are very close to the top of the potential well.

We have thus observed a solid state system exhibit behavior, as a function of temperature, from the quantum mechanical to the classical thermally activated regimes.

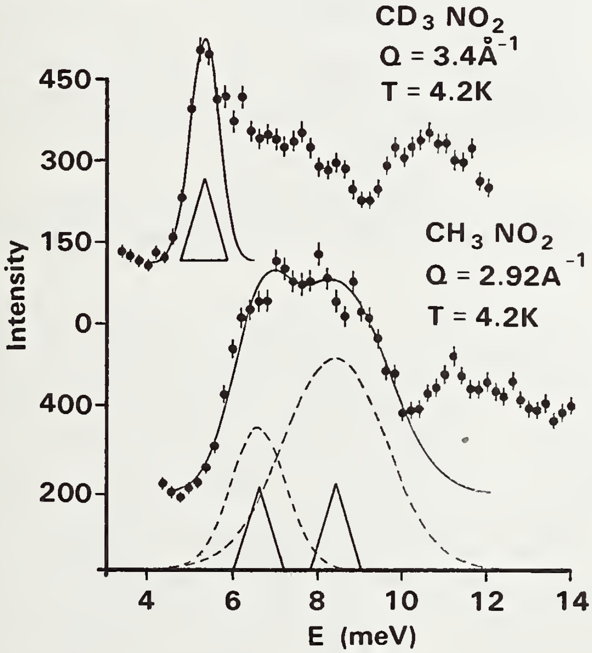

Figure 3. The inelastic scattering spectra of CD_3NO_2 (upper figure) and CH_3NO_2 (lower figure) obtained at 4.2K. The triangles correspond to the instrumental resolution. The solid lines correspond to the overall fit and the dashed lines in the lower figure to the individual components.

---

1. E. Tannenbaum, R. J. Myers and W. D. Gevinn, *J. Chem. Phys.* 25, 42 (1965).
2. S. F. Trevino, C. Hubbard and E. Prince, *J. Chem. Phys.* (to be published).
3. C. T. Chudley and R. J. Elliot, *Proc. Phys. Soc. London* 77, 353 (1961) K. Skold, *J. Chem. Phys.* 49, 2443 (1968).
4. C. Steenbergen and J. J. Rush, *J. Chem. Phys.* 70, 50 (1979).
5. James E. Wollrah, Rotational Spectra and Molecular Structure, Ernest M. Loebl Ed. *(Academic Press, New York, 1967)* Appendix 12.

NEUTRON POWDER DIFFRACTION STUDY OF THE STRUCTURES OF $CeTaO_4$, $CeNaO_4$, AND $NdTaO_4$

A. Santoro

M. Marezio
(Laboratoire de Cristallographie, C.N.R.S., Grenoble-Cedex, France)

and

R. S. Roth and D. Minor
(Ceramics, Glass and Solid State Science Division)

1. Experimental

The compounds were prepared by mixing the appropriate amounts of tantalum, niobium, cerium and neodimium oxides and by heating the mixtures overnight at 1000°C in platinum crucibles. After cooling to room temperature, the products of this heat treatment were ground, heated again at 1400°C for $CeNbO_4$, 1500°C for $CeTaO_4$ and 1600°C for $NdTaO_4$, over a period of 16-20 h, quenched in water, filtered and dried. The only single crystals obtained for these materials were too small for neutron diffraction and many of them were twinned, especially in the case of $CeTaO_4$. It was therefore decided to analyze the materials with the powder technique and to refine the structures with the Rietveld method[6].

Neutron diffraction measurements were made at room temperature on a powder diffractometer at the National Bureau of Standards Reactor, using the experimental conditions shown in table 1. The structural refinements were based on space group $P2_1/c$ for $CeTaO_4$ and I2/a* for $CeNbO_4$ and $NdTaO_4$. The contribution to the profile from the background was determined at portions of the powder patterns free from diffraction effects, and estimated by extrapolation from these regions to those where overlapping is most severe. The neutron scattering amplitudes used were b(Ta) = 0.70, b(Ce) = 0.48, b(Nb) = 0.71, b(Nd) = 0.72 and b(O) = 0.58×10^{-12} cm [7]. The initial values of the structural parameters were those obtained in the x-ray study of $LaTaO_4$ [5] for $CeTaO_4$ and those obtained in the x-ray study of $YNbO_4$ [8] for $CeNbO_4$ and $NdTaO_4$. In all cases individual isotropic temperature factors were used in the calculations and were allowed to vary. The starting lattice constants were determined with the x-ray powder method and the initial values of the profile parameters U, V and W were calculated theoretically[9]. A total of 33 and 21 structural, lattice and profile parameters were refined simultaneously for $CeTaO_4$ and for $CeNbO_4$ and $NdTaO_4$, respectively, until all shifts were less than 0.3σ.

From the early stages of the analysis it was apparent that the isotropic temperature factor of the Nd atom in the structure of $NdTaO_4$ was converging to an incorrect value [$B(Nd) = -0.19$ Å^2]. Such abnormal behavior of the thermal parameter may be caused by the use of an improper neutron scattering amplitude for the Nd atom; and, in fact, a check of the literature revealed that the value b(Nd) = 0.72×10^{-12} cm used in the calculations was too low. More reasonable results and lower R factors were obtained by using an updated amplitude of 0.77×10^{-12} cm [10], but B(Nd) still converged to a value abnormally low (0.13 Å^2). At this point b(Nd) was allowed to vary and after final refinement the value

---

*The standard setting for space group I2/a is C2/c. The transformation matrix from our axes to the conventional ones is $(00\bar{1}/010/101)$.

$b(Nd) = 0.80 \times 10^{-12}$ cm was obtained with reasonable thermal parameters for all atoms in the structure. The results of these calculations are summarized in table 2. (It is worth noting that the atomic positional parameters obtained in the three refinements of the structure did not vary by more than two times the standard deviation.)

Refinements of the structures of $CeNbO_4$ and $NdTaO_4$ in the acentric space group Ia did not differ significantly from those in I2/a and therefore the centric space group was assumed for these compounds.

2. Results

a. Profile parameters.

The profile parameters obtained in the refinements are shown in table 3 where they are compared with those calculated theoretically. The experimental values agree closely with one another and with those of other compounds studied with the same experimental conditions, but they are significantly higher than the theoretical values. Discrepancies of this kind have been noted previously[9,11] and are probably caused by approximations made in deriving the original theory rather than by crystallite size effects or structural distortions.

b. Lattice parameters.

The lattice constants obtained in the neutron study agree well with those determined with the x-ray powder method. The former, however, are systematically smaller than the latter, as shown in table 4. This effect is probably the result of slightly underestimating the neutron wavelength. The x-ray parameters, therefore, should be preferred over those obtained in the neutron refinement.

c. Structure of $CeTaO_4$.

The results of the structure refinement of $CeTaO_4$ are shown in table 5. A projection of the unit cell on the (010) plane is shown in figure 1 and cation-oxygen distances are given in table 6. In the asymmetric unit there is one type of tantalum and one type of cerium cations, whereas there are four types of oxygen anions. The tantalum cations are located at the center of the oxygen octahedra which are outlined in figure 1. Each octahedron is formed by two oxygen atoms of type O(1), two of type O(2), one of type O(3), and one of type O(4). The average Ta-O distance is 1.990 Å. The octahedra share only vertices among themselves; they form blocks which are infinite in two dimensions (along the b and c axes) and are two octahedra wide in the third (the a^* axis). These are actually perovskite-like blocks and the cerium atoms are located in sites similar to the A sites of the ABO_3 perovskite structure. The cerium cations are surrounded by eleven oxygen anions, belonging to the same block [three O(1), four O(2), two O(3), and two O(4)], because of the finite dimension of the blocks. The twelfth is replaced by two oxygen anions of the adjacent block. These two come closer to the cerium cation because each block is displaced with respect to the adjacent one by half the height of an octahedron. The blocks are linked together by these interblock Ce-O bonds. In order to form these bonds, the cerium cations move out of the center of the eleven-oxygen polyhedra so that they become so distorted that only six oxygen anions are first nearest neighbors to the cerium cation. The Ce-O distances corresponding to the interblock bonds (2.361 and 2.826 Å) are of the same order of magnitude as those of the intrablock Ce-O bonds. Each cerium cation is bonded to one O(1), one O(2), three O(3) and three O(4) oxygen atoms. The coordination number of the cerium cations is thus eight and the average Ce-O distance is 2.520 Å. The coordination number of the oxygen anions is 3 for O(1) and O(2) and 4 for O(3) and O(4). The first two are bonded to two Ta and one Ce cations whereas the other two are bonded to one Ta and three Ce cations. If one calculates the charge of these four oxygen anions without taking into account the differences in the anion-cation distances [anionic charge = $\sum_i S_i$, where S_i, the bond strength, is the ratio $\frac{Z}{n}$, Z is the cationic charge and n the cationic coordination number], one finds for O(1) and O(2), $\sum_i S_i = 2.04$ and for O(3) and O(4), $\sum_i S_i = 1.96$. These values indicate that only a small part of the distortion is needed to balance the electrostatic charge.

It has been pointed out recently[1,2] that $CeTaO_4$ can absorb oxygen according to the following oxidation-reduction reaction:

$$CeTaO_4 + 1/2O_2 \rightarrow Ce^{3+}_{1-2x}\ Ce^{4+}_{2x}\ TaO_{4+x}$$

The x parameter is variable and temperature dependent. Three distinct ranges in x ($x \simeq 0.49$, $x \simeq 0.37$, $x \simeq 0.12$) were found to yield three different phases.

The structural arrangement of $CeTaO_4$ can also be regarded as that of an oxidized ABO_3 perovskite. An extra oxygen layer is inserted in the structure every three anion layers and this causes the separation of the perovskite blocks into finite two-octahedron thick slabs. For instance, it can be seen from figure 1 that if the oxygen anions O(3) at $y = 1.02$ were coincident with O(4) at $y = 0.99$, and if O(4) at $y = 0.49$ were coincident with O(3) at $y = 0.52$, the structural arrangement would be truly an ABO_3 perovskite-like arrangement. When these oxygen anions are not coincident, the ABO_4 compound is obtained instead.

d. Structures of $CeNbO_4$ and $NdTaO_4$.

The results of the profile refinements of $CeNbO_4$ and $NdTaO_4$ are given in tables 7 and 8 and relevant cation-oxygen distances in tables 9 and 10. The two compounds are isostructural and, therefore, many of the considerations made for $CeNbO_4$ can be applied, *mutatis mutandis*, also to $NdTaO_4$. Figure 2 shows the cerium and niobium polyhedra arrangement in $CeNbO_4$ as viewed down the monoclinic $\underline{b}$ axis. This structure is a monoclinic distortion of the tetragonal structure of scheelite, $CaWO_4$.

There are one cerium, one niobium, and two oxygen ions in the asymmetric unit. The cations have a distorted face-centered cubic arrangement. The cerium cations are surrounded by eight oxygen ions, four O(1) and four O(2), forming two interpenetrated tetrahedra. The average Ce-O distance is 2.480 Å. The niobium cations are surrounded by four close oxygen ions, two O(1) and two O(2), arranged as a distorted tetrahedron. The average Nb-O distance over these four neighbors is 1.886 Å. There are four other oxygen ions around the niobium cations, each one capping a face of the closest tetrahedron. Two of these oxygen ions are close enough (the corresponding Nb-O distance being 2.482 Å) that they may be considered bonded to the niobium atoms, whereas the other two are removed much farther and cannot be considered as involved in the bonds. In the scheelite $CaWO_4$ structure, the eight oxygen ions surrounding the tungsten cation are arranged as two interpenetrated tetrahedra of very different sizes. The two sets of W-O distances are 1.78 Å and 2.91 Å (13). The calcium cations are also surrounded by eight oxygen ions but differ from the tungsten cations because the two sets of cation-oxygen distances in the calcium case are very close, 2.44 and 2.48 Å. One possible way of looking at the scheelite structure is to consider it as a distorted superstructure of fluorite, CaF_2. The fluorite structure contains a simple cubic array of anions so that all cations which form a perfect face-centered cubic lattice have an eightfold coordination. In the scheelite structure, instead, the cations are distorted slightly from the f.c.c. lattice and the anions move away from the simple cubic positions in the following manner: four of the eight anions around the positions occupied by the small cations move closer to these cations and in this way a tetrahedral coordination is achieved for the small cations. The remaining four anions move farther away from these cations in such a way that the large cations still have an eightfold coordination. The resulting polyhedron around the large cations has mm symmetry, i.e., lower than the m3m symmetry of the cubic structure. From this point of view the fergusonite-like structures could be considered as intermediate between the fluorite and the scheelite structures, even though the fluorite is cubic, the scheelite is tetragonal and the fergusonite-like structures have either orthorhombic or monoclinic symmetry. In this latter type of structure, two anions of the four forming the larger tetrahedron around the small pentavalent cations, come closer to Nb^{+5} cations in $CeNbO_4$ and to the Ta^{+5} cations in $NdTaO_4$. It should also be pointed out that in the scheelite structure the cubic arrangement of the anions is so distorted that it is better described as a puckered hexagonal network.

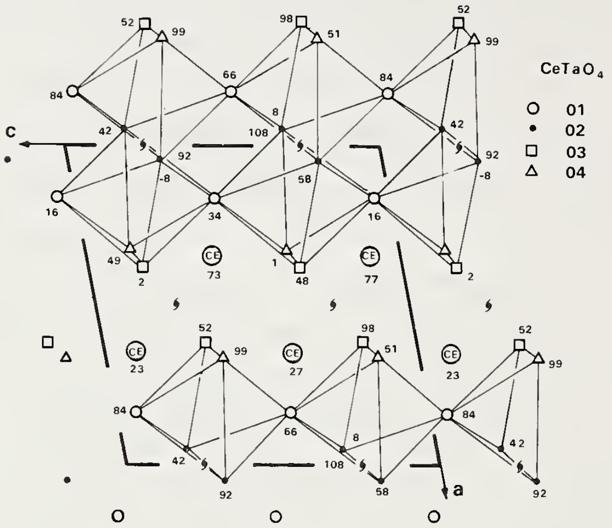

Figure 1. Projection on (010) of the structure of $CeTaO_4$. The Ta cation are located at the centers of the distorted octahedra outlined in figure. The y-coordinate (x100) is given for each atom.

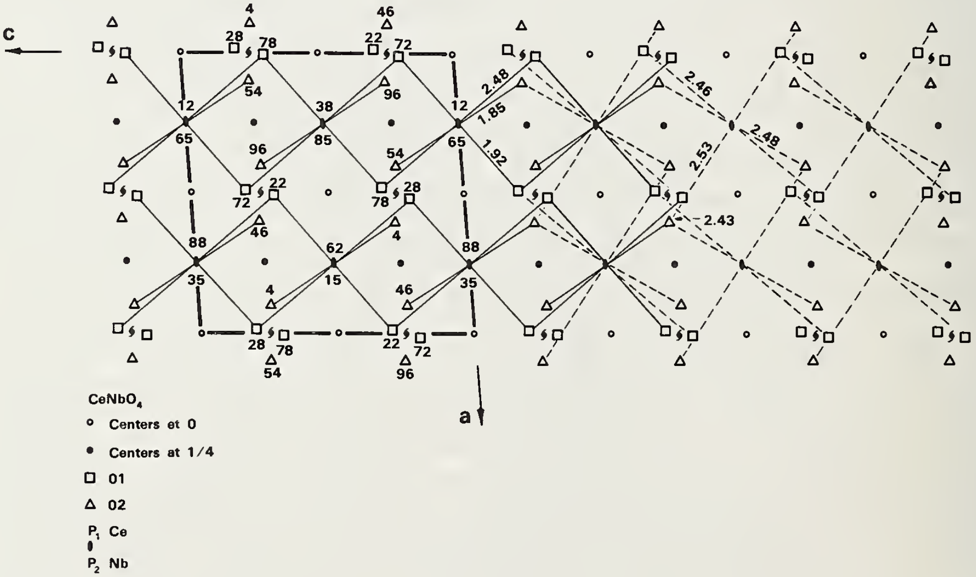

Figure 2. Projection on (010) of the structure of $CeNbO_4$. The solid lines identify the Nb polyhedron, the broken lines, the Ce polyhedron. The y-coordinate (x100) is indicated for each atom. The relevant Ce-O and Nb-O distances are also given.

In the structure of $CeNbO_4$ the oxygen atom O(1) is surrounded by two niobium and two cerium atoms and the O(2) atom is surrounded by one niobium and two cerium atoms. Consequently, if one does not take into account the individual distances, the former anion is overbonded ($\sum S_i = 2.42$), whereas the latter one is underbonded ($\sum S_i = 1.58$). Therefore, in this structure the differences in these distances are mainly due to balancing the electrostatic charge.

As we have mentioned earlier $NdTaO_4$ and $CeNbO_4$ are isostructural. A difference which is worthwhile to point out lies in the coordination of the pentavalent cations. As can be seen from table 9 and 10 the first two sets of M^{5+}-O distances increase (from 1.851 and 1.920 to 1.861 and 1.941 Å), whereas the third set decreases (from 2.482 to 2.353 Å) on going from the niobate to the tantalate. These values indicate that this third set of oxygen atoms behave, at least in the niobate, as second nearest neighbors. Therefore the coordination number of these cations should be taken as 4+2, although the Ta^{+5} ion appears to be approaching six-fold coordination.

The change in structure which takes place in the tantalum series is probably due to the size of the rare-earth cation. When this size becomes too large for the A-site of the fergusonite-like structure, the tantalates crystallize with the $LaTaO_4$-type structure. The same structural change does not take place in the niobates because of the preference of the Nb^{5+} cations for a coordination smaller than six.

Table 1. Experimental conditons used to collect the powder intensity data for $CeTaO_4$, $CeNbO_4$, and $NdTaO_4$.

Monochromatic beam: reflection 220 of a Cu monochromator in transmission geometry.

Mean neutron wavelength: 1.5416(3) Å

Horizontal divergences
- (i) In-pile collimator: 10 min. arc;
- (ii) Monochromatic beam collimator: 20 min. arc;
- (iii) Diffracted beam collimator: 10 min. arc.

Monochromator mosaic spread: 15 min. arc.

Sample container: V can of 1 cm. diameter.

Table 2. Coherent neutron scattering amplitude of Nd.

b(Nd)	0.72(*)	0.77(**)	0.80(***)
B(Nd)	−0.19(4) A^2	0.13(4)	0.31(4)
B(Ta)	0.70(5)	0.57(5)	0.50(5)
B(01)	0.67(4)	0.52(4)	0.43(4)
B(02)	0.71(4)	0.58(4)	0.51(4)
$R^{(x)}$	5.41	5.23	5.24
R_p	9.76	9.41	9.42
R_w	11.07	10.73	10.70
R_e	7.08	7.06	7.06
χ	1.57	1.52	1.52

(*) Bacon, G.E. (1972). *Acta Cryst.*, A28, 357.

(**) Yelon, W.B. (1977). Neutron Diffraction Newsletter.

(***) From refinement of $NdTaO_4$.

(x) $$R = 100 \times \left\{ \frac{\sum |I(obs) - I(cal)|}{\sum I(obs)} \right\}$$

$$R_p = 100 \times \left\{ \frac{\sum |y(obs) - y(cal)|}{\sum y(obs)} \right\}$$

$$R_w = 100 \times \left\{ \frac{\sum w[y(obs) - y(cal)]^2}{\sum w[y(obs)]^2} \right\}^{1/2}$$

$$R_e = 100 \times \left\{ \frac{N - P + C}{\sum w[y(obs)]^2} \right\}^{1/2}$$

In the above formulas N is the number of statistically independent observations, P the number of parameters refined, C the number of constraints, I the integrated intensities and w the weights.

Table 3. Profile parameters

	U	V	W deg.^{2}
Calculated	0.212	-0.231	0.107
$CeTaO_4$	0.43 (2)	-0.47 (2)	0.221(6)
$CeNbO_4$	0.418(8)	-0.47 (1)	0.219(3)
$NdTaO_4$	0.39 (1)	-0.45 (2)	0.221(5)

The parameters U, V and W appear in the equation

$$H^2 = U \tan^2\theta + V \tan\theta + W$$

where H is the full width at half maximum of a reflection occurring at the Bragg angle θ. The theoretical values of U, V and W have been calculated with the expressions derived by Caglioti, Paoletti and Ricci, *Nucl. Instr*., 3, 223-228(1958).

Table 4. Lattice parameters

	$CeTaO_4$	$NdTaO_4$	$CeNbO_4$
a			
Neutrons	7.6161(3)	5.5115(2)	5.5350(1)
X-rays	7.618 (1)	5.520 (1)	5.542 (1)
b			
Neutrons	5.5254(2)	11.2320(3)	11.3991(3)
X-rays	5.531 (1)	11.244 (2)	11.414 (1)
c			
Neutrons	7.7588(3)	5.1112(1)	5.1590(1)
X-rays	7.767 (1)	5.117 (1)	5.165 (1)
β			
Neutrons	100.87 (2)	95.71 (1)	94.60 (1)
X-rays	100.94 (2)	95.72 (1)	94.60 (1)

The errors on the cell dimensions determined by neutron diffraction do not include the error in the neutron wavelength.

Table 5. Results of the total profile refinement of the structure of $CeTaO_4$. Space group $P2_1/c$(*)

Atom	Position	X	Y	Z	B
Ce	4el	0.3441(6)	0.7728(7)	0.0999(5)	0.73(8)
Ta	"	0.1668(4)	0.2670(6)	0.3045(4)	0.65(6)
0(1)	"	0.1680(5)	0.1604(6)	0.0544(5)	0.69(8)
0(2)	"	0.0568(5)	0.5869(5)	0.2067(5)	0.90(8)
0(3)	"	0.3823(4)	0.4842(6)	0.3312(5)	0.52(7)
0(4)	"	0.3338(4)	0.0084(6)	0.3671(4)	0.78(6)

$R = 3.82$, $R_p = 8.29$, $R_w = 10.04$; $R_e = 8.08$.

Number of points above background: 1277.

2Θ(initial) = 11.0°, 2Θ(final) = 94°, step = 0.05°.

Number of independent Bragg reflections: 290.

Parameters refined

(i) Structural (including scale factor) = 25

(ii) Lattice (including zero point for 2Θ) = 5

(iii) Profile = 3

(*) Figures in parentheses are standards deviations in the last decimal figure.

Table 6. Cation-oxygen distances (Å) in $CeTaO_4$.

Tantalum-octahedron

Ta - O(1)	2.032(5)
O(1)	1.980(5)
O(2)	2.041(4)
O(2)	1.960(5)
O(3)	2.013(4)
O(4)	1.914(5)

Average = 1.990

Cerium-polyhedron

Ce - O(1)	2.518(5)
O(2)	2.688(6)
O(3)	2.380(5)
O(3)	2.361(5)*
O(3)	2.545(6)
O(4)	2.464(5)
O(4)	2.826(6)*
O(4)	2.375(5)

Average = 2.520

* These are interblocks Ce - O distances.

Table 7. Results of the total profile refinement of the structure of $CeNbO_4$. Space group I2/a

Atom	Position	X	Y	Z	B
Ce	4e2	1/4	0.1202(2)	0	0.41(5)
Nb	4e2	1/4	0.6470(1)	0	0.40(4)
0(1)	8f1	0.0129(3)	0.7171(1)	0.2031(3)	0.68(3)
0(2)	8f1	0.8999(3)	0.4553(1)	0.2399(3)	0.60(3)

$R = 3.32$, $R_p = 7.33$, $R_w = 8.94$, $R_e = 6.34$.

Number of points above background: 1520

2Θ(initial) = 14.5°, 2Θ(final) = 111.7°, step = 0.05°.

Number of independent Bragg reflections: 212.

Parameters refined

(i) Structural (including scale factor) = 13

(ii) Lattice (including zero point for 2Θ) = 5

(iii) Profile = 3

Table 8. Results of the total profile refinement of the structure of $NdTaO_4$. Space group I2/a

Atom	Position	X	Y	Z	B
Nd	4e2	1/4	0.1178(2)	0	0.31(4)
Ta	4e2	1/4	0.6515(2)	0	0.50(5)
0(1)	8f1	0.0152(4)	0.7188(2)	0.2165(5)	0.43(4)
0(2)	8f1	0.9014(4)	0.4563(2)	0.2396(4)	0.51(4)

$R = 5.24$, $R_p = 9.42$, $R_w = 10.70$, $R_e = 7.06$.

Number of points above background: 1516.

2Θ(initial) = 15.0°, 2Θ(final) = 114.5°, step = 0.05°.

Number of independent Bragg reflections: 220.

Parameters refined:

(i) Structural (including scale factor) = 13

(ii) Lattice (including zero point for 2Θ) = 5

(iii) Profile = 3

Table 9. Cation-oxygen distances (Å) in $CeNbO_4$.

Cerium polyhedron

Ce - O(1) x2	2.461(2)
O(1) x2	2.535(2)
O(2) x2	2.428(2)
O(2) x2	2.494(2)

Average = 2.480

Niobium polyhedron

Nb - O(1) x2	1.920(2)
O(2) x2	1.851(2)
O(1) x2	2.482(2)

Average = 2.084

Table 10. Cation-oxygen distances (Å) in $NdTaO_4$.

Neodimium polyhedron

Nd - O(1) x2	2.441(3)
O(1) x2	2.534(3)
O(2) x2	2.380(2)
O(2) x2	2.449(3)

Average = 2.451

Tantalum polyhedron

Ta - O(1) x2	1.941(2)
O(2) x2	1.861(3)
O(1) x2	2.353(3)

Average = 2.052

1. T. Negas, R. S. Roth, C. L. McDaniel, H. S. Parker and C. D. Olson, *Mat. Res. Bull.*, 12, 1161 (1977).
2. R. S. Roth, T. Negas, H. S. Parker, D. B. Minor and C. Jones, *Mat. Res. Bull.*, 12, 1173 (1977).
3. R. S. Roth, T. Negas, H. S. Parker, D. B. Minor, C. D. Olson and C. Skarda, *The Rare Earths in Modern Science and Technology*, edited by G. J. McCarthy and J. J. Rhyne, 163 (1978).
4. R. J. Cava, T. Negas, R. S. Roth, H. S. Parker, D. B. Minor and C. D. Olson, *The Rare Earths in Modern Science and Technology*, edited by G. J. McCarthy and J. J. Rhyne, 181 (1978).
5. T. A. Kirova and V. B. Alexandrov, *Doklady Akademii Nauk*, USSR, 201, 1095 (1971).
6. H. M. Rietveld, *J. Appl. Cryst.*, 2, 65 (1969).
7. G. E. Bacon, *Acta Cryst.*, A28, 357 (1972).
8. C. T. Prewitt, Private communication.
9. G. Caglioti, A. Paoletti and F. P. Ricci, *Nucl. Instrum.*, 3, 223 (1958).
10. W. B. Yellon, Neutron Diffraction Newsletter (1977).
11. G. Caglioti and F. P. Ricci, *Nucl. Instrum. Methods*, 15, 155 (1962).
12. A. Santoro, R. S. Roth and D. B. Minor, *Acta Cryst.*, B33, 3945 (1977).
13. A. Zalkin and D. H. Templeton, *J. Chem. Phys.*, 40, 501 (1964).

DETERMINATION OF THE RELATIONSHIP BETWEEN DERIVATIVE LATTICES

A. Santoro

and

A. D. Mighell
(Ceramics, Glass, and Solid State Science Division)

and

J. R. Rodgers
(University Chemical Laboratory, Cambridge, U.K.)

In the study of crystalline materials it is often necessary to find the relationship between two or more crystal lattices, either identical or different from one another. Typical cases in which a knowledge of lattice relationships are required occur, for example, in the critical evaluation of data to be included in major compilations as the Crystal and Powder Data Files, in the analysis of twinning and coincidence-site lattices, in the study of interrelated structures, in the evaluation of the results obtained from powder indexing procedures, in single-crystal diffractometry, and in many other areas of crystallography.

The method commonly employed to study how two lattices are related is based on converting an arbitrary cell into a standard one, such as the Delaunay Cell (Delaunay, 1933), the reduced cell (Santoro and Mighell, 1970), the Crystal Data Cell (Donnay and Ondik, 1972), or the conventional cell as defined in the International Tables (1969). This method is particularly suitable to classify crystalline materials, to establish symmetry, and to recognize if two cells describe the same lattice. It has, however, one serious disadvantage in that it does not allow one to determine easily if the two lattices are derivative of one another, i.e., if one is the super-, sub-, or composite lattice of the other. This is unfortunate because many of the crystallographic problems mentioned previously are related to the derivative character of lattices.

For example: (i) twinning by reticular merohedry takes place because a superlattice of the crystal lattice has elements of symmetry other and above those of the crystal lattice; (ii) the solutions obtained in the indexing of a powder pattern are commonly derivative lattices; (iii) cell determinations carried out with automated four-circle diffractometers, not infrequently, yield lattices which are derivative of the true lattice of the crystal. A second disadvantage in the use of conventional cells is that this method often requires a transformation of the cells determined experimentally. This is often a complicated process, and if the transformation is not applied properly, cells which in fact are not conventional may result, or, in some cases, one may even obtain a lattice different from the original.

These shortcomings can be circumvented by devising practical procedures to determine the matrices relating arbitrary cells of two or more lattices. The relevant properties of the lattices can then be derived from the nature of the transformation matrices. A method based on such an approach has been developed and is described in the following sections.

1. Theory

Let us consider two lattices Λ and Λ' of vector bases $\vec{a}_i$ and $\vec{a}'_i$ ($i = 1, 2, 3$). As the metric properties of a lattice are completely specified by any triplet of noncoplanar translations, $\vec{a}_i$ and $\vec{a}'_i$ can be chosen arbitrarily. For simplicity, however, we will assume that the unit cells defined by $\vec{a}_i$ and $\vec{a}'_i$ are primitive. We will also assume that Λ and Λ' have a common origin in a node, but otherwise, arbitrary mutual orientation. The two lattices are then related by the transformation

$$\vec{a}_i = \Sigma_j \, B_{ij} \, \vec{a}'_j \qquad (i,j = 1, 2, 3) \qquad (1)$$

The elements B_{ij} of matrix $\underset{\sim}{B}$ can be any real numbers.

Let us suppose, however, that they are all rational. In this case we have:

Theorem: "If two lattices Λ and Λ' are related by a transformation matrix $\underset{\sim}{B}$ having rational elements B_{ij}, the two lattices have a superlattice Γ in common, and the converse is also true."

If the B_{ij}'s are rational, we may write

$$B_{ij} = N_{ij}/n_{ij} = \nu_{ij}/\mu_i \tag{2}$$

where N, n, ν and μ are integers and μ_i is the minimum common multiple of n_{i1}, n_{i2}, and n_{i3}. Substituting in equation (1), we have

$$\vec{a}_i = \Sigma_j \frac{\nu_{ij}}{\mu_i} \vec{a}'_j$$

i.e.

$$\mu_i \vec{a}_i = \Sigma_j \nu_{ij} \vec{a}'_j = \vec{s}_i \tag{3}$$

Since μ_i and ν_{ij} are integral, the translations $\mu_i \vec{a}_i$ define a superlattice of Λ(*) and the translations $\nu_{ij} \vec{a}'_j$ and $\Sigma_j \nu_{ij} \vec{a}'_j$ superlattices of Λ'. It follows that the translations $\vec{s}_i$ define a lattice Γ which is a superlattice of both Λ and Λ'.

To prove the converse, let us suppose that Λ and Λ' have a common superlattice Γ defined by the translations $\vec{s}_i$. We may write

$$\vec{s}_i = \Sigma_j R_{ij} \vec{a}_j = \Sigma_j R'_{ij} \vec{a}'_j \tag{4}$$

where the elements R_{ij} and R'_{ij} are integral. Comparing with (1), we obtain readily

$$\underset{\sim}{B} = \underset{\sim}{R}^{-1} \underset{\sim}{R}' \tag{5}$$

in which the elements B_{ij} are rational.

(*) This definition of superlattice follows the one given by Santoro & Mighell (1972). In some publications (e.g., Cassels, 1971) a superlattice as defined here is called "sublattice" following the terminology of group theory.

From the above results, it follows that:

Theorem: "If two lattices Λ and Λ' have a superlattice Γ in common, they also have in common the derivative lattices Δ of Γ."

According to definitions given elsewhere (Santoro & Mighell, 1972), the derivative lattices Δ of Γ are all the lattices obtained from Γ with the transformation

$$\vec{d}_i = \Sigma_j \, L_{ij} \, \vec{s}_j \tag{6}$$

where the primitive triplet of translations $\vec{s}_i$ define Γ and the elements L_{ij} are rational numbers. From equations (6) and (4), we obtain

$$\vec{d}_i = \Sigma_j \, L_{ij} \, \Sigma_k \, R_{jk} \, \vec{a}_k = \Sigma_j \, L_{ij} \, \Sigma_\ell \, R'_{j\ell} \, \vec{a}'_\ell \tag{7}$$

The lattices Δ, therefore, are common to Λ and Λ' and can be obtained from $\vec{a}_i$ and $\vec{a}'_i$ with the matrices $\underset{\sim}{L}\underset{\sim}{R}$ and $\underset{\sim}{L}\underset{\sim}{R}'$, respectively.

If Λ and Λ' have a superlattice in common, matrix $\underset{\sim}{B}$ can always be expressed by means of the equation

$$\underset{\sim}{B} = \underset{\sim}{Q}^{-1} \, \underset{\sim}{P} \tag{8}$$

where the elements of $\underset{\sim}{P}$ and $\underset{\sim}{Q}$ are integral and $\underset{\sim}{Q}$, in addition, is upper triangular with

$$0 \leq Q_{ij} < Q_{jj} \quad \text{with} \quad i < j \tag{9}$$

Equation (8) has been used to derive algorithms for finding the smallest common superlattice and the largest common sublattice consistent with any given rational matrix $\underset{\sim}{B}$.

If not all the elements B_{ij} are rational, the lattice Λ and Λ' are not related to each other in any specialized manner, i.e., the two lattices do not have common geometric properties or features. The previous treatment shows that the rational solutions of equation (1) are the only solutions of crystallographic interest.

These can be found with the following procedure. Letting

$$A_{ij} = \vec{a}_i \cdot \vec{a}_j \quad , \quad A'_{ij} = \vec{a}'_i \cdot \vec{a}'_j \tag{10}$$

from equation (1), we obtain

$$\begin{aligned} A_{ij} &= (\Sigma_h B_{ih} \vec{a}'_h) \cdot (\Sigma_n B_{jn} \vec{a}'_n) = \\ &\Sigma_k \Sigma_\ell B_{ik} B_{j\ell} A'_{k\ell} \end{aligned} \tag{11}$$

Rational solutions of equations (11) can be found, if they exist, by substituting for the unknown elements B_{ik} and $B_{j\ell}$, rational numbers generated systematically in some convenient way, e.g., by writing

$$B_{ij} = N_{ij}/n_{ij}$$

and by assigning to N_{ij} and n_{ij} all possible integral values. In practical applications these integers can be limited to a small interval, for example (-5, 5), because the relationships of crystallographic interest usually involve simple rational numbers.

If two lattices are not related exactly, equation (11) becomes

$$\Sigma_k \Sigma_\ell B_{ik} B_{j\ell} A'_{k\ell} - A_{ij} = S_{ij} \tag{12}$$

The rational relationship between the two lattices will be acceptable or unacceptable depending on the magnitude of the values of S_{ij} that can be tolerated in a given problem.

2. Applications

a. Ambiguities in Determining Unit Cells From Powder Data

In the automatic indexing of powder patterns with the program of Visser (1969), the output consists of four candidate unit cells. The algorithm described in the previous section has been used to relate these cells with one another and with the correct unit cell, where known. Not uncommonly, two or more of the four lattices were found to be in a derivative relationship with each other and/or with the true lattice of the crystal.

An example has been encountered in the indexing of chromium phosphate hydrate. From a set of observed d-spacings, the best solution found by the indexing algorithm was

$$a = 6.030,\ b = 11.471,\ c = 11.711\ \text{Å};\ \alpha = 94.72,\ \beta = 97.72,\ \gamma = 99.49°$$

with a volume of the unit cell of 787.83 Å^3. A single crystal analysis carried out with a Syntex automated diffractometer, on the other hand, gave

$$a' = 6.003,\ b' = 6.007,\ c = 23.389\ \text{Å};\ \alpha' = 97.04,\ \beta' = 92.61,\ \gamma' = 110.16°$$

with a volume of 782.27 Å^3. Both these cells are reduced, and one must therefore conclude that they define different lattices. The $\underset{\sim}{B}$-matrix algorithm, applied to the two cells, established that they are related by the transformation

$$\vec{a}'_i = (\bar{1}00/\tfrac{1}{2}\ \tfrac{1}{2}\ 0/-\tfrac{1}{2}\ -\tfrac{1}{2}\ 2)\ \vec{a}_i \qquad (i = 1, 2, 3)$$

Since the determinant of the transformation matrix is unity and since there are fractional elements, the two lattices bear a composite relationship to each other.

This example shows that the cell determined by the indexing program is closely related to the correct cell. This is a consequence of the fact that the two lattices, being in a composite relationship, have many d-spacings in common. In this particular case the observed diffraction lines, because of accidental absences, are consistent almost equally well with either cell $\vec{a}_i$ or with cell $\vec{a}'_i$.

b. Relationship Between Cells Determined From Different Crystals of the Same Species

There are lattices in which two or more unit cells are dimensionally similar. This may cause problems in single-crystal work where it is necessary to use two or more individuals of the same material to collect a complete set of data. An example of such a lattice has been reported by DeCamp (1976) and is summarized below.

In a study of the structure of Condelphine Hydroiodide, two experimenters, using different crystals, described the crystal lattice by means of the two cells:

$$a = 9.34,\ b = 17.39,\ c = 9.10\ \text{Å};\ \alpha = 94.85,\ \beta = 119.15,\ \gamma = 88.57°$$

and

$$a' = 9.32,\ b' = 17.45,\ c' = 9.09\ \text{Å};\ \alpha' = 94.84,\ \beta' = 118.83,\ \gamma' = 86.50°$$

and the differences in lattice parameters were ascribed, at first, to experimental errors, especially absorption. Subsequent work revealed this not to be the case, because intensities of corresponding reflections differed far more than the experimental errors would justify. The application of the $\underset{\sim}{B}$-matrix algorithm immediately established the relation between the two cells which are transformed into one another by means of the expression

$$\vec{a}_i = (\bar{1}01/010/001)\ \vec{a}_i$$

In the original paper, reduction theory was used to show that the two cells describe the same lattice and to find the relation between them. The present method, however, has to be preferred in problems of this type, not only because it is more direct, but especially because there could be in the lattice more than two cells with similar parameters which would be revealed immediately by the $\underset{\sim}{B}$-matrix algorithm, but could not be detected by the reduction procedures.

c. Relation Between Different Unit Cells of the Same Crystal Determined by an Automated 4-Circle Diffractometer

In determining the unit cell of a crystal with a 4-circle diffractometer, there are cases in which accidental or systematic extinctions (as well as other causes) may lead to the choice in reciprocal space of a superlattice of the correct one. An example of this type of error was encountered in the study of the structure of 2,3-Dichloro-hydroxide-4-nitro-diphenyl iodonium ($C_{12}H_6Cl_2I\ NO_3$).

The solution of this structure was initially attempted by using the data collected on the basis of the unit cell

$$a = 13.595,\ b = 4.638,\ c = 10.321\ \text{Å},\ \alpha = \gamma = 90°,\ \beta = 81.72°$$

In the last stages of refinement, however, it was found that two different models refined equally well to an R factor of about 8%. This result could be ascribed to disorder in the structure or to an incorrect procedure in collecting the data. By mounting the crystal a second time, the following cell was determined:

$$a' = 15.928,\ b' = 18.271,\ c' = 4.623,\ \alpha' = \beta' = 90°,\ \gamma' = 105.58$$

The $\underset{\sim}{B}$-matrix algorithm immediately revealed that the two cells are related by the transformation

$$\vec{a}'_i = \begin{pmatrix} -1 & 0 & 1 \\ 1 & 0 & 1 \\ 0 & 1 & 0 \end{pmatrix} \vec{a}_i$$

This matrix shows that by using the first cell, only half of the data were collected and used in the structure determination. With the second cell, the structure was successfully solved and refined.

d. Studies of Related Structures

In many problems of crystal chemistry it is important to establish the relationship between two or more structures. In this area the $\underset{\sim}{B}$-matrix algorithm is particularly useful, as the following example illustrates.

In a systematic study of compounds structurally related to palmierite, $K_2Pb(SO_4)_2$, it was found that the powder pattern of the compound $Rb_2Pb(MnO_2)_2$, although similar to that of palmierite, could not be indexed on the basis of a hexagonal cell theoretically derived from chemical considerations and values of the ionic radii. The lattice of $Rb_2Pb(MnO_2)_2$ was found to be monoclinic instead of reduced form

$$\begin{pmatrix} \underset{\sim}{a}\cdot\underset{\sim}{a} & \underset{\sim}{b}\cdot\underset{\sim}{b} & \underset{\sim}{c}\cdot\underset{\sim}{c} \\ \underset{\sim}{b}\cdot\underset{\sim}{c} & \underset{\sim}{a}\cdot\underset{\sim}{c} & \underset{\sim}{a}\cdot\underset{\sim}{b} \end{pmatrix} = \begin{pmatrix} 36.578 & 64.481 & 109.60 \\ -18.264 & -0.077 & -18.14 \end{pmatrix}^{(*)}$$

This reduced form shows more specialization than the one required by a monoclinic C-centered cell, indicating that the lattice has derivative lattices of symmetry higher than monoclinic. The hexagonal lattice parameters of the Rb compound predicted on the basis of a preliminary analysis of the powder pattern and of the ionic radii involved, are

$$a = 6.058,\ c = 21.73\ \text{Å};\ \gamma = 120°$$

[the parameters of palmierite reported in NBS Monograph 25 (Morris, McMurdie, Evans, Paretzkin, deGroot, Hubburd, and Carmel, 1976) are $a = 5.4950(6)$, $c = 20.849(4)$] which gives the reduced form

$$\begin{pmatrix} 36.699 & 36.699 & 64.690 \\ 18.350 & 18.347 & 18.347 \end{pmatrix}^{(**)}$$

The $\underset{\sim}{B}$-matrix algorithm showed that the monoclinic lattice can be obtained from the hexagonal form with the transformations

$$(101/011/002) \quad (200/010/001) \quad (100/020/001)$$

This indicates that the monoclinic lattice can be oriented in space in three different ways with respect to the hexagonal lattice, i.e., it is possible to mutually orient three monoclinic individuals so that a common hexagonal sublattice propagates from one to the other with little or no disturbance. These are the conditions required to have twinning

---

(*) The transformation to obtain the conventional C-centered monoclinic cell from the reduced cell is

$$(\bar{1}\bar{2}0/\bar{1}00/00\bar{1})$$

(**) The transformation to obtain the conventional cell from the reduced cell is

$$(100/\bar{1}10/\bar{1}\bar{1}3)$$

(Santoro, 1974). The existence of twins in $Rb_2Pb(MnO_2)_2$ are, therefore, quite possible, and anyone working with single crystals of the compound should be aware of it.

e. Studies of the Geometrical Properties of Lattices

It has been shown (Santoro and Mighell, 1970) that in some lattices more than one cell is based on the shortest three noncoplanar translations. Gruber (1973) has shown that, at most, five different cells of this type may exist in the same lattice. For identification purposes, it is necessary to describe a crystal in terms of only one of these cells and the special conditions of reduction theory provide a way to make such selection.

On the other hand, there are cases in which it is useful to find and relate to one another all of the cells based on the shortest translations, and the $\underset{\sim}{B}$-matrix algorithm represents a simple procedure to study this type of problem. As an example, let us consider the lattice studied by Gruber (loc. cit.) and described by the cell

$$a = 2,\ b = c = 4\ \text{Å},\ \alpha = 60,\ \beta = 79.2,\ \gamma = 75.517°$$

As we require only the equality of cell edges, only the equations

$$A_{ii} = \Sigma_k \Sigma_\ell B_{ik} B_{i\ell} A_{k\ell} \quad (k,\ \ell,\ i = 1,\ 2,\ 3)$$

need to be satisfied and the required values of the elements B_{ij} are restricted to integers for which $|\underset{\sim}{B}| = 1$. The algorithm finds the five different cells in agreement with those found by Gruber.

3. Conclusions

In the previous section only a few examples of the application of the algorithm have been illustrated. Many more cases could have been given.

The method represents a practical tool to study inter- and intra-lattice relationships, and for this reason it is particularly suited to carry out research on the published crystallographic data now collected in the NBS Crystal Data File and JCPDS Powder Data File.

Applications of the procedure, underway or planned for the future, comprise cross-referencing of the single-crystal and powder data files, routine identification and registration procedures, and a systematic study of twinning, especially to clarify the relationship between the geometrical and structural aspects of twins.

---

1. Santoro, A. and Mighell, A. D., *Acta Cryst. A* 28, 284-287, (1972).
2. Cassels, J. W. S., *"An Introduction to the Geometry of Numbers,"* Springer-Verlag, (1971).
3. Delaunay, B., *Z. F. Kristall.* 84, 109-149, (1933).
4. Santoro, A. and Mighell, A. D., *Acta Cryst. A* 26, 124-127, (1970).
5. International Tables for X-ray Crystallography, Vol. I, p. 7, Kynoch Press, (1969).
6. Visser, J. W., *J. Appl. Cryst.* 2, 89-95, (1969).
7. DeCamp, W. H., *Acta Cryst. B* 32, 2257-2258, (1976).
8. Santoro, A., *Acta Cryst. A* 30, 224-231, (1974).
9. Gruber, B., *Acta Cryst. A* 29, 433-440, (1973).
10. Donnay, J. D. H. and Ondik, H. M. , Crystal Data Determinitive Tables, Third Edition. U. S. Department of Commerce, National Bureau of Standards and the JCPDS - International Center for Diffraction Data, Swarthmore, PA., (1972).
11. Morris, M. C., McMurdie, H. F., Evans, E. H., Paretzkin, B., DeGroot, J. H., Weeks, B. S., and Newberry, R. J., *(National Bureau of Standards Monograph)* 25, Section 15, 63, (1978).

THERMAL RELAXATION IN A LIQUID UNDER SHOCK COMPRESSION

D. H. Tsai
(Thermal Physics Division)
and
S. F. Trevino
(Energetic Materials Division, LCWSL, ARRADCOM, Dover, NJ)

We have carried out a molecular-dynamical study of the shock compression of a dense three-dimensional liquid. Our system consists of 7200 particles interacting through a Lennard-Jones potential $\phi = 4\varepsilon[(\sigma/4)^{12} - (\sigma/r)^{6}]$ with ε and σ adjusted to simulate argon.[1] The range of interaction extends to about 2.5 σ. The particles form a filament with a cross-section of 9.9 σ x 9.9 σ and a length of 170 σ. The undisturbed portion of the filament is maintained at equilibrium throughout the calculation. Shock compression is initiated by causing the filament to move with a mass velocity of $-U_p$ in the longitudinal direction along the Z axis toward the origin, and to collide with its image through a mirror plane located at Z=0. The boundary conditions in the transverse (X-Y) directions are assumed to be periodic. We calculate the response of the filament under these initial and boundary conditions by solving numerically the classical equations of motion for all the particles in the filament. From the positions and velocities of all the particles as functions of time we calculate the profiles of mass density, energy density, kinetic temperature and stress components, and thus obtain an atomistic description of the shock compression process in a dense liquid system under fully non-equilibrium conditions.

We have two main objectives in this investigation. First, we wish to compare these results for the discrete model of a dense liquid system with the results for a continuum model.[1] The continuum model usually assumes that local equilibrium exists in the shock profile, even within the thickness of the shock front where conditions change most rapidly. Second, we wish to study the thermal relaxation process in the dense liquid following the passage of the shock front and to compare this relaxation process with that obtained earlier[2] in a crystalline solid under similar condition of shock compression. In addition, the recent work of Klimenko and Dremin[3] has just come to our attention. These authors have also made molecular dynamical calculations of the shock compression of liquid argon. Their system is similar to ours, and it would be interesting to compare their results with ours.

We have completed two calculations in which the initial configurations of the uncompressed liquid (subscript 1) were different, but both corresponded to the same equilibrium conditions as follows: $\rho_1 = 0.85/\sigma^3$, $T_1 = 1.16\ \varepsilon/k$, $P_1 = 3.18\ \varepsilon/\sigma^3$ with $\varepsilon = 120\ k$ and $\sigma = 0.3405$ nm. U_p is taken to be 0.2 C_o where $C_o = 9.46\sqrt{\varepsilon/m}$ is the longitudinal sound velocity in a fcc crystal of argon at zero pressure and zero temperature and m is the atomic mass of argon. U_p is then approximately 300 m/s. In his study of the continuum solution based on the Navier-Stokes description of strong shock waves in a liquid, Hoover[1] has also obtained one set of solutions under conditions similar to ours. We compare our results with his as follows (subscript 2 refers to conditions at the high pressure side of the shock front profile; ρ, P and T in proper units; U_s is shock front velocity):

	ρ_1	P_1	T_1	ρ_2	P_2	T_2	U_S/C_o
Ours	0.85	3.18±.31*	1.16±.03	1.04	-16	2.09	1.109
Hoover's	0.85	2.86*	1.16	1.05	21.24	2.24	1.133

*Disagreement here is due to slight differences in the cutoff of the Lennard-Jones potential and in the treatment of the correction term beyond the cutoff. See D. H. Tsai, J. Chem. Phys. 70, 1375 (1979).

Our values are the "best" average values taken from a number of time steps between $\tau = 140$ and 160 at the end of the calculation, where τ is measured in d/C_o, d being the interplanar spacing of the fcc argon at zero pressure and zero temperature. By this time, the shock front profile is essentially steady. However, additional data would be useful for reducing the fluctuation in the data. We obtain a shock front thickness of 14.9 σ as compared with 17.6 σ obtained by Hoover. The two profiles are qualitatively similar, but the maximum gradients in our profile are noticeably higher than Hoover's. This similarity does not suggest that the viscosity coefficients in Hoover's calculations are "correct," because even with zero viscosity, as in a model of a one-dimensional solid, the discrete model still gives a shock front profile of 5-10 lattice spacings thick (similar to that in our three-dimensional liquid or solid), whereas the Navier-Stokes continuum solution would give a shock front of zero thickness.

Our results are also in qualitative agreement with the results of Klimenko and Dremin.[3] For example, we also find a marked difference in the longitudinal and transverse components of the kinetic temperature within the thickness of the shock front. However, we have allowed the shock wave to propagate considerably farther than the Russian authors did, by a factor of 4 or 5, so that we may also investigate the energy relaxation process behind the shock front.

Figure 1 shows the average kinetic temperature profile from three time steps near $\tau = 160$, at $U_p = 0.2\ C_o$. In this case the temperature rise immediately following the shock front is 15% higher than that in the trailing portion farther behind. Here we ignore that part of the profile adjacent to the mirror plane at $Z=0$ where the boundary conditions introduce some disturbance to the system. The corresponding pressure profile gives a uniform pressure over the entire profile. The corresponding mass density immediately following the shock front is 1% lower than that in the region farther behind. The conservation of energy (and of momentum) for the entire calculation is better than 0.5%. These considerations indicate that the temperature difference in figure 1 is real and not an artifact of the numerical computation. If this is indeed so, this result is in harmony with our understanding of the thermal relaxation process in a crystalline solid[2], i.e., in a dense system under shock compression, equilibration of thermal energy in the shock profile is slower than the equilibration of momentum

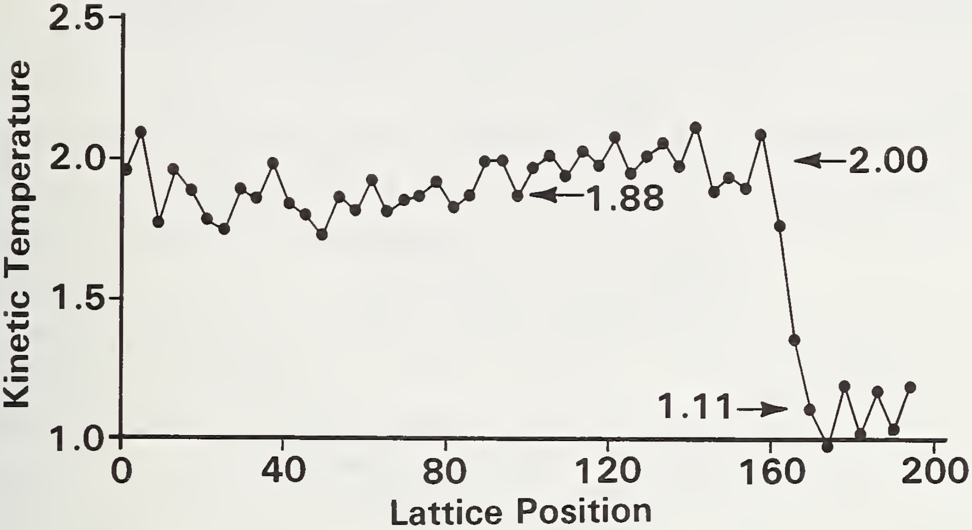

Figure 1. Average kinetic temperature profile from three time steps at $\tau = 159$, 159.5, and 160. $U_p = 0.2\ C_o$, other conditions as given in the text.

which follows immediately behind the shock front. In analogy to the crystalline case, we believe that the propagation of the thermally equilibrated region behind a shock front may be identified as second sound in a liquid. But further work is required to establish this point on a satisfactory basis.

---

1. W. G. Hoover, *Phys. Rev. Lett.* 42, 1531 (1979).

2. D. H. Tsai and R. A. MacDonald, *High Temperatures-High Pressures,* 8, 403 (1976); R. A. MacDonald and D. H. Tsai, *Physics Reports,* 46, 1 (1978).

3. V. Y. Klimenko and A. N. Dremin, *Detonatsiya, Chernogolovka, Akad. Nauk USSR (O. N. Breusov, et al. eds)* 79 (1978). We thank Dr. Hoover for giving us this reference.

ON THE MEASUREMENT OF SINGLE CHAIN NEUTRON SCATTERING IN CONCENTRATED POLYMER SOLUTIONS

Charles C. Han
(Polymer Science and Standard Division)

and

Chung Yup Kim and Hyuk Yu
(Department of Chemistry
University of Wisconsin
Madison, WI)

and

A. Z. Akcasu and G. C. Summerfield
(Department of Nuclear Engineering
The University of Michigan
Ann Arbor, MI)

and

S. N. Jahshan
(Department of Engineering Science,
Aerospace-Engineering, and Nuclear Engineering
State University of New York
Buffalo, NY)

A number of authors[1-5] have reported the measurement of single chain polymer configurations in concentrated solutions and in bulk using small angle neutron scattering and samples composed of mixtures of normal and deuterated polymers. The measurements of the single chain configurations have always involved taking the limit of small relative concentrations of the deuterated polymer. This was done to eliminate interference effects in scattering from different chains. The difficulty with this procedure is, of course, that it emphasizes the least reliable results, namely those from the small relative concentrations of marked polymer.

Most analyses that have been done thus far seem to have relied on ideas that were developed for light and x-ray scattering where the limit of zero concentration was required to eliminate the interchain interference. With the introduction of isotopic marking, one has an entirely new dimension. That is, the scattering signal from the marked chains can be changed without any change in the underlying solvent polymer interactions. This is done by changing the relative normal and marked polymer concentrations while keeping the overall polymer concentration the same. As we shall see, this permits the measurement of the single chain scattering without taking limiting values of small concentrations of the marked polymer. Another way of stating this is that the "background" correction can be made by simply performing experiments at different concentrations of marked polymer.

Suppose we have a solution composed of solvent molecules at positions $\underline{R}_S$ and polymer molecules with centers of mass at $\underline{R}_M$ and monomers at $\underline{r}_j$. The concentrations of solvent and polymer are taken to be c_S [molecules/cm^3] and c_P [monomers/cm^3], respectively. Further, we assume that some of the polymer molecules are "marked" by having deuterium substituted for all of the protons. If we take the concentrations of marked and normal polymer to be c_D and c_H, respectively, we have

$$c_P = c_D + c_H \tag{1}$$

If we assume that the solution is in compressible in which case, we have shown[6] the intermediate coherent neutron small angle scattering function is

$$S(\underline{Q},t) =$$

$$< (\overline{a_P} - a'_S)^2 \sum_{MjM'j'} \exp[i\underline{Q}\cdot(\underline{R}_M+\underline{r}_j)] \exp[-i\underline{Q}\cdot(\underline{R}_{M'}(t) + \underline{r}_{j'}(t))] >$$

$$+ < (\overline{a_P^2} - \overline{a}_P^2) \sum_{Mjj'} \exp[i\underline{Q}\cdot(\underline{R}_M+\underline{r}_j)] \exp[-i\underline{Q}\cdot(\underline{R}_M(t) + \underline{r}_{j'}(t))] > \tag{2}$$

where

$$a'_S = \frac{V_P}{V_S} a_S$$

$a_M = \bar{a}_P$, with S, M and P stand for solvent, inonomer and polymer. Also, since part of the polymers are marked by deuteration, we will have

$$\bar{a}_P = \frac{c_H}{c_P} a_H + \frac{c_D}{c_P} a_D = a_H + (a_D - a_H) \frac{c_D}{c_P}$$

$$\overline{a_P^2} - (\bar{a}_P)^2 = \frac{c_D}{c_P} (1 - \frac{c_D}{c_P}) (a_H - a_D)^2$$

and

$$(\bar{a}_P - a'_S)^2 = [a_H - a'_S + (a_D - a_H) \frac{c_D}{c_P}]^2$$

In fact we need only divide the measured S(Q,t) at two values of c_D by the factors $(\bar{a}_P - a'_S)^2$ at those values of c_D and subtract to obtain the single chain contributions. Also, we can in some cases, choose the solvent and the ratio c_D/c_H to give

$$\bar{a}_P = a'_S$$

which eliminates everything but the single chain term in (2).

Now let us specialize to the case of elastic scattering in bulk material for which (2) reduces to

$$S(Q) = < (\bar{a}_P)^2 \left| \sum_{Mj} \exp[i\underline{Q}\cdot(\underline{R}_M+\underline{r}_j)] \right|^2 >$$

$$+ < (\overline{a_P^2} - (\bar{a}_P)^2 N_P \left| \sum_{j} \exp[i\underline{Q}\cdot\underline{r}_j] \right|^2 > \qquad (3)$$

where N_P is the total number of polymer chains in the sample.

We have used two samples composed of mixtures of polyisoprene and deuterated polyisoprene. The molecular weight, as measured by Gel Permeaton Chromatography, of the deuterated polyisoprene was 10^4 g/mol. The first sample contained 6.9 weight percent deuterated polyisoprene. This gives the average monomer scattering length for sample one to be

$$\overline{a_P}(1) = 0.79 \times 10^{-12} \text{ cm.}$$

The second sample contained 14.5 weight percent deuterated material with

$$\overline{a_P}(2) = 1.36 \times 10^{-12} \text{ cm.}$$

The SANS experiments were performed at the NBS reactor. The neutron beam had 5.8 A wavelength with a resolution of 1 A. It was obtained using a helical slot velocity selector and nitrogen cooled Be and Pb filters. Beam size at the sample was 8 mm x 8 mm and a 50-cm linear position sensitive He-3 detector was used. Data acquisition time for each sample was approximately forty hours. The background and incoherent scattering were measured and subtracted for each sample to give the total coherent scattering for each sample, $I_1(Q)$ and $I_2(Q)$. From our earlier results, it is clear that the single chain from factors

$$S_S(\underline{Q}) = \qquad \exp[i\underline{Q}\cdot\underline{r}_1]^{2} \tag{4}$$

can be obtained from I_1 and I_2 as follows

$$S_S(\underline{Q}) = K \quad \frac{I_2(Q)}{|\overline{a_P}(2)|^2} - \frac{I_1(Q)}{|\overline{a_P}(1)|^2} \tag{5}$$

where K is a constant.

The $S_S(Q)$ obtained in this experiment is shown in Figures 1 and 2. The solid points are the measured values while the solid and broken curves are computations using the Debye form factor for gaussian coils at various values of the radius of gyration R_g. The scatter in these data is smaller by an order of magnitude than similar data taken earlier on polybutadiene using a low concentration of marked polymer.[7]

We can see from Figure 1 that the Debye form factor with an R_g of 34 A fits the data reasonably well over the range of the measurements. A Zimm plot of the data in the Guinier range ($Q R_g < 1$) gives an R_g of 33 ± 4 A, while fitting the data to the Debye form factor with varying values of R_g gives an R_g of 33.9 ± 0.8 A. The minimum, unperturbed value of R_g for polyisoprene occurs for 1,2-addition products and sydiotactic placements. This value for the molecular weight here is 28.9 A. The maximum value occurs for trans 1,4-addition products and is 39.8 A.

Our results and those of Williams *et al.*[8], show that one can measure single chain form factors for bulk polymer and concentrated solutions using large ratios of marked to normal polymer. The practical impact of this is that the flux requirements to perform any particular experiment are reduced by at least an order of magnitude. This means

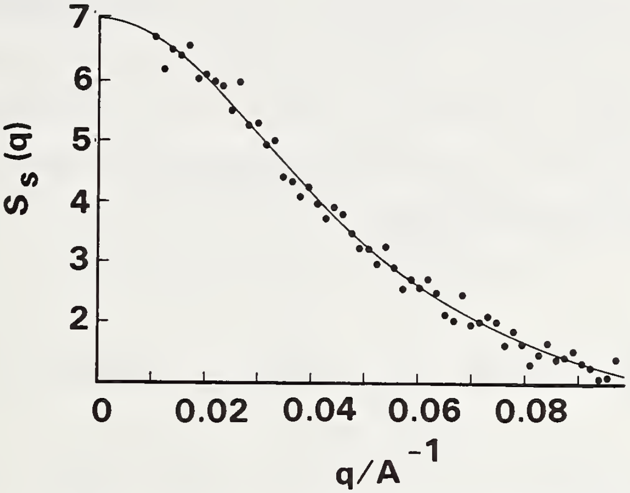

Figure 1. $S_S(Q)$ in arbitrary units for polyisoprene. The solid curve is the Debye form factor for a gaussian coil with an R_g of 34 A.

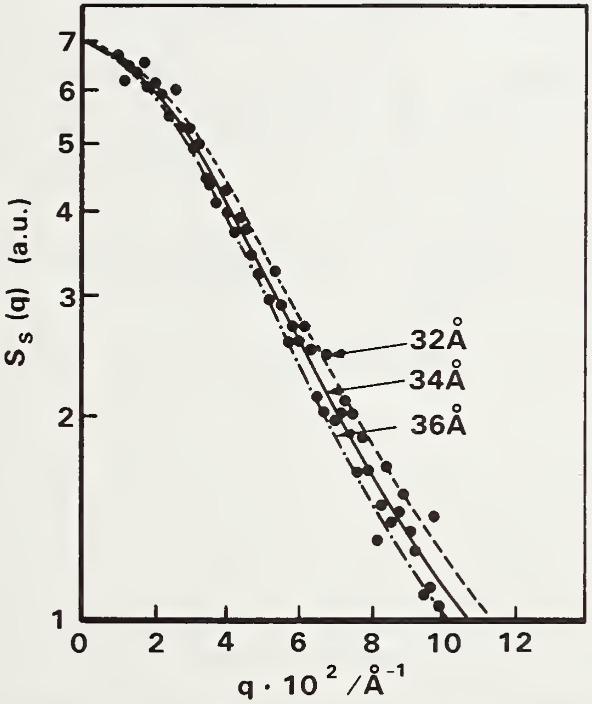

Figure 2. Comparison of the measured $S_S(Q)$ and gaussian coil calculations for three values of R_g, 32, 34, and 36 A. The best fit is given by $R_g = 33.9 \pm 0.8$ A.

that previously impossible experiments, such as the polyelectrolyte solution measured by Williams, et al., can now be done at the highest flux facilities. Other experiments, such as the polyisoprene experiment, described here, can now be done at facilities of more modest flux such as NBS reactor with precision.

---

1. R. G. Kirste, W. A. Kruse, and J. Schelten, *Makromol. Chem.* 162, 299 (1973).
2. J. P. Cotton, B. Farnoux, G. Jannink, J. Mons, and C. Picot, *Compt. Rend. Acad. Sci. (Paris),* 275 3C, 175 (1972).
3. H. Benoit, J. P. Cotton, D. Decker, B. Farnoux, J. S. Higgins, G. Jannink, R. Ober, and C. Picot, *Nature, Phys. Sci.* 245, 13 (1973).
4. J. P. Cotton, B. Farnoux, G. Jannink, C. Picot, and G. C. Summerfield, *J. Polymer Sci., Symp. No.* 42, 807 (1973).
5. J. P. Cotton, D. Decker, B. Farnoux, G. Jannink, R. Ober, and C. Picot, *Phys. Rev. Letters* 32, 1170 (1974).
6. A. Z. Akcasu, G. C. Summerfield, S. N. Jahshan, C. C. Han, C. Y. Kim and H. Yu, (To be published).
7. Jeffrey A. Hinkley, Charles C. Han, Bernard Mozer, and Hyuk Yu, *Macromolecules* 4, 836 (1978).
8. C. Williams, et al., *J. Polymer Sci. Letters* (to be published).

CRITICAL EXPONENTS FOR ^{4}He AT THE GAS-LIQUID PHASE TRANSITION

Bernard Mozer

and

Bernard Le Neindre
(Laboratoire des Interactions Moleculaires
et des Hautes Pressions
Centre Universitaire Paris Nord
Villetaneuse, France)

and

John R. D. Copley[1]
(Institut Laue-Langevin
Grenoble, France)

Small angle neutron diffraction measurements were obtained from ^{4}He in the vicinity of the gas-liquid phase transition. Diffraction patterns varying from κ(wave vector difference) = 0.01 to 0.125 Å^{-1} were taken for each temperature in the reduced temperature range 0.25 to 10^{-4} for a fixed value of the helium density at its critical value. The thermodynamic measurements of density and temperature were made in the gas and liquid phases for calibration of the system and were accurate to better than 1% in density and limited to an accuracy in relative temperature from 0.25 mK fluctuations on the control block. Raw neutron data was corrected for background from the sample container and environment, response of the area detector, and multiple scattering. Normalization of the response of the area detector was determined from the scattering of water. Extensive calculations were made for the correction factors for angular resolution of the incoming beam and of the scattering and detector configuration as well as wave length distribution of the incoming beam. Additional diffraction data was obtained at 8 to 10 K at the critical density and at reduced densities along the isotherm of the critical temperature. Preliminary data analysis of the corrected structure factor enabled us to determine the critical exponents η (deviation from Ornstein-Zernike theory), γ (isothermal compressibility), and ν (correlation length). γ and ν were determined in the reduced temperature range 0.025 to 0.001 and η determined in the range of reduced temperatures less than 0.001. The following table shows the values of these exponents

$$\eta = 0.10 \pm 0.05$$
$$\gamma = 1.16 \pm 0.05$$
$$\nu = 0.63 \pm 0.03$$

More extensive data analysis is being undertaken to refine the values of these exponents and to seek estimates for other exponents associated with corrections to the scaling hypothesis.

---

1. Now at McMaster University, Hamilton, Ontario, Canada

PHASE TRANSITION IN AMMONIUM NITRATE

C. S. Choi and H. J. Prask
(Energetic Materials Division, LCWSL, ARRADCOM, Dover, NJ)
and
(National Bureau of Standards, Washington, DC)
and
E. Prince

Ammonium nitrate (AN) is hygroscopic and crystallizes in at least five different polymorphic forms at atmospheric pressure, the existence of which leads to serious problems for the utilization of AN in certain practical applications. In particular, the phase transition between phase IV (-18°C to 32°C) and phase III (32°C to 84°C) is accompanied by a large change in volume, which causes irreversible growth, break-up and caking of cast or pellitized AN. The occurence of phase III, however, depends on the presence of water ($\gtrsim$ 0.1 wt%) which suggests the possiblity, that dopants might be found which would counteract the effect of water and eliminate phase III. Our recent work on AN has included structural studies of AN with dopants and of pure AN to understand the effect of water or dopants on the bonding.

1. Ammonium Nitrate Doped with 2 wt.% NiO or CuO[1]

Neutron powder diffraction data of these samples were taken at room temperature and in 20K steps from 260K to 80K using the multi-detector powder diffractometer. The diffraction patterns at each temperature were analyzed by the Rietveld profile refinement method and the following results were obtained:

a. The AN/metal oxide system was found to be a solid solution with the AN structure and with the metal oxide complex occurring at random in interstitial positions.

b. Temperature ranges of phase (IV) are -133°C to 55°C for the AN/NiO solid solution, and -63°C to 55°C for the AN/CuO solid solution.

c. Unit cell dimensions of these doped samples were clearly different from pure AN.

d. Thermal expansion coefficients, α (where $a_i = \alpha_i(330 - T)^{\frac{1}{2}} + a_i^o$ were determined from the unit cell dimensions of the AN/NiO solid solution at nine different temperatures by a non-linear least-square fit.

The results, as shown in table 1, indicate strong anisotropic thermal expansion in the phase (IV) structure.

2. Hydrogen Bonding in the Phase (III) Structure

The solid solution of KNO_3 in NH_4NO_3 crystallizes in the phase (III) structure of NH_4NO_3 at room temperature if the concentration of KNO_3 is 3 wt% or more. Neutron powder diffraction data were measured from NH_4NO_3-5 wt% KNO_3 solid solution at room temperature using the 5-detector powder diffractometer with collimation of 10'-20'-10'. Since the structure of non-hydrogeneus atoms were well known by the x-ray single crystal study of Holden and Dickenson[2], Hydrogen positions only were determined by a Rietveld profile refinement. The results are given in table 2. One oxygen atom of each nitrate group is hydrogen-bonded to two adjacent ammonium groups to make a linear hydrogen-bond chain running parallel to b-axis in the phase (III) structure, as shown in figure 1. The parameters of this N-H . . . O type hydrogen bond are 0.96 Å, 2.17 Å and 142° for the N-H and H . . . O distances and the N-H . . . O angle respectively.

The strong two-dimensional hydrogen bond network which occurs in the phase (IV) structure is broken systematically along one direction and becomes a one-dimensional chain (with weaker O . . .H bond) in the phase (III) form.

3. Disordered Model of the Phase (II) Structure

In a previous study of the phase (II) structure[3], we have refined a model structure derived from phase (IV) with space group $P\bar{4}2_1m$. Recently, Lucas et. al.[4] using powder neutron diffraction data have refined the structure of a disordered model proposed by Shinnaka and obtained an excellent result. However, there are several difficulties associated with the disordered model of Lucas et al. Therefore, to further test this model we have reinvestigated the phase II structure, also by powder neutron diffraction. In our case the diffraction intensities were measured from NH_4NO_3 (doped with 3 wt% NiO) at 65°C to reduce thermal motion. To minimize incoherent contributions, a 3-axis spectrometer with 45'-40'-40'-20' collimation was used at a wavelength of 1.5077Å.

We have refined two distinct structures with our data: firstly, an ordered structure in the $P\bar{4}2_1m$ space group; secondly, a static disordered model with space group P4/m b m. The later is equivalent to the constrained disorder model of Lucas et al. with space group $P\bar{4}2_1m$. Using isotropic temperature factors for the H-atoms and anisotropic factors for the other atoms, weighted R-factors of 0.034 and 0.030 were obtained for the ordered and disordered models, respectively. However, in the ordered model, the NO_3 group tended to distort and the O-atom thermal motion became unphysically large. Least-squares parameters are given in table 3 for the disordered model.

Table 1. Thermal expansion coefficients of phase (IV) expressed in a form; $a_i = \alpha_i (330 - T)^{1/2} + a_i^o$ where a_i and a_i^o in angstrum unit, and T in Kelvin temperature.

axis	α_i	a_i^o(A)	X_i (%)
a	0.00124(12)	5.7485(13)	0.118
b	-0.02234(53)	5.5586(55)	0.512
c	-0.00332(15)	4.9390(15)	0.145

Table 2. Least squares parameters of AN-KN phase (III) structure.

Atom	X	Y	Z	B
H_1	-0.128(4)	3/4	0.370(4)	15.(1)
H_2	0.071(3)	3/4	0.412(4)	14.(1)
H_3	0.005(2)	0.893(2)	0.242(2)	13.(1)

Unit cell: a = 7.6789(4)

b = 5.8223(3)

c = 7.1404(4)

v = 319.24(2)

Table 3. Least squares parameters of phase (II) structure (disordered model) with P4/mbm space group.

Atom	X	Y	Z	B
NH	0.	0	1/2	βij
NO	0.	1/2	0.022(2)	βij
O_1	0.	1/2	0.275(2)	βij
O_2	0.131(1)	1/2-X	-0.101(1)	βij
H	0.141(1)	-0.016(4)	-0.382(1)	7.1(3)

Unit cell: a = 5.6955(3)

b = 5.6955(3)

e = 4.9198(5)

v = 159.59(2)

---

1. W. Engel, *Explosivstoffe, No. 1,* 1973.
2. J. R. Holden & C. W. Dickenson, *J. Phys. Chem.,* 79, 249, 1975.
3. C. S. Choi, *NBS Tech Note* 995, 1978.
4. B. W. Lucas, M. Ahtee and A. W. Hewat, *Acta. Cryst.* B35, 1038-1041.

NONDESTRUCTIVE DETERMINATION OF TEXTURE IN COLD-WORKED TUNGSTEN ALLOYS

C. S. Choi and H. J. Prask
(Energetic Materials Division, LCWSL, ARRADCOM, Dover, NJ)
and
(National Bureau of Standards, Washington, DC)

The Army group at the NBSR has been engaged in a continuing program to apply neutron diffraction to NDT problems of military importance.[1,2] Recent efforts in this area have centered upon the nondestructive determination of texture in cold-worked, tungsten-alloy samples which are used in certain anti-tank munitions. Some aspects of the problem have significance beyond the military application and illustrate the complementary character of x-ray and neutron diffraction probes.

The samples are composed of tungsten, nickel and iron in a wt % ratio of 97/1.8/1.2. Sample preparation - which involves isostatic pressing, sintering, heat treatment, and cold working - leads to a system consisting of a "tungsten" phase (96.5 wt %) and a "matrix" phase (3.5 wt %). The approximate compositions by weight of the two phases are 99.7W - 0.1Ni - 0.2Fe and 55Ni - 23Fe - 22W, respectively. The potential of neutron diffraction for studies of this type of sample can be inferred from figure 1 in which partial x-ray and neutron diffraction patterns which cover the same range in d-spacing are shown. The full diffraction patterns show that the tungsten phase can be indexed according to the bcc tungsten structure with a = 3.160(1) A, and the matrix phase can be indexed according to a fcc nickel structure with a = 3.586(1) A. For alloys of these compositions and relative concentrations, Bragg peaks corresponding to the matrix phase are virtually invisible to x-rays. In contrast, two matrix-phase peaks are clearly visible in the neutron pattern which makes possible texture studies and, in principal, residual stress studies of the matrix phase.

Texture resulting from various types of cold-working have been

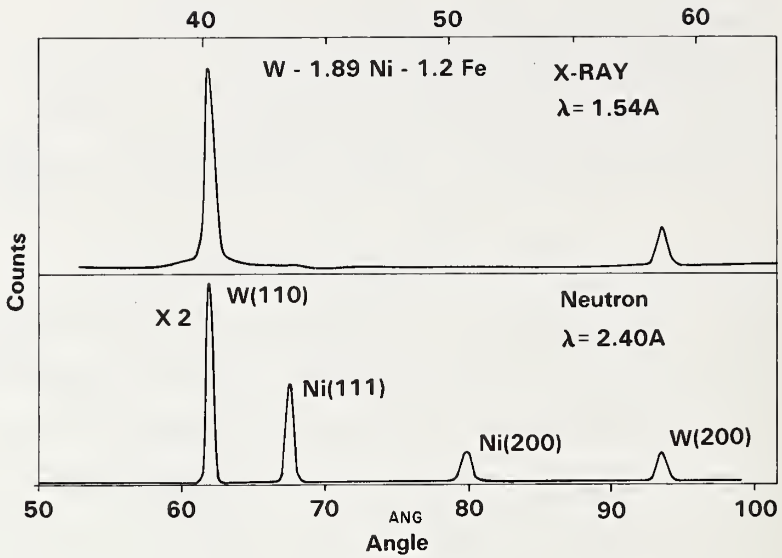

Figure 1. Partial X-ray and neutron diffraction patterns for a two-phase tungsten-alloy system. The tungsten-rich phase exhibits a bcc structure; the "matrix-phase" exhibits a nickel-like fcc structure. Other details are given in the text.

measured for these types of alloys. In figure 2 are shown pole-figure patterns for one matrix-phase and two tungsten-phase reflections. The three sets of pole figures correspond to cylindrical samples which have been cold-worked by "upsetting" with an 8% increase in cross-section (5904B), and swaged with an 8% decrease in cross-section (5903B and 5905J). Cold-working of the latter pair was performed at two different fabrication facilities. As one would expect, the fiber textures of the "upset" and swaged samples are different. On the other hand, the pattern of sample 5903B is essentially untextured whereas that of 5905J shows definite texture in the tungsten phase for nominally, the same cold-working. The matrix phase (111) pattern shows little if any clear texture.

In contrast to the above results, samples which have been swaged to a 16% reduction in area show very pronounced tungsten and matrix phase textures. As shown in figure 3, the matrix-phase (111) pattern exhibits a more pronounced fiber texture than the tungsten-phase (110) pattern.

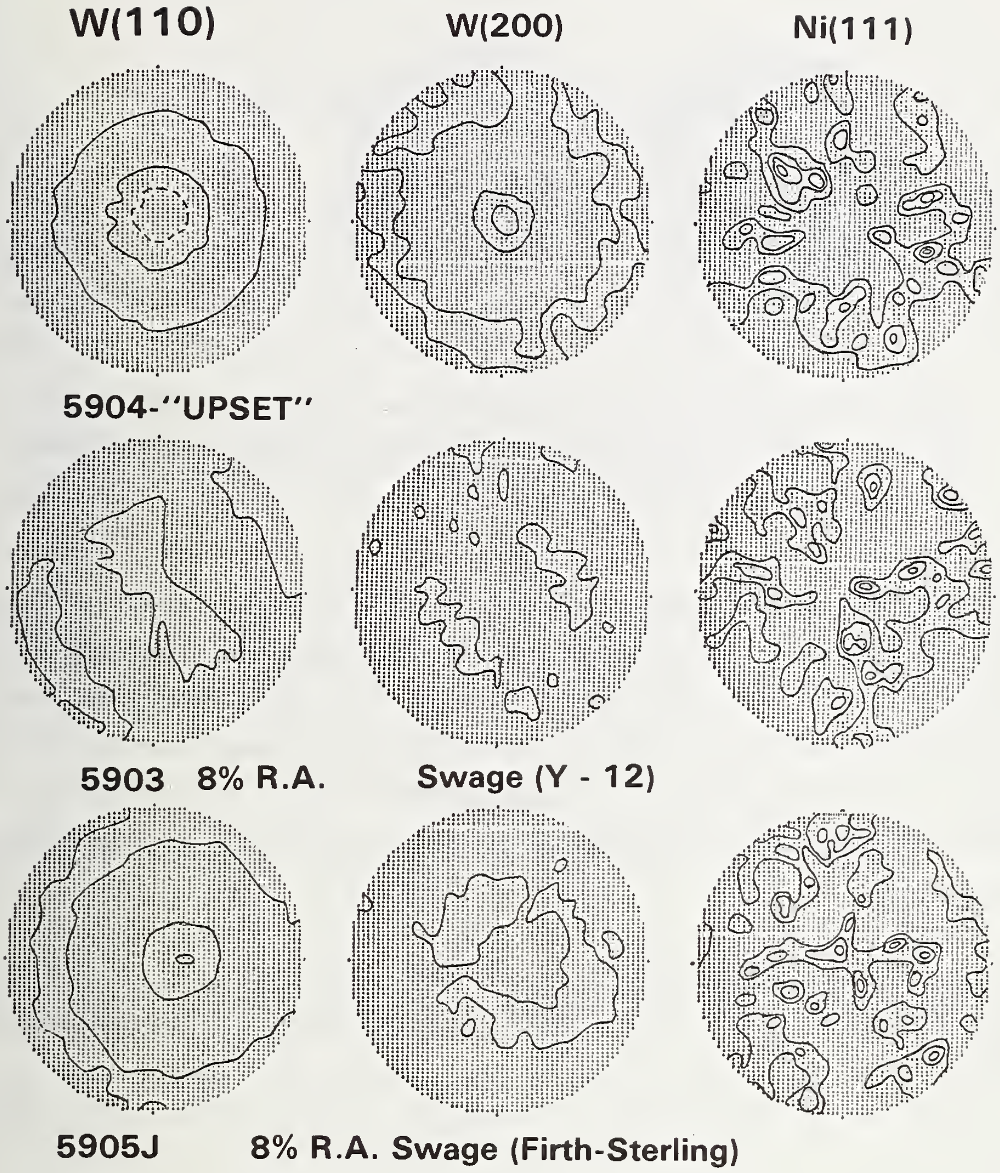

Figure 2. Neutron diffraction pole figures for three of the tungsten- and matrix-phase reflections shown in Figure 1. The samples were 0.7 cm diameter cylinders, approximately 10 cm in length. The center of each figure corresponds to a configuration in which the scattering vector is aligned with the cylinder axis. Fabrication of the three samples is described in the text.

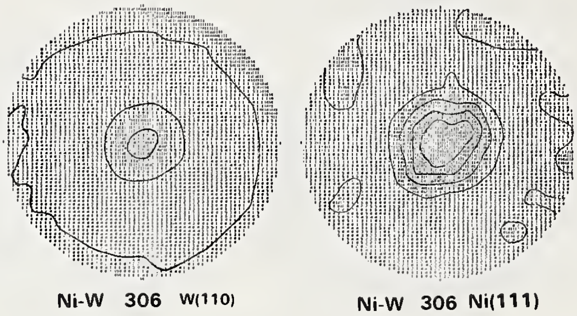

Figure 3. Tungsten-phase (110) and matrix-phase (111) textures for a 16% R.A. swaged sample. In this case the data were obtained at the center-line of a piece cut from a full-scale (∿3 cm diameter) production-type sample.

In summary, the neutron diffraction study of texture in these samples reveals some differences resulting from cold-working that would not have been observable with x-ray diffraction alone. Although the significance of the measurements as they relate to ductility, hardness, etc. is not determined, it is clear that the nondestructive nature of the neutron probe allows empirical correlations to be made between measured properties and performance.

---

1. C. S. Choi et al., *NBS Tech. Note 995*, p. 34 (1979), and references cited.

2. C. S. Choi, H. J. Prask and S. F. Trevino, *J. Appl. Cryst.*, <u>12</u>, 327, (1979

C. NON-RRD PROGRAMS

ACTIVATION ANALYSIS: SUMMARY OF 1979 ACTIVITIES

Rolf Zeisler

As part of the Inorganic Analytical Research Division, Center for Analytical Chemistry, the Activation Analysis Group is physically located in the NBS-Reactor building. It has at present a staff of 7 full-time members who are conducting research in the development and application of advanced nuclear analysis techniques. The scope of the work is within the following functions of the National Bureau of Standards: the preparation and distribution of standard reference materials and their use in chemical analysis, and the development of methods of chemical analysis.

The Neutron Activation Analysis (NAA) program included numerous measurements at a high level of precision and accuracy in support of the Standard Reference Materials programs which include the certifications of inorganic and organic compounds for the chemical composition (major, minor, and trace elements). The Activation Analysis Group continually develops or modifies new procedures in order to support the SRM certification with improved precision and accuracy. In addition to the lasting support to the NBS Center for Analytical Chemistry, the group has participated in other agency programs and has made significant contributions by developing improved methodology and demonstrating its applications. Such interactions impart the analytical expertise of the group and the NBS to where it is needed.

This report summarizes the activities of the Activation Analysis Group during the period of July 1978-June 1979. Included are contributions in the areas of basic research, applied research, certifications, and non-NBS research programs.

1. Basic Research in Nuclear Analysis

a. Major Elemental Boron Determination by Nuclear Track Counting

J. W. Mitchell and J. E. Riley, Jr. (Bell Laboratories, Murray Hill, NJ)
B. S. Carpenter

Determinations of boron, when present as a major element (0.5 to 50%), are susceptible to many matrix interferences during chemical analyses. Although most interferences can be eliminated by chemically separating boron as the volatile methyl ester, this procedure requires tedius and time consuming sample processing steps which result in low sample throughout. In contrast, the nondestructive nuclear track counting technique for determining boron is inherently fast and capable of high precision and accuracy. Investigations are now underway to determine the reliability of the method for determining the homogeneity of the distribution of boron in glass and to measure major amounts of this element in optical waveguide materials.

Reproducible conditions for irradiating samples at the neutron beam tube (flux 3.5×10^5 n/cm^2 sec) have been provided by the sample irradiation chamber shown in figures 1a and b. The sample (1.27 cm dia disk) is placed between appropriate detector film and clamped securely into holder (A), which is in turn attached to apparatus part (B). After the boral curtain of the reactor is raised, the boral shutter assembly, (C), in the irradiation chamber is used to block the neutron beam. The irradiation chamber lid (D), is then raised, and the assembled sample holder unit (A+B) is then placed on a track which guides it into the irradiation chamber, and reproducibly positions it at the center of the beam part. The shutter (C) is raised, held in the beam open position (figure 1b), and lowered at the end of the desired irradiation period. Continuous use of the sample chamber during an eight hour period has resulted in minimal activation of the aluminum-boral chamber parts.

A series of borosilicate glasses of the nominal compositions listed in table 1 have been irradiated. Preliminary optical microscopic

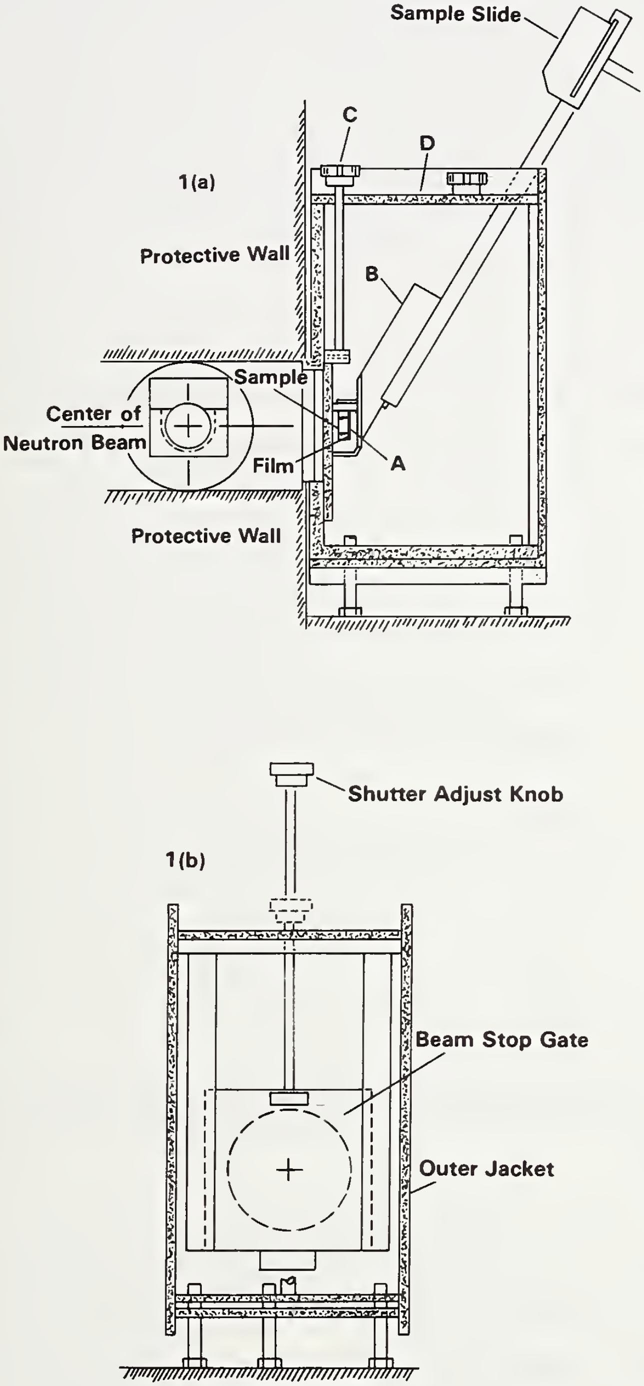

Figure 1. Sample irradiation chamber.

examinations of detectors indicate homogeneities sufficient for use of these specimens as comparison standards. Detailed determinations of alpha track densities over many fields of view are being made via image analyses and determinations of boron content using chemical procedures are underway. This series of samples will be used subsequently to examine the quantitative reliability of the nuclear track method at high boron levels.

Table 1. Commercially available borosilicate glasses

I.D. Number	Nominal B_2O_3, Wt%
7913	3
1720	5
N51A	9.6
SRM93a	12.53
7740	13
7720	15
7050	24
7070	26

b. Measurements of Palladium Thickness in COMSAT Solar Cells

R. F. Fleming

Neutron Activation Analysis was employed to accurately (better than 10%) determine, intact, the effective thickness of palladium (Pd) protection layers (1-100 nm thick) on solar cells. The solar cells are intended for use on INTELSAT V communications satellites being produced by Ford Aerospace and Communications Corporation. The thickness of the Pd film--sandwiched between a titanium (Ti) layer and a silver (Ag) layer--is critical for protection of the Ti film from oxidation and subsequent failure of the cell either through increased resistance of the Ti layer or from peeling of the Ag layer upon exposure to moisture.

The palladium was measured by counting the 88 keV gamma ray from the decay of the 13.46 hour Pd-109 activity using the LEPS detector. The samples along with a standard were irradiated for one hour in the 1.3×10^{13} $n/cm^2/sec$ neutron flux of the RT-4 pneumatic facility. The counting was done after a 12 hour cooling period to allow for the decay of the 2.62 hour Si-31 activity. Four standards of vacuum deposited palladium on silicon substrates were produced. Their thicknesses, which ranged from 100 Å to 1000 Å, were determined by both gravimetric and spectrophotometric analysis at COMSAT.

The NBS measurements were important verifications of the results of destructive analyses (wet chemical and electron probe) of COMSAT laboratories which showed the films to be thinner than the target tolerances. These tests, performed on representative samples of the solar cells, were vital in quality control of batches which potentially could have failed in service on the satellite.

Subsequent to the NBS findings, researches at Ford Motor Company Scientific Laboratories and COMSAT developed the x-ray fluorescence technique to monitor the thickness of the cell coatings. This new approach is similar in principle to that used in the neutron activation technique; however, it does not suffer from the residual radioactivity generated by neutron activation and thus is a non-destructive technique. Standards for these measurements have been cross-calibrated with the neutron activation technique by NBS.

c. The Use of Radiochemical Activation Analysis for the Determination of Platinum in Biological Materials

J. V. Bailey and R. Zeisler

Increased concern over possible growing human body burdens of the noble metals, especially platinum, requires the analytical assay of these elements. Platinum, an element widely used in automotive catlaytic converters, poses a potential threat to humans through its ever increasing environmental concentrations. Another source of body burdens of platinum is the use of platinum compounds in medical treatment. Both effects have yet to be investigated because "normal" concentrations of platinum and possible dangerous body burdens are at extremely low levels; about 1 ng/g for soft wet tissues. Present limits of determination are well above this level with reports of 100 ppb for atomic absorption, 20 ppb for spark source emission, 400 ppb for instrumental neutron activation analysis, and 15 ppb for radiochemical neutron activation analysis.

Radiochemical activation analysis provides the highest potential for lowering the detection limit of platinum in biological materials. Depending on irradiation and counting conditions, an "interference free" limit of detection of less than .1 ng/g (wet weight) can be calculated. The objective of this study is to develop a new radiochemical separation technique to provide "interference free" counting of the activated platinum.

In this study the reaction Pt-198 (n,γ,β^-) Au-199 is utilized. The Au-199 produced in this reaction decays with a half-life of 3.14d under emission of two-one gamma energies of 158.37 keV (76.8%) and 208.20 keV (16.6%). This long half-life allows ample time for chemical separation as well as sufficient time for the decay of high level short lived activities. The radiochemical procedure consists of the wet-ashing of an irradiated sample (200-400mg) and a Pt standard (.1 ml of solution pippetted onto filter paper) followed by the actual chemical separation. The separation is achieved through precipitation of the elemental Au-198 along with 1 mg of Au carrier by reduction with Fe(II). The precipitate is then filtered and counted on a Ge(Li) detector.

Initial radiotracer studies as well as a comparator analysis with Pt-spiked NBS bovine liver show that the radiochemical separation can be carried out quantitatively with a chemical yield of 99-100%. During the same determination, a detection limit of 3ng/g (200mg dry weight) for a 1h irradiation and 5d decay time was estimated after counting the sample for 20,000 seconds. By optimizing the irradiation and counting conditions, the radiochemical procedure can be expected to yield results with a limit of detection lower than 1 ng/g.

d. Determination of Chlorine and Bromine Species in New and Used Petroleum Products

R. Zeisler

Inorganic halogen and halogenated organic compounds in petroleum products have different impacts on the environment and are of great toxicological interest. The evaluation of halogen species in petroleum products will provide important information on the hazards connected with the use of those products and might lead to products with less hazardous compounds.

Though neutron activation analysis (NAA) is a method essentially insensitive to the chemical state of the elements, when combined with chemical separations, NAA can become a powerful tool for the determination of trace element species. The analyses are performed using instrumental NAA for the determination of total chlorine and bromine. Inorganic species are determined by extraction into an aqueous phase and precipitation of the silver halides. The organic bound hydrogen is calculated as the difference: total halogen minus inorganic halogen. It is planned to use specific extraction and chromatographic procedures for the determination of certain species. The feasibilitity of this method is currently being tested. Preliminary results on low halogen-oils (NBS SRM Residual Fuel Oil and re-refined oil) show that the procedure is reproducible.

e. Depth Profiling of He-3, Li-6 and B-10 Using a Thermal Neutron Beam

R. F. Fleming

A joint effort has been undertaken between the Bureau and Sandia Laboratories, Albuquerque, to develop the use of thermal neutron beams to determine the amount and depth profile of helium-3 in metal tritides by means of the He-3 (n,p) H-3 reaction. The metal tritides (MT_2) are stoichiometrically loaded with tritium which undergoes its natural 12 year beat decay to produce the helium-3. These tritides are fabricated as targets for high yield 14-MeV neutron generators used for defense, medical therapy, and analytical purposes. The build-up of the helium-3 and its migration in the tritide may have a significant effect on the long term integrity of the neutron targets.

The work to date has involved surface implants of He-3, Li-6 and B-10 as well as actual tritide targets of both ScT_2 and ErT_2. Figure 1 shows a silicon surface barrier detector spectrum with a 'surface' layer of He-3 on a Sc substrate. The second figure shows the broad proton distribution from the He-3 accumulated in a 1.5 μm thick ErT_2 target. These spectra were obtained using the thermal neutron beam of the Nuclear Physics Facility (BT-7) with Dr. Ivan G. Schroder (532) and Dr. J. M. Harris of Sandia. Improvements to the beam have resulted in a factor of eight increase in the signal-to-noise and a factor of ten in intensity, such that in recent data the broadened triton peak is also apparent above the background for the tritide. Planning has now begun on the construction of a high purity, 10^8 n/cm^2/sec thermal neutron beam dedicated to depth profiling at the BT-3 port of the NBS reactor.

The neutron technique has significant advantages over conventional charged particle methods such as Rutherford backscattering or PIXE, especially for low-Z targets. First, the neutrons uniformly illuminate the entire target depth. Second, since the incident neutron energy is completely negligible compared to the reaction Q-valve, there is no kinematic broadening and the charged particles are produced both monoenergetically and isotropically. The target depth distribution is therefore monotonically

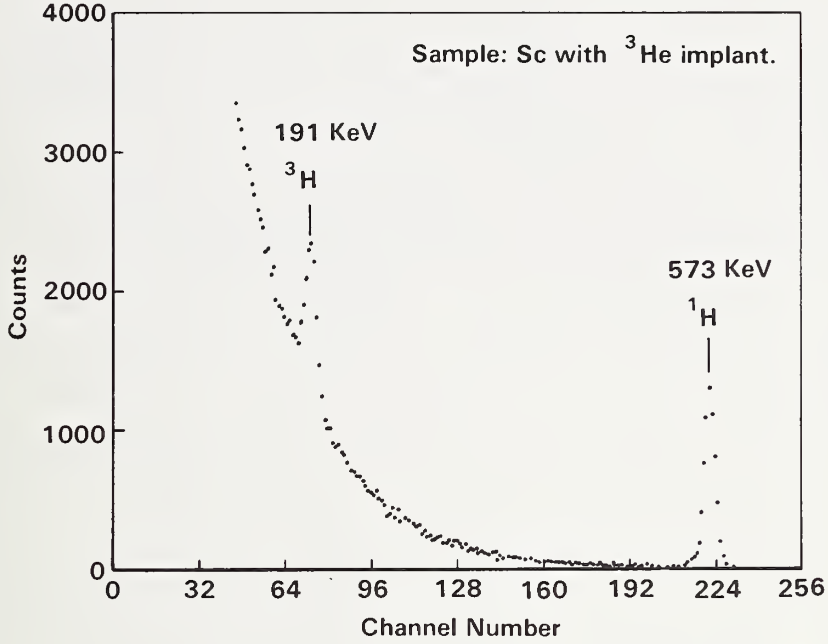

Figure 1. Surface He-3 distribution.

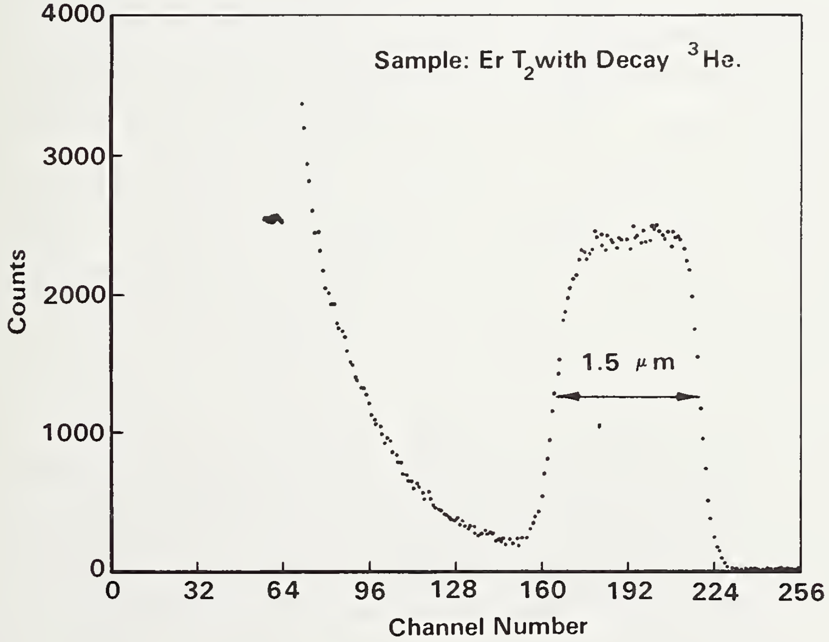

Figure 2. Volume He-3 distribution.

related to the exiting charged particle energy via that particle's stopping power. Depth resolution of the order of 100 Å is possible.

In addition to the NBS-Sandia effort, two other groups have been developing the thermal neutron depth profiling technique. The pioneering work was done by Biersack and Fink[1] using a guide tube at the Grenoble reactor. A second effort is being carried out at the 2 MW reactor at the University of Michigan as the Ph.D. thesis of Mr. William Halsey working under Professors John King and Dietrich Vincent. This work, which is directed toward a metallurgical study of the effect of annealing on helium diffusion in metals, will be completed early in 1980. We have exchanged samples with Halsey and he has visited NBS. The possibility of him coming here to continue profiling work as an NBS post-doctoral worker has been discussed. When completed, the NBS depth profiling beam will be the most powerful such facility in the U. S.

In the table we list the feasible thermal neutron induced charged particle reactions along with a calculated sensitivity based on a count rate of 0.1 cps, a detector solid angle of 1%, and a neutron flux of 10^8. By far the most attractive candidates are He-3, Li-6 and B-10 since they are stable and have large cross sections. We have obtained results for all three reactions. Besides the importance of He-3 in metal tritides, both He-3 and Li-6 depth distributions are of great interest to the thermonuclear fusion community for first-wall reactor design and for diffusion into metals. The distribution of lithium and especially boron in semiconductors is of course of great concern to the electronics community. In fact the recent explosive growth of ion beam depth profiling has been driven primarily by this need. Both Be-7 and Na-22 are of interest because of their huge cross sections even though the targets would be radioactive. (The radioactivity has the advantage, however, of allowing absolute measurement of the number of target atoms by gamma counting.) The study of sodium diffusion into metals and glasses is a long standing problem. The Ni-59 reaction would allow study of nickel diffusion into host metals--the physics of this reaction has already been thoroughly

Table 1. Candidate for thermal neutron depth profiling

Elem.	Reaction	Target Halflife	atoms/mci or (% abun.)	Energy of Emitted Particles (keV)		Cross Section (barns)	Sensitivity (atoms/cm^2)
He	^{3}He(n,p) T	Stable	(.00014)	573	191	5327	2 x 10^{13}
Li	^{6}Li(n,α) T	"	(7.5)	2056	2728	940	1 x 10^{14}
B	^{10}B(n,α)^{7}Li	"	(20)	1473	840	3836	3 x 10^{13}
Be	^{7}Be(n,p)^{7}Li	53 day	2.5 x 10^{14}	1439	206	48000	2 x 10^{12}
Na	^{22}Na(n,p)^{22}Ne	2.6 year	4.4 x 10^{15}	2248	102	36000	3 x 10^{12}
Ni	^{59}Ni(n,α)^{56}Fe	8 x 10^4 yr	1.3 x 10^{20}	4753	340	12	8 x 10^{15}
N	^{14}N(n,p)^{14}C	stable	(99.63)	584	42	1.8	6 x 10^{16}
O	^{17}O(n,α)^{14}C	"	(0.038)	1415	404	0.235	4 x 10^{17}
S	^{33}S(n,α)^{30}Si	"	(0.75)	3081	411	0.14	7 x 10^{17}
Cl	^{35}Cl(n,p)^{35}S	"	(75.77)	598	17	0.49	2 x 10^{17}
K	^{40}K(n,p)^{40}Ar	"	(0.012)	2231	56	4.4	2 x 10^{16}

Sensitivity based on: 0.1 cps, 1% solid angle, 10^8n/cm^2/sec flux investigated at BT-7. The reactions with N, O, S, Cl and K would be suitable for depth profiling only for matrices in which they are a major constituent.

It should be pointed out that neutron induced depth profiling is a complementary technique to the nuclear track method, developed as an analytical tool at NBS by B. S. Carpenter. The track technique provides a real distributions, but little information on particle energy or depth. Depth profiling provides detailed depth distributions averaged over the area of the sample.

f. Neutron-Capture Prompt Gamma-Ray Activation Analysis

G. E. Gordon, W. H. Zoller, W. B. Walters, D. L. Anderson,
M. P. Failey (University of Maryland, College Park, MD)
R. M. Lindstrom

A facility for performing neutron-capture prompt γ-ray activation analysis (PGAA) has been developed at the NBS reactor to the stage at which concentration of many elements (from the set: H, B, C, N, F, Na, Mg, Al, Si, P, S, Cl, K, Ca, Ti, V, Cr, Mn, Fe, Sr, Cd, Ba, Nd, Sm, and Gd) have been measured in a wide variety of samples. The analytical capabilities of the PGAA instrument have been improved with the addition of a new, well-shielded upper beam tube and with the operation of a large, split-annulus NaI crystal surrounding a Ge(Li) detector for Compton-suppression and pair spectrometry. The PDP-11/34-based pulse-height analyzer is now capable of acquiring singles and Compton-suppressed spectra over the energy range of 0.06 to 11.0 MeV and a pair spectrum (3.5 - 10.0 MeV) for each sample.

The neutron beam ($\phi_{nth} = 2 \times 10^8$ n/cm^2-sec) has a usable diameter of 3 cm at the sampling position and the flux in this area is constant with radial distance to ±3%. Samples ranging in mass from 0.05 to 2.5 g are packaged in Teflon, polyethylene, or mylar bags or vials. A Cr monitor is run regularly at the sampling position to check for flux variations or changes in the detector response.

Several NBS Standard Reference Materials (SRMs) have been analyzed to check the reliability of the method. The results are compared to the certified and other literature values in tables I-III. Also presented in table IV-VIII are the analyses of several U.S.G.S. standard rock samples. In general, PGAA has been found to be extremely useful in evaluating many types of samples for major and trace elements.

A more complete description of the system and its analytical capabilities is given in two major papers, one emphasizing the analytical uses which has been published and the second, emphasizing the instrumentation, which will be submitted soon for publication.

Table I. Concentrations of Elements in Standard Orchard Leaves and Bovine Liver (μg/g unless % indicated)[a]

Element	SRM 1571 Orchard Leaves			SRM 1577 Bovine Liver		
	This Work	NBS	Other Values	This Work	NBS	Other Values
H (%)	5.54±0.08	-	6.1±0.1	6.8±0.3	-	7.0±0.1
B	33.2±0.1	33±3	33±2, 23.7-38	3.2±0.2	-	-
C (%)	46±2	-	47±5, 45.8±1.3	52±2	-	51±2. 49.6±1.5
N (%)	2.70±0.09	2.76±0.05	2.5-2.86, 2.7±0.4, 2.76	10.35±0.30	10.6±0.6	10.4±0.8, 10.6
Na	-	82±6	71-90	3100±600	2430±130	2000±2670
Mg (%)	0.63±0.07	0.62±0.02	0.40-0.71	-	-	0.060-0.061
S (%)	0.17±0.02	(0.19)	0.23±0.02	0.72±0.02	-	0.72±0.04
Cl	730±30	(700)	790	3000±100	(2600)	2542±300
K (%)	1.49±0.04	1.47±0.03	1.11-1.62	1.00±0.03	0.97±0.06	0.756-0.99
Ca (%)	2.13±0.11	2.09±0.03	2.052-2.125	-	-	0.0117-0.0125
Mn	98±20	91±4	52-144	13±6	10.3±1.0	9.1-28
Cd	-	0.11±0.02	<0.1-0.45	0.27±0.06	0.27±0.04	<0.1-0.35
Sm	0.11±0.03	-	-	-	-	-

[a] Based on five separate irradiations.

Table II. Concentrations of Elements in Standard Fly Ashes (μg/g unless % indicated)[a]

Element	SRM 1633			SRM 1633a
	This work	NBS	Other values	This work
B	433±4	-	434±9, 493±14, 500±29	39.2±0.7
Na (%)	0.30±0.02	-	0.32±0.04, 0.283±0.014, 0.36	0.21±0.06
Mg (%)	1.5±0.2	-	1.8±0.4, 1.78±0.20, 2.4	-
Al (%)	12.6±0.2	-	12.7±0.5, 12.35±0.25, 12.3	14.0±0.2
Si (%)	21.8±0.3	-	21±2, 17.7, 17	22.2±0.4
P (%)	-	-	0.3, 0.088	1.5±0.2
S (%)	0.39±0.04	-	0.44±0.07	0.27±0.02
K (%)	1.76±0.05	(1.72)	1.61±0.15, 1.80±0.13, 1.69, 1.75	1.97±0.04
Ca (%)	4.75±0.08	-	4.7±0.6, 4.69±0.14, 3.8	1.29±0.11
Ti (%)	0.72±0.02	-	0.74±0.03, 0.70±0.03, 0.696	0.84±0.01
V	190±50	214±8	235±13, 237±20	360±40
Mn	480±25	493±7	496±19, 488±14	190±15
Fe (%)	6.1±0.1	-	6.2±0.3, 6.7	9.7±0.2
Cd	1.50±0.07	1.45±0.06	1.6±0.2	1.07±0.05
Nd	62.1±2.4	-	57.8±1.6, 81	65.6±5.4
Sm	12.1±0.4	-	12.4±0.9, 11.4±1.6	16.0±0.2
Gd	11.4±0.2	-	-	15.3±0.2

[a] Based on five separate irradiations.

Table III. Concentrations of Elements in NBS Standard Coals ($\mu g/g$ unless % indicated)[a]

Element	SRM 1632 (old coal standard)			SRM 1632a (Bituminous)			SRM 1635 (Subbituminous)		
	This work	NBS	Other values	This work	NBS	Other values	This work	NBS	Other values
H (%)	4.02±0.05	-	4.3±0.1	3.7±0.1	-	-	3.96±0.03	-	-
B	42.1±0.7	-	47.0±1.6, 30±1, 43	52.7±1.8	-	-	104.5±2.6	-	-
C (%)	70±5	-	73±3, 69.6±2.1	71±4	-	-	59±3	-	-
N (%)	1.3±0.2	-	2.2±0.4	1.27±0.08	-	-	1.0±0.1	-	-
Na	-	-	414±20	-	-	850±45	2700±50	-	2440±200
Al (%)	1.68±0.04	-	1.85±0.13, 1.74±0.04	3.01±0.13	(3.07)	2.91±0.32	0.34±0.04	(0.32)	0.30±0.02
Si (%)	2.95±0.06	(3.2)	3.92	5.8±0.1	-	-	0.52±0.02	-	0.56±0.07
S (%)	1.29±0.03	-	1.32±0.07	1.59±0.02	(1.64)	1.8±0.4	0.32±0.01	(0.33)	-
Cl	895±15	-	890±125, 844±35	784±17	-	780±40	26±2	-	26±4
K (%)	0.275±0.010	-	0.28±0.03, 0.30±0.02	0.42±0.02	-	0.42±0.02	0.0097±0.0006	-	0.0117±0.0015
Ca (%)	0.33±0.05	-	0.43±0.05, 0.35±0.03	0.24±0.02	-	0.24±0.02	0.54±0.02	-	0.55±0.08
Ti	890±35	(800)	1100±100, 890±50	1550±40	(1750)	1620±70	190±20	(200)	205±20
Mn	43.5±2.4	40±3	43±4, 41±4	29±5	28±2	32±3	24±7	21.4±1.5	22±3
Fe (%)	0.842±0.024	0.87±0.03	0.84±0.04	1.11±0.02	1.11±0.02	1.15±0.03	0.22±0.01	0.239±0.005	0.22±0.02
Cd	0.18±0.02	0.19±0.03	0.2±0.05	0.21±0.03	0.17±0.02	-	-	0.03±0.01	-
Nd	11.3±2.0	-	8.7±1.0, 10±7	11.8±0.4	-	12±3	-	-	1.4±0.2
Sm	1.53±0.02	-	1.7±0.2, 1.38±0.10	2.10±0.07	-	-	0.25±0.01	-	-
Gd	1.43±0.05	-	-	1.95±0.03	-	-	0.23±0.01	-	-

Table IV

Concentrations of Elements Observed in U.S.G.S. Rock Samples

(μg/g unless % indicated)

Element	AGV-1[a]			
	This Work	U.S.G.S.[b]	Other Values	
H	690±50	2060	-	
B	5.9±0.1	[5]	3.9±0.7	
Na (%)	2.82±0.17	3.16	3.15±0.15	3.10
Mg (%)	0.94±0.07	(0.923)	1.02	
Al (%)	9.03±0.09	(9.13)	8.83	
Si (%)	27.4±0.6	27.6	28.2	
P (%)	-	0.21	0.30	
Cl	119±12	[110]	-	
K (%)	2.30±0.10	(2.40)	2.2±0.9	2.47
Ca (%)	3.44±0.04	(3.50)	3.79	
Ti (%)	0.597±0.012	(0.619)	0.60	
V	78±9	(125)	-	
Mn	741±8	763	640±30	
Fe (%)	4.36±0.17	4.73	4.3±0.2	4.65
Sr	-	657	-	
Cd	0.07±0.03	[0.09]	-	
Ba	-	1208	1180±100	
Nd	16±2	(39)	-	
Sm	5.3±0.2	(5.9)	5.4±0.5	
Gd	3.67±0.03	[5.5]	-	

[a] Based on a single irradiation

[b] Values without parentheses are recommended. Values with parentheses are averages. Values with brackets are magnitude.

Table V

Concentrations of Elements Observed in U.S.G.S. Rock Samples

(μg/g unless % indicated)

Element	PCC-1[a]		
	This Work	U.S.G.S.[b]	Other Values
H (%)	0.557±0.005	0.582	-
B	1.4±0.1	[6]	-
Na	-	[400]	430
Mg (%)	25.6±0.9	(26.0)	27.4
Al (%)	0.38±0.02	(0.39)	0.38
Si (%)	19.3±0.8	19.6	19.6
P	-	[90]	80
Cl	76±14	[60]	-
K	-	[300]	-
Ca (%)	0.38±0.03	(0.36)	0.365
Ti	240±30	[900]	910
V	21±7	(30)	-
Cr	3090±100	(2730)	-
Mn	920±30	(959)	-
Fe (%)	5.61±0.18	(5.84)	5.55
Cd	-	[0.1]	-
Nd	-	-	-
Sm	0.04±0.02	(<0.18)	-
Gd	-	-	-

[a] Based on a single irradiation

[b] Values without parentheses are recommended. Values with parentheses are averages. Values with brackets are magnitude.

Table VI

Concentrations of Elements Observed in U.S.G.S. Rock Samples (μg/g unless % indicated)

Element	G-2[a]			
	This Work	U.S.G.S.[b]	Other Values	
H	620±60	(739)	-	
B	2.6±0.1	[2]	3.9±0.7	
Na (%)	2.61±0.12	(3.02)	2.95±0.05	3.55
Mg (%)	0.38±0.08	(0.46)	0.63	
Al (%)	8.08±0.04	(8.12)	8.51	
Si (%)	30.9±0.8	32.3	32.1	
P (%)	-	0.061	0.080	
Cl	41±10	[50]	-	
K (%)	3.67±0.13	3.74	4.0±0.5	2.96
Ca (%)	1.35±0.08	(1.39)	1.02	
Ti	2640±40	(2780)	3200	
V	34±10	(35.4)	-	
Mn	230±30	(260)	212±14	
Fe (%)	1.86±0.14	(1.85)	1.72±0.5	1.81
Sr	600±200	479	-	
Cd	0.023±0.011	(0.039)	-	
Ba	2000±800	1870	1800±70	
Nd	39±6	(60)	-	
Sm	6.71±0.33	(7.3)	8.7±0.5	
Gd	3.20±0.03	[5]	-	

[a] Based on a single irradiation.

[b] Values without parentheses are recommended. Values with parentheses are averages. Values with brackets are magnitudes.

Table VII

Concentrations of Elements Observed in U.S.G.S. Rock Samples (μg/g unless % indicated)

Element	GSP-1[a]			
	This Work	U.S.G.S.[b]	Other Values	
H	780±50	(772)	-	
B	0.7±0.2	(<3)	0.08±0.06	
Na (%)	2.09±0.04	2.08	2.1±0.2	2.22
Mg (%)	0.62±0.12	0.58	0.60	
Al (%)	7.94±0.08	(8.07)	8.01	
Si (%)	30.4±0.8	31.5	31.8	
P (%)	-	0.12	0.10	
Cl	270±20	[300]	-	
K (%)	4.44±0.11	4.59	4.5±0.6	4.36
Ca (%)	1.51±0.07	1.44	1.50	
Ti	3830±30	(3990)	6900	
V	70±20	52.9	-	
Mn	330±70	325	264±16	
Fe (%)	2.88±0.16	3.03	2.8±0.1	2.92
Sr	-	233	-	
Cd	-	[0.06]	-	
Ba	-	1300	1110±50	
Nd	185±10	(188)	-	
Sm	24.0±0.3	(27.1)	23.2±1.0	
Gd	9.64±0.09	[15]	-	

[a] Based on a single irradiation.

[b] Values without parentheses are recommended. Values with parentheses are averages. Values with brackets are magnitudes.

Table VIII

Concentrations of Elements Observed in U.S.G.S. Rock Samples
(µg/g unless % indicated)

Element	RGM-1[a]		QLO-1[b]	
	This Work	U.S.G.S.	This Work	U.S.G.S.
H	840±40	-	540±50	-
B	26.5±0.4	30.0	33.3±0.5	41.0
Na (%)	2.82±0.11	-	2.73±0.12	-
Mg (%)	0.79±0.11	-	0.97±0.12	-
Al (%)	7.33±0.05	-	8.52±0.13	-
Si (%)	33.1±0.7	-	29.7±0.5	-
Cl	525±30	440	220±20	192
K (%)	3.45±0.11	-	2.84±0.13	-
Ca (%)	0.75±0.06	-	2.17±0.07	-
Ti	1460±20	-	3430±15	-
V	13±6	15	30±15	62
Mn	270±15	270	650±20	672
Fe	1.32±0.07	-	2.86±0.07	-
Cd	0.06±0.02	-	-	-
Nd	18±2	19	17±2	35
Sm	3.72±0.05	-	4.19±0.08	-
Gd	3.06±0.06	-	3.57±0.05	-

[a] Based on two irradiations.

[b] Based on a single irradiation.

2. Activities in Major NBS Programs

a. The National Environmental Specimen Bank (NESB)

S. Harrison and R. Zeisler

For the past three years the U.S. National Bureau of Standards has been cooperating with the U. S. Environmental Protection Agency in studies which anticipate the establishment of a sample archiving system known as the National Environmental Specimen Bank. Currently, the Activation Analysis Group is involved in setting up a Pilot Specimen Bank which will serve to evaluate the feasibility of a national specimen archiving program and to determine the optimum sampling and storage procedures necessary for obtaining long term stored samples valid for both inorganic and organic trace constituents.

Progress this year was highlighted by the construction of the clean room facility for sample storage. As sample collection is scheduled to begin in early FY 80, research this year has been concerned primarily with procedures and evaluation of materials for sample collection.

1. The Storage Facility

The clean room storage facility is in the final construction stages and will be operational by the end of FY 79. The facility consists of a Class 100 clean laboratory which is subdivided into inorganic and organic working areas. In addition to work benches, clean air working modules and a fume hood, the clean laboratory will contain a biohazard hood for handling human tissue samples and a microwave oven for processing biologically contaminated material before disposal. The adjacent clean storage room will be a low humidity area. It will house three liquid nitrogen (LN_2) freezers (storage from 77 K to 150 K) and four upright freezers (storage at 188 K and at 250 K) with LN_2 backup system. Both types of freezers are equipped with audible alarms alerting personnel at loss of temperature or power. This equipment will make possible a comparison study of long term storage of specimen bank samples at a variety of temperatures.

2. Research for Sample Collection, Storage and Analysis

The Activation Analysis Group has been involved with the development and evaluation of certain materials called for in the rigorous sampling protocol to be used by pathologists at autopsy. One of these is a titanium-Teflon knife to take the place of an autopsy knife and/or stainless steel scalpel customarily employed. A prototype of this knife is currently being used at the University of Maryland Hospital with good reports as to its ease of use by a pathologist. Commercial pure water has been analyzed for trace elements and has been found to contain contaminant levels sufficiently low as to allow its use as rinse water in the sample collection procedure. Samples of the FEP Teflon film manufactured into sheets and bags are currently being evaluated for surface and leachable trace element impurities as are non-talced, pre-cleaned, sterile gloves to be worn by pathologists and technicians. The Teflon PFA jars to be used for sample storage are also being studied for any contribution to sample contamination.

A method for homogenizing frozen tissue samples (they will be received from the collecting hospitals at approximately liquid nitrogen temperature) was described by Iyengar, et al.[1] This method, the brittle fracture technique, pulverizes a sample using a ball inside a cylindrical container and mechanically shaking. The fracturing chamber and sample are frozen to LN_2 temperature before shaking.

A machine for brittle fracturing liver samples has been built at NBS. In this case the chamber and ball were machined out of solid Teflon. A system designed for handling samples up to 60g size was constructed and used successfully. However, we will be receiving a 1/2 left lobe of human liver which weighs about 250g. Therefore, a much larger chamber and ball were constructed to accommodate this large sample in one piece. Due to the greatly increased weight of the larger chamber, there have been problems getting the shaker to operate satisfactorily. It is anticipated that modification of the shaker will solve this problem. Brittle fracture should provide a way of homogenizing samples without defrosting them and with a minimum chance for inorganic or organic contamination.

Work in analytical methodology has concentrated on increasing sensitivity and developing methods to cover the first priority elements established by NBS and EPA. A preirradiation separation for V is being studied as well as a radiochemical separation for Pt and Au. The multi-element radiochemical procedure described in last year's summary (NBS Technical Note 995) has been successfully applied to a variety of biological SRM matrices. It will be used for liver sample analyses in FY 80.

---

1. Iyengar, G. and Kasperek, K., *J. Radioanal. Chem.*, p. 301-315 (1977).

b. Evaluation of Reactor Track-Etch Power Monitor

B. S. Carpenter, L. J. Pilione, I. G. Schroder
J. W. Roe (Nuclear Regulatory Commission, Washington, DC)
S. Sanatani (International Atomic Energy Agency, Vienna, Austria)

General Description of the Track-Etch Monitor

The National Bureau of Standards was requested by the International Atomic Energy Agency through ISPO to evaluate the capability of the Track-Etch Monitor[1,2] for providing an independent record of reactor power by conducting field tests under very well defined experimental conditions. The Track-Etch Monitor was designed by G. E. Vallecitos Nuclear Center to operate unattended in a neutron field to provide an independent permanent record of the periods of reactor operation and shut-down, and in addition, to provide information concerning the neutron energy spectrum.

The track-etch monitor is an externally-powered device designed to record the neutron flux from operating reactors and other sources for extended periods of time. A strip of 35 mm wide polymer tape is driven past a group of six fissionable desposits which are exposed to the local neutron flux table 1. A given fraction of the fission fragments generated penetrate the tape producing radiation damaged tracks that are subsequently etched and counted to permit a reconstruction of the temporal flux history to which the monitor was exposed. The monitor is equipped with enough tape to cover a year's operation. Under these conditions the monitor is designed to operate at a neutron flux of 10^6 n cm^{-2}s^{-1}.

The monitor was designed to fit within the ion chamber thimbles normally used by power reactors for detector monitors. It is contained within a sealed aluminum can of two different sizes, 8.4 cm in diameter and 26 cm long or 10.2 cm in diameter and 26 cm long. The total weight is approximately 1.2 kg or 1.5 kg, respectively. There is an eye-bolt located at the end opposite the fission sources for insertion and retrieval. Power is supplied to the monitor from an external source through a sealed electrical connector. The synchronous motor within the monitor uses either 115 V or 240 V AC for operation and drives the take-up reel for the 35 mm film at the speed of 4.75 cm per day. In addition a microswitch is placed on the drive sprocket of the feed reel to allow remote indication of proper film transport operation.

In order to test the monitor under a controlled and known neutron environment a monitor was installed in the Nuclear Detector Well #2 of the 10MW NBS Research Reactor. At this position the monitor was exposed to a neutron flux of 1×10^{6} n $cm^{-2}sec^{-1}$ and a gamma dose of 500 R/hr. The monitor remained in this position for 56 days and during this time the NBS reactor cycled through six start-ups and shut-downs. Following the removal of the monitor from the reactor, the exposed tape, 2.69 m in length, was processed (etched) and studied at NBS. The track densities were counted manually using an optical transmission microscope and the optical densities were measured with the aid of an image analyzing microscope. The variation in both track density and optical density show an exact correlation with the reactor power output as determined by the monitors in the NBS Reactor control room.

Additional tests and evaluation of the monitors in known neutron fields have been made in order to determine the monitor's response to field changes. Some of these tests have been conducted with a highly thermal neutron beam from one of the NBS Reactor beam tubes. The monitor was placed in the beam and the intensity of the beam recorded with a fission chamber. The beam intensity was then changed by means of lead attenuators for fixed periods of time. The tape was removed from the monitor and etched.

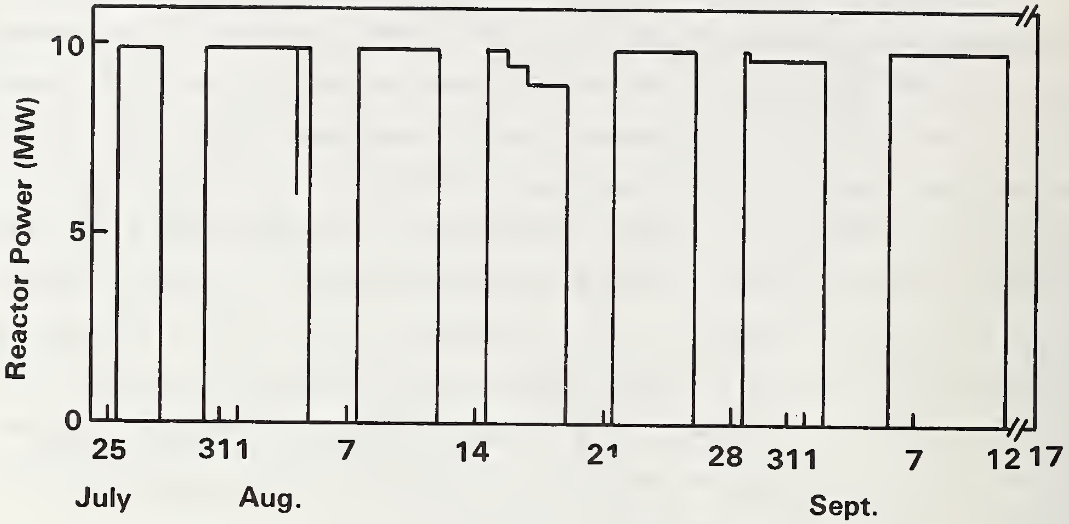

Figure 1. NBSR power history 25 July-17 September, 1978.

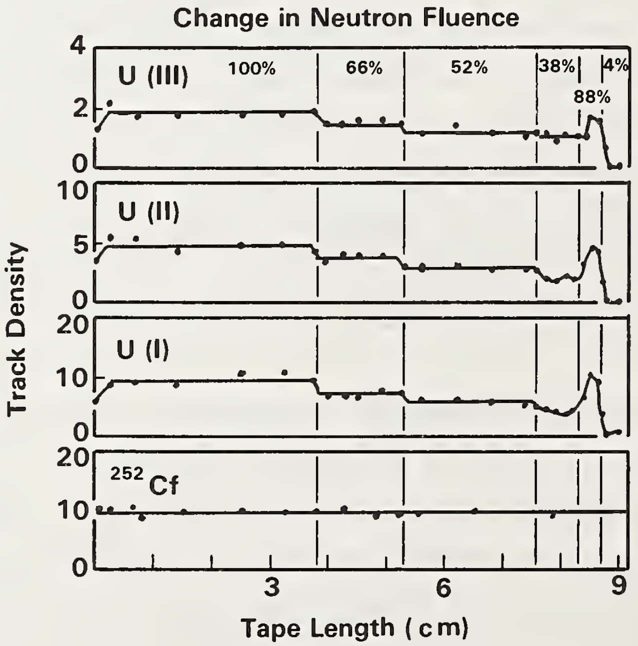

Figure 2. Test of track etch power monitor in NBSR in BT-7 position with reactor power at 9.01 MW and monitor tape speed 45.1 mm d^{-1}.

The track densities in the three U-235 channels and Cf-252 channel were counted along the length of the tape and the variations in track densities matched exactly the changes in neutron measured with the fission chamber (Figure 2). A similar study is underway using a Cf-252 neutron source, to relate the track density of the U-238 and Np-237 channels to changes in neutron intensity.

Finally, field testing of the monitor in operating nuclear power facilities is underway to provide archival records of these facilities power history. The data gathered from both the field test and the studies made at the NBS Research Reactor will be used in evaluating the overall potential of the Track-Etch Monitor for Reactor Safeguards use.

---

1. Fleischer, R. L, Price, P. B. and Walker, R. M., *Nuclear Tracks in Solids: Principles and Applications, University of California Press,* (1975).

2. Weidenbaum, R., Lovett, D. B. and Kosanke, H. D., *American Nuclear Society Transactions,* 13, p. 524-526, (1970).

c. Analysis of Chesapeake Bay Water by Neutron Activation Analysis with Pre-Irradiation Chemistry

Robert R. Greenberg

The accurate analysis of trace elements in seawater is often complicated by the presence of large amounts of alkali metals, alkali earths and halides. A separation procedure based on the use of Chelex 100 resin has been developed by Kingston et al.[1] to concentrate and separate various elements of interest from a seawater matrix. Several groups in the Inorganic Analytical Research Division are currently involved in a joint project to analyze water samples from the Chesapeake Bay. As part of this project, Neutron Activation Analysis coupled with the Chelex 100 pre-irradiation separation will be used. A preliminary analysis of two aliquots of a large Chesapeake Bay Water sample has been completed, and the results obtained are compared in table 1 with those obtained by graphite furnace atomic spectrometry analysis of the same sample. Both sets of values agree within the listed uncertainties.

Table 1. Comparison of elemental concentrations determined in a Chesapeake Bay water sample by neutron activation analysis and graphite furnace atomic absorption spectrometry

Element	NAA	GFAAS
Co	0.07± 0.01	≤0.1
Cu	1.8± 0.3	2.0± 0.1
Fe	1.9± 0.5	2.1± 0.5
La	0.10± 0.01	
Mn	1.9± 0.1	2.0± 0.1
Sc	0.0006± 0.0002	
V	0.44± 0.02	
Zn	4.8± 0.5	4.8± 0.3

---

1. H. M. Kingston, I. L. Barnes, T. J. Brady, T. C. Rains and M. A. Champ, *Anal. Chem. 50*, 2064 (1978).

3. Certification Analysis of Standard Reference Materials

a. Analysis of SRM 1643a Trace Elements in Water

R. Zeisler, R. R. Greenberg, T. E. Gills

The following nuclear activation techniques have been applied to the certification analysis: instrumental neutron activation analysis (INAA), radiochemical neutron activation analysis (RNAA) and instrumental photon activation analysis (PAA). Results are presented in table 1 on 18 trace elements. Though for many elements, different techniques and procedures have been used, the results-which are in agreement amont the procedures-represent the method which yields the lowest error.

Table 1. Results of the analysis of SRM 1643a obtained by selected NAA procedures

Element	NAA Procedure	Number of Determinations	Concentration (ng/mL) $\bar{x}$ ± 1s	Relative Error %
Al	INAA	18	123.4 ± 3.9	3.2
V	INAA	18	52.5 ± 2.4	4.6
Cr	RNAA	6	19.8 ± 1.5	7.9
Mn	INAA	6	34.1 ± 0.6	1.7
Fe	INAA-Preconcentration	6	91 ± 8	8.8
Co	INAA-Preconcentration	6	16.61 ± 0.6	3.9
Ni	PAA	6	53 ± 4	8.2
Cu	RNAA	8	20.1 ± 0.5	2.5
Zn	INAA-Preconcentration	6	71.2 ± 3.7	5.2
As	RNAA	8	87.6 ± 2.9	3.3
Se	INAA-Preconcentration	6	10.5 ± 0.4	3.8
Sr	RNAA-Preconcentration	4	241.1 ± 2.7	1.1
Mo	RNAA	7	94.1 ± 3.7	3.9
Ag	INAA-Preconcentration	6	2.90 ± 0.10	3.4
Cd	RNAA	5	11.07 ± 0.18	1.6
Ba	RNAA	4	46.2 ± 0.6	1.3
Hg	INAA-Preconcentration	6	2.3*	
Pb	PAA	6	29 ± 4	13

*Errors in mercury determination 50% rel. due to blank value

b. Analysis of Estuarine Sediment SRM 1646

Robert R. Greenberg and Thomas E. Gills

A new Standard Reference Material, Estuarine Sediment (SRM 1646) has recently been prepared to help meet the needs of the analytical community. This material has been analyzed by both radiochemical and instrumental neutron activation analysis. A summary of the concentration of 16 elements is listed in table 1.

Table 1. Elemental Concentrations Observed in Estuarine Sediment SRM 1646

	Concentration - μg/g unless % indicated	
Element	INAA	RNAA
As		11.2 ± 0.8*
Cd		0.38 ± 0.04
Ce	79 ± 4	
Co	10.13 ± 0.16	
Cr	76.4 ± 2.0	
Cs	3.64 ± 0.15	
Cu		17.1 ± 0.6
Eu	1.46 ± 0.04	
Fe (%)	3.32 ± 0.05	
Hg		0.055 ± 0.004
Mn	373 ± 14	
Rb	85 ± 4	
Sb	0.43 ± 0.05	
Sc	10.7 ± 0.2	
Th	9.9 ± 0.7	
Zn	125 ± 19	

---

*Uncertainties are 2s

c. Radiochemical Analysis of New Fly Ash-SRM 1633a

Robert R. Greenberg and Thomas E. Gills

As part of the SRM recertification program, the new Fly Ash Standard Reference Material (SRM 1633a) has been analyzed by radiochemical neutron activation analysis (RNAA) for 5 elements: As, Cd, Cu, Sb and Se. The concentrations observed are compared with those observed instrumentally in table 1.

Table 1. Comparison of Elemental Concentrations Determined in the New Fly Ash SRM 1633a by Radiochemical and Instrumental Neutron Activation Analysis

	Concentration - μg/g	
Element	RNAA	INAA
As	152 ± 16*	146 ± 12
Cd	1.06 ± 0.16	
Cu	0.21 ± 6	
Sb	6.1 ± 1.2	6.8 ± 0.4
Se	11 ± 2	10.9 ± 1.2

---

*Uncertainties are 2s

d. Determination of Hafnium in Zirconium and Zircalloy SRMs

G. J. Lutz

A series of eight zirconium and zircalloy SRMs has been analyzed for hafnium using instrumental neutron activation analysis. Standards were prepared by pipetting solutions of known concentrations of hafnium onto filter paper which was then dried. These were irradiated along with samples of approximately 200 mg mass for two hours in RT-4 of the NBS reactor. After several weeks decay, samples and standards were counted with a Ge(Li) detector. Values obtained are given in table 1.

Table 1 Hafnium in Zirconium and Zircalloy SRMs

Values are ppm

		Average and Std. Dev.
C1 + D1	191, 196, 193, 192	193 ± 2
I1 + J1	91, 96, 93	93 ± 3
K1 + L5	74, 76, 76	75 ± 1
A1 + B3	44, 43, 43	43 ± 1
G1 + H5	175, 176, 172, 176	175 ± 2
E1 + F3	31, 30, 29, 29	30 ± 1
360a	73, 71, 72, 76	73 ± 2
1210	80, 77, 80	79 ± 2

e. A comparison of the NBS Oyster Standard Reference Material (1566) with the IAEA Oyster Homogenate (MA-M-1)

Thomas E. Gills and Robert Greenberg

The development of the NBS Oyster Standard Reference Material is the first marine standard certified by the National Bureau of Standards for trace elements. Oysters being an accumulation of trace substances from its environment makes it a very valuable indicator of certain pollutants or pollution burdens on the acquatic egosystem.

By contrast, the International Laboratory of Marine Radioactivity in Monaco has developed an oyster homogenate (MA-M-1) for inter-calibration for trace elemental analysis. During certification of the NBS Standard (1566), the IAEA Oyster Homogenate was concurrently analyzed and a comparison was made of both the concentration found and the homogeneity of the NBS and IAEA standards. Because the IAEA material has been depleted, the analysis of the available NBS standard should provide useful information to the international calibration exercise. Both materials were analyzed by neutron activation analysis. By analyzing both materials simultaneously, a comparison could be made of any differences in the levels of trace elements and of the accuracy and precision of the NBS values versus the Round Robin data conducted by IAEA. A table of the results of both Standard Materials are given in table 1.

Table I

	NBS Oyster (SRM 1566) ng/g	IAEA Oyster (MA-M-1) ng/g
Arsenic	13.75 ± .42[1]	13.62 ± .48
Bromine	55.3 ± 1.3	not determined
Cobalt	.32 ± .01	.36 ± .01
Copper	63 ± 2	362 ± 16
Chromium	.48 ± .05	.40 ± .15
Cadmium	3.59 ± .16	2.5 ± 0.2
Iron	199 ± 13	292 ± 9
Mercury	.062 ± .006	.20 ± .02
Rubidium	4.65 ± .32	5.08 ± .26
Selenium	2.17 ± .09	1.97 ± .08
Zinc	850 ± 30	2762 ± 65

[1] Errors expressed as the average standard deviation at 1 sigma.

f. Determination of Aluminum in SRM 16332 Fly Ash

R. M. Lindstrom

In an effort to resolve discrepancies among three chemical determinations of Al in the new Fly Ash SRM, instrumental neutron activation was used. Samples of nominally 100 mg were irradiated for 60 sec in the RT5 rabbit facility of the NBSR and counted twice for 300 sec on a large Ge(Li) detector. When corrections were made for pulse pileup the results of the two counts agreed as well as counting statistics would predict (below 1% s.d.). Intersample variations were a factor of three larger. The results are given in table 1.

As a check on the accuracy of the determination, a sample of SRM 1633, the previous Fly Ash was analyzed in parallel by the same procedure. The concentration found was 12.47 ± 0.34 (s.d.) percent. While aluminum is not certified in this material, the mean of three laboratories reported by Ondov et al. (Anal. Chem. 47, 1102 (1975) is 12.7 ± 0.5 (s.d.) percent.

While the precision and apparent accuracy of this measurement are adequate for SRM certification, it appears possible that instrumental neutron activation analysis can be used to determine an element which dominates the gamma-ray spectrum with better accuracy, possibly approaching the precision limit set by counting statistics at well below 0.1%. If this can be demonstrated, then it may be concluded that neutron activation can be considered an absolute referee method of analysis in favorable cases.

Table 1. Aluminum found, percent

Sample No.	Count 1	Count 2	Count 3
1	14.03 ± 0.08	13.78 ± 0.13	
2	14.29 ± 0.08	14.46 ± 0.12	
3	13.56 ± 0.07	13.87 ± 0.10	14.07 ± 0.16
4	14.10 ± 0.07		
5	13.77 ± 0.07	13.86 ± 0.11	
6	14.68 ± 0.08	14.36 ± 0.13	

Unweighted mean 14.07 % Al
Standard deviation 0.33 % Al, n=12

4. Non NBS Programs

a. The Analysis of Ancient Middle Eastern Ceramics by Instrumental Neutron Activation

M. J. Blackman

One hundred and sixteen ceramic and unfired clay object samples from late 4th and early 3rd Millenia Banesh levels at the archaeological site of Tal-e Malyan, Iran were analyzed for 19 elements by instrumental neutron activation. The objective of the study was to investigate, through trace and minor element profiling, the production and distribution of ceramic products in the context of a developing urban center.

The unfired clay objects were chosen as representative of the local alluvial clays in the immediate area of the site. The ceramics sample included both chaff tempered and grit tempered wares. Within each temper group further subdivisions were made based on form and decoration. The ceramics and clay objects were all from stratagraphic context in the two major Banesh excavations, TUV and ABC, at Fal-e Malyan. Analysis was also carried out on samples of the grit temper to assess the temper contribution to the overall elemental concentrations.

Three distinct chemical groups were detectable within the ceramic sample. The elemental concentration means and standard deviations for these groups and for the clay object samples are presented in table 1. Multivariate statistical analysis of the chemically defined groups confirmed their validiry. No sample assigned to a group showed a greater than 5% probability of membership in another group. The influence of temper inclusion in the sample was also rejected as a possible source of the chemical group differences noted.

When the chemical group membership and ceramic ware type were compared, several patterns of clay utilization were immediately evident. As can be seen in table 2, all chaff tempered ceramics were made from Group I clays, while the grit tempered ceramics made predominately from Group II and III clays. Group I clay closely resembles the clay objects in elemental concentrations and it is likely that the chaff tempered wares were made from the locally available alluvial clay. The grit tempered ceramics show little use of Group I clay, probably due to the high calcium carbonate content of this clay. Grit tempered ceramics are high fired, in excess of 900°C, and a high carbonate content would be unacceptable. The carbonate content would not be a factor in the low fired, less than 600°C, chaff tempered ceramics. The sources of Group II and III clay remains unknown, but are probably located in the mountains surrounding the Kur River Basin where Tal-e Malyan is located.

Group II clay was apparently favored over Group III clay for a wider variety of forms and decorative motifs. This preference does not seem to arise from physical or esthetic properties of the two clays, nor from chronological shifts in clay source use. The difference in use of Group II and III clays can best be explained at present, by multiple ceramic production sites with access restricted to a single clay source at any given site. Further distribution of the products of ceramic manufacture seem to favor the site(s) with access to Group II clay.

Although no evidence of ceramic production has been detected at Tal-e Malyan during the Banesh Period, the low fired, chaff tempered wares could have been produced at the site. The high fired, grit tempered wares, however, were probably produced elsewhere in the Kur River Basin and redistributed to Tal-e Malyan. Further research is planned on material from known and assumed production sites to attempt to identify the source of the grit tempered wares.

Table 1. Concentration means for banesh ceramic samples and clay objects

	Clay Objects (15)#			Group I (50)			Group II (35)			Group III (16)		
Element	Mean	Sigma	%Sigma	Mean	Sigma	%Sigma	Mean	Sigma	%Sigma	Mean	Sigma	%Sigma
Sc	10.02	1.33	13.30	11.27	1.27	11.24	21.50	2.05	9.53	20.31	3.28	16.14
Cr	243	64	26.34	200	40	20.13	156	17	10.74	171	78	45.45
Fe%	2.85	0.38	13.27	3.18	0.37	11.59	5.27	0.74	14.12	5.25	0.83	15.74
Co	15.28	1.62	10.57	16.98	2.22	13.07	20.14	5.94	29.51	23.86	5.65	23.66
Rb	51.31	7.32	14.26	47.76	6.29	13.17	103	13	12.67	72.04	12.09	16.79
Sb	0.643	0.246	38.32	0.529	0.165	31.22	0.578	0.182	31.49	0.523	0.143	27.34
Cs	3.34	0.50	14.96	2.72	0.45	16.41	26.21	4.21	16.07	5.04	0.93	18.38
Ba	224	43	19.39	425	172	40.37	362	126	34.92	414	192	46.39
La	18.68	1.63	8.71	20.47	2.01	9.82	44.45	4.86	10.94	31.08	4.51	14.51
Ce	37.28	3.76	10.08	41.67	3.93	9.44	89.27	11.74	13.15	62.20	9.91	15.93
Sm	3.32	0.36	10.84	3.63	0.37	10.16	6.71	0.75	11.12	5.37	0.75	13.94
Eu	0.740	0.070	9.46	0.802	0.089	11.09	1.38	0.16	11.46	1.24	0.19	15.40
Tb	---	---	---	0.550	0.097	17.61	0.821	0.142	17.24	0.719	0.138	19.21
Yb	1.54	0.15	9.80	1.69	0.18	10.43	2.67	0.27	10.15	2.37	0.31	13.17
Lu	0.265	0.024	9.05	0.291	0.030	9.83	0.470	0.040	8.61	0.409	0.047	11.56
Hf	2.65	0.36	13.45	2.76	0.13	11.10	5.03	0.44	8.82	4.15	0.69	16.62
Ta	0.673	0.100	14.87	0.740	0.101	13.68	1.48	0.19	12.63	1.22	0.27	21.76
Th	5.17	0.58	11.17	5.76	0.59	10.20	12.68	1.24	9.73	8.36	1.07	12.87
Ca%							5.81	2.43	41.82	7.66	3.97	51.86

Table 2. The distribution of ceramic type by chemical group.

Ceramic Type	Chemical Group I		Chemical Group II		Chemical Group III	
Grit Temper	TUV	ABC	TUV	ABC	TUV	ABC
Bichrome	0	0	10	1	0	0
Ring Bases	0	0	6	0	0	0
Knobby Ware	0	0	5	0	0	0
Monochrome	0	1	8	0	1	2
Flat Bases	1	0	4	0	7	4
Storage Jar	0	0	0	0	0	1
Rosette Relief	0	0	0	0	0	1
Total	1	1	33	1	8	8
Chaff Temper	TUV	ABC	TUV	ABC	TUV	ABC
Trays	10	10	0	0	0	0
Goblets	10	8	0	0	0	0
Bevel Rim Bowls	6	6	0	0	0	0
Total	26	24	0	0	0	0
Grand Total	52		34		16	

b. Activation Analysis Studies by the University of Maryland Nuclear and Environmental Chemistry Group

W. H. Zoller and G. E. Gordon

During the past year we and our students and research associates have made extensive use of the NBS Reactor in a variety of applications involving the use of instrumental neutron activation analysis (INAA) and neutron-capture prompt γ-ray activation analysis (PGAA). In order thoroughly to check out our analytical procedures, we had all members of our group analyze the new NBS coal standards (SRM 1632a and 1635) by INAA or other procedures and the standards were also analyzed by PGAA. Concentrations of many trace elements in it were about 10-fold lower than in SRM 1632a, bituminous coal. As shown in table I, our values are in generally excellent agreement with NBS certified or information values. A paper covering this work has been submitted for publication by *Analytical Chemistry*.

In our atmospheric studies, we have made use of INAA to analyze in-plant and plume samples from five copper smelters in Arizona. We were able to measure concentrations of about 40 elements. We find that particles released by copper smelters are a very rich source of chalcophile trace elements, some of which are toxic, e.g., Se, As, and Cd. The elemental concentration patterns of particles from the different smelters are so different that they provide a "fingerprint" that could be used to identify particles from specific plants in ambient air. We are also in the process of analyzing particles collected in plumes from a cement plant and a steel mill.

We have continued to study the compositions of particles in global circulation. For several years, we have been analyzing atmospheric particles collected during brief visits to the South Pole during Austral summers. During the past year we have analyzed substantial numbers of samples collected throughout the year at the South Pole. Preliminary interpretation of this more complete data set indicates that various groups of elements undergo different cyclical variations throughout the year, suggesting that they originate from different sources and are transported to the Pole via different global circulation patterns. There are very fragmentary indications that concentrations of a few elements at the Pole increase significantly after large volcanic eruptions. We are just initiating a long-term study (supported by NOAA) of the elemental compositions of particles collected in a global network of stations located in Hawaii, American Samoa, Barrow, Alaska and the South Pole.

Table I. Summary of Results for SRM 1632a and SRM 1635 and Comparison with NBS values

Element	SRM 1632a		SRM 1635	
	This Work	NBS[a]	This Work	NBS[a]
H (%)	3.7±0.1	-	3.96±0.03	-
B (ppm)	53±2	-	105±3	-
C (%)	71±4	-	59±3	-
N (%)	1.27±0.08	-	1.0±0.1	-
Na (%)	0.085±0.004	-	0.26±0.01	-
Mg (%)	0.13±0.03	-	0.10±0.02	-
Al (%)	2.94±0.13	3.07	0.30±0.03	0.32
Si (%)	5.8±0.1	-	0.52±0.02	-
S (%)	1.59±0.02	1.64	0.32±0.01	0.33
Cl (ppm)	790±20	-	26±2	-
K (%)	0.42±0.02	-	0.011±0.001	-
Ca (%)	0.23±0.02	-	0.55±0.02	-
Sc (ppm)	6.8±0.6	6.3	0.69±0.07	0.63
Ti (%)	0.161±0.004	0.175	0.020±0.002	0.02
V (ppm)	44±3	44±3	4.5±0.5	5.2±0.5
Cr (ppm)	34±2	34.4±1.5	2.3±0.2	2.5±0.3
Mn (ppm)	32±3	28±2	22±3	21.4±1.5

Table I. Continued

Element	SRM 1632a		SRM 1635	
	This Work	NBS[a]	This Work	NBS[a]
Fe (%)	1.16±0.03	1.11±0.02	0.23±0.01	0.239±0.005
Co (ppm)	6.5±0.2	6.8	0.59±0.06	0.65
Ni (ppm)	26±4	19.4±1	-	1.74±0.1
Zn (ppm)	31±6	28±2	7.5±2.2	4.7±0.5
Ga (ppm)	8.0±0.8	8.49	-	1.05
As (ppm)	10.2±0.5	9.3±1	0.7±0.4	0.42±0.15
Se (ppm)	2.6±0.3	2.6±0.7	0.98±0.09	0.9±0.3
Br (ppm)	41±4	-	1.6±0.3	-
Rb (ppm)	29±1	31	-	-
Sr (ppm)	84±9	-	129±14	-
Y (ppm)	5.8±0.5	-	-	-
Zr (ppm)	53±5	-	16±3	-
Cd (ppm)	0.21±0.03	0.17±0.02	-	0.03±0.01
In (ppb)	36±4	-	5±2	-
Sb (ppm)	0.60±0.09	0.58	0.14±0.01	0.14
I (ppm)	1.8±0.2	-	0.6±0.3	-
Cs (ppm)	2.0±0.3	2.4	0.046±0.005	-

Table I. Continued

Element	SRM 1632[a]		SRM 1635	
	This Work	NBS[a]	This Work	NBS[a]
Ba (ppm)	122±11	-	70±9	-
La (ppm)	18±2	-	2.1±0.3	-
Ce (ppm)	32±4	30	3.5±0.5	3.6
Nd (ppm)	12.1±0.4	-	1.4±0.2	-
Sm (ppm)	2.10±0.07[b]	-	0.25±0.01[b]	-
Eu (ppb)	550±30	540	61±7	64
Gd (ppm)	1.95±0.03	-	0.23±0.01	-
Tb (ppm)	0.36±0.12	-	-	-
Dy (ppm)	2.2±0.3	-	0.31±0.04	-
Yb (ppm)	0.98±0.08	-	0.14±0.02	-
Lu (ppb)	180±30	-	27±4	-
Hf (ppm)	1.55±0.08	1.6	0.27±0.04	0.29
Ta (ppb)	400±30	-	46±9	-
W (ppm)	0.6±0.2	-	-	-
Pb (ppm)	15±4	12.4±0.6	-	1.9±0.2
Th (ppm)	4.8±0.2	4.5±0.1	0.64±0.06	0.62±0.04
U (ppm)	1.2±0.1	1.28±0.02	0.21±0.05	0.24±0.02

[a] Data from NBS certificate of analysis. Values with no limits attached are information values only, i.e., not certified.

[b] PGAA value only (see text).

5. Facilities for Activation Analysis

a. Counting and Data Reduction

R. M. Lindstrom

The recently acquired Nuclear Data 6620 Nuclide Identification System has become the major component in data reduction for activation analysis. The modular software package supplied the manufacturers for activation analysis is an excellent base for future improvement. Testing has revealed a few weaknesses in the peak search routine supplied, so that for the most critical work the SUM program has been written to provide reliable net areas for well-resolved peaks with user control of the integration parameters.

Two new gamma-ray detectors have been acquired which will be invaluable for particular problems. An ion-implanted p-type Ge detector offers excellent resolution for all energies, and greatly improved efficiency for low and high energies when compared with existing Ge (Li) and planar detectors, respectively. A Ge (Li) well detector with nearly 4π geometry for a point source at the bottom of the well is most useful when samples of very low activity are to be counted.

b. Sample Rotator for the Thermal Column

R. M. Lindstrom

Sally H. Harrison

As part of an effort to measure the absolute sputtering yield of gold, a facility was constructed to allow irradiation of several samples in the identical average neutron flux in the ISNF cavity in the thermal column. A shaft whose axis is parallel to the flux gradient carries a disk on which samples are mounted. This spit assembly is driven from outside the reactor face by a small electric motor. The entire assembly will slide into the 1 5/8" access port to the cavity, and thus the rotator's capacity is restricted to four samples, 13 mm in diameter. Larger or more numerous samples could be accommodated by constructing a larger sample-carrying disk, which would necessitate removing blocks of graphite to insert samples.

The degree of flux homogeneity achieved is not known. In one experiment the ratio of specific activities of two gold standards irradiated together in this facility was 1.0008 ± 0.0006, where the uncertainty is the standard deviation based on counting statistics alone. Since the ratio includes terms for sample weight, decay, detector dead time, and pulse pileup we can only conclude that inhomogeneity has not been found to exceed 0.1%.

U-238 CAPTURE/U-235 FISSION CROSS SECTION RATIO IN THE ISNF

D. M. Gilliam, J. A. Grundl, V. Spiegel and C. E. Eisenhauer
(Nuclear Radiation Division)

and

C. W. Maddison and S. G. Carpenter
(Argonne National Laboratory, Idaho Falls, ID)

The preparation of the ENDF/B V compilation for the U-238 capture cross section presented inconsistencies in the experimental data which an accurate integral test could help to resolve. A collaborative experiment was planned which would utilize the NBS Intermediate Energy Standard Neutron Field (ISNF) and the activation foil counting and analysis expertise of the ANL (Idaho) Applied Physics Division.

The arrangement of the ISNF is shown in figure 1. The one-dimensional geometry and the simplicity of the composition have permitted the most rigorous kinds of transport calculations to be employed in the characterization of this neutron field. Figure 2 shows the details of the mounting arrangements for the activation foils. The results of four irradiations are given in table 1 along with details of foil identification, locations, and timing. The data presented in table 1 have been corrected for gradients within the ISNF test volume. The corrections were less than 2% in every case. The four runs listed in table 1 are denoted as the main run, the fission chamber run, the background run, and the self-shielding run. In the main run, two U-235 foils, two U-238 foils, and one thorium foil were activated. The background run was a repetition of the main run except that the U-235 fission source disks (shown in figure 1) were removed from the spherical cavity. The background response, due to epithermal and fast neutrons in the thermal column, is subtracted from the response observed in the main run to get the net ISNF response. The background-corrected results are given in the first column of table 2. Calculations of neutron self-shielding for the U-238(n,γ) reaction were made by ANL, and these corrections turned out to be large - about 10% for a 5 mil (0.13 mm) gold foil. The "self-shielding" run included a 5 mil foil, a stack of three

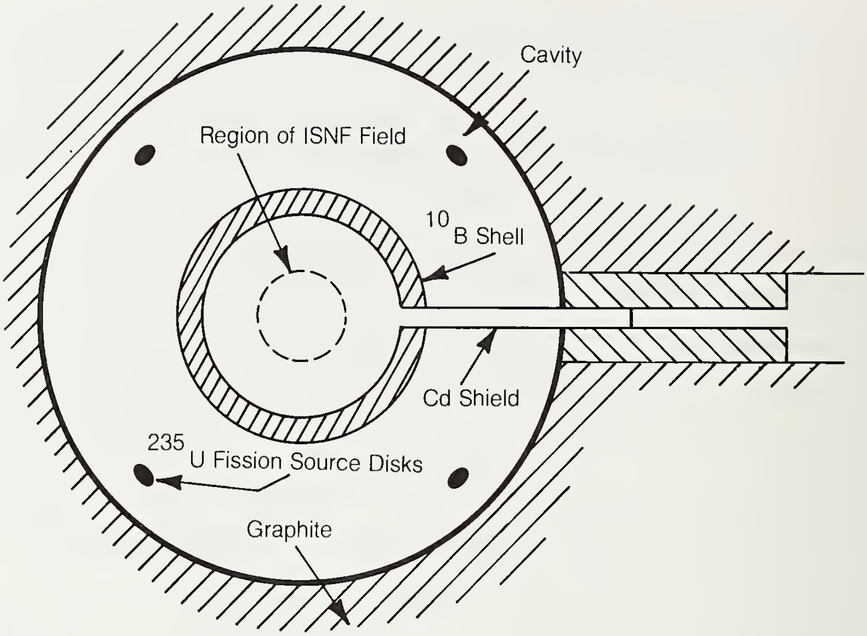

Figure 1. A schematic drawing of the ISNF spherical cavity.

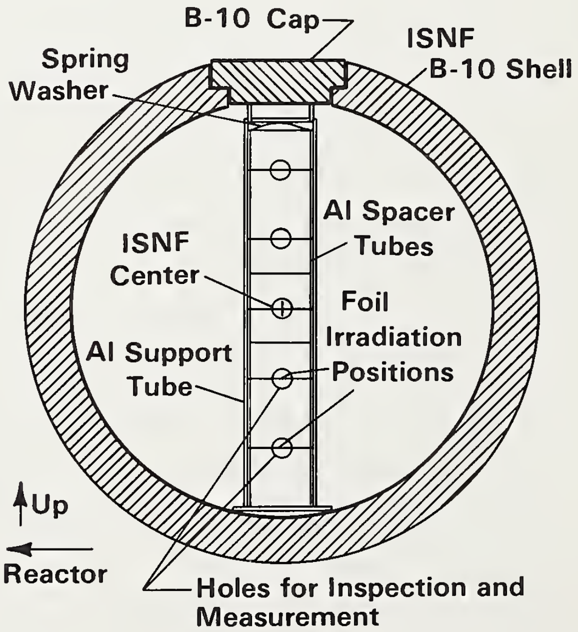

Figure 2. Foil mounting arrangement for the intermediate-energy standard neutron field (ISNF).

Table 1

Fission and Capture Rates for Four ISNF Runs
(not corrected for neutron self-shielding)

Foil or Deposit	Principal Isotope	Irradiation Location	Gradient-Corrected Fission or Capture Rate (f/sec. or c/sec. per mg of principal isotope	Random Error (%, 1σ)	Systematic Error (%, 1σ)
		Main Run 9/6/78	08:11:27 - 12:11:21 EDT		
8BNY	U-238	2 cm above center	437.4 c	0.70	1.6
5CXP	U-235	center	3494.0 f	0.62	1.5
8BNT	U-238	1 cm below center	440.9 c	0.71	1.6
5CXI	U-235	2 cm below center	3513.5 f	0.63	1.5
		Fission Chamber Run 9/5-6-78	21:44:43 - 01:40:37	EDT	
		(data corrected for 0.56% addition irradiation in long cooling period after high flux exposure)			
8BNV	U-238	top of chamber	433.3 c	0.68	1.6
5CXL	U-235	center of chamber	3440. f	0.64	1.5
5CXS	U-235	bottom of chamber	3447. f	0.64	1.5
25S-5-2	U-235	center of chamber	3415. f	0.50	1.6

Table 1 (continued)

Fission and Capture Rates for Four ISNF Runs
(not corrected for neutron self-shielding)

Foil or Deposit	Principal Isotope	Irradiation Location	Gradient-Corrected Fission or Capture Rate (f/sec. or c/sec. per mg of principal isotope)		Random Error (%, 1σ)	Systematic Error (%, 1σ)
		Background Run 9/5/78	15:13:27 - 19:13:21 EDT			
5CXQ	U-235	center	29.9	f	5.	___
8BNQ	U-238	1 cm below center	1.54	c	20.	___
		Self-Shielding Run 3/20/79	08:07:27 - 12:07:21 EDT			
O	U-238*	2 cm above center (top of stack)	452.8	c	0.7	1.6
AB	U-238*	2 cm above center (middle of stack)	450.1	c	0.7	1.6
AC	U-238*	2 cm above center (bottom of stack)	451.3	c	0.7	1.6
8BNP	U-238	1 cm above center	436.4	c	0.6	1.6
5CXG	U-235	center	3487.	f	0.6	1.5
L	U-238*	1 cm below center	464.1	c	0.7	1.5
5CXH	U-235	2 cm below center	3476.	f	0.6	1.5

*denotes 1 mil thickness; others 5 mils.

Table 2

Summary of U-238/U-235 Cross Section Ratio Measurements for the ISNF Field

U-238 Foil Type and Position	Capture/Fission Ratio and Random Error	Capture/Fission Ratio Corrected for Neutron Self-Absorption and Self-fission
stacked 1 mil foils, 2 cm above center	0.1324 ± 0.8% 0.1316 ± 0.8% 0.1320 ± 0.8%	----- ----- -----
average of stacked foils	0.1320 ± 0.6%	0.1427
1 mil foil, 1 cm below center isolated	0.1357 ± 0.8%	0.1406
5 mil foil 1 cm above center	0.1276 ± 0.7%	0.1429
5 mil foil 1 cm below center	0.1271 ± 0.8%	0.1424
5 mil foil 2 cm above center	0.1281 ± 0.8%	0.1435
average for 5 mil foils in closed ISNF	0.1276 ± 0.5%	0.1429
5 mil foil on top of fission chamber	0.1288 ± 0.8%	0.1443

Table 3. Estimated Uncertainties in the Cross Section Ratio Measurements

Source of Error	Estimated 1σ Limit (%)
σ_γ(U-238)/σ_f(U-235) Activation Foil Results	
Deposit mass and other minor errors in calibration against back-to-back fission chambers at ZPPR and AFSR.	1.2
Self-shielding correction	1.0
Combined Random Errors	0.72
Total Systematic Error	1.56
Total Random Error	0.72
Total Error	1.72

1 mil foils, and an isolated 1 mil foil in order to avoid having to make such a large correction and to obtain an experimental check on the calculated self-shielding corrections. The degree of agreement of the corrected results from all thicknesses of foil (second column of table 2) is a measure of the accuracy of the self-shielding corrections. The spread of the results is just over 2%. The uncertainty in the self-shielding correction for the weighted average of all the results is estimated to be ± 1.0%. This and other uncertainties are tabulated in table 3.

The U-238 capture to U-235 fission cross section ratio for the Intermediate-Energy Standard Neutron Field (ISNF) was determined experimentally to be

$$\sigma_\gamma(\text{U-238})/\sigma_f(\text{U-235}) = 0.1412 \pm 1.7\%$$

in good agreement with the calculated value of 0.1410 which was derived from ENDF/B IV cross sections and a 240 group discrete ordinates calculation.

CERTIFIED NEUTRON FLUENCE DOSIMETRY STANDARDS

V. Spiegel, E. D. McGarry, J. Grundl and R. A. Dallatore
(Nuclear Radiation Division)

A dosimetry program for surveillance of the fast fluence exposure of pressure vessels for light-water reactors has been established by the U. S. Nuclear Regulatory Commission. As part of the effort to develop a reference-data base for the program, NBS is under contract to the Commission to provide standard neutron field irradiations and calibration methodology.

A first step in establishing traceable calibrations of surveillance dosimetry methods is to insure interlaboratory consistency in measuring and evaluating fluence detectors. To accomplish this, NBS will periodically issue neutron fluence standards obtained from exposures of dosimeters to a certified neutron fluence in one of the NBS standard neutron fields. The fluence standards will be typical pressure-vessel activation-dosimeter materials (e.g. nickel, iron, uranium-238) and will be suitable for use with germanium-lithium or sodium-iodide gamma counting systems. The NBS will also serve to evaluate the neutron fluences reported by participating laboratories based upon the assigned neutron spectrum for the standard field.

Twenty-seven nickel foils that were irradiated to a known fluence in the NBS U-235 fission spectrum Cavity Fission Source[1] have been distributed internationally. To date the results of analyses by 17 laboratories have been received at NBS and the remaining are expected by late Fall, 1979. Each laboratory reports results on radioactivity, neutron fluence, and experimental uncertainties.

Similar distributions of counting standards of iron and fissionable materials are planned for 1979-1980.

PRECISION GAMMA-RAY AND X-RAY WAVELENGTHS

E. G. Kessler, Jr., R. D. Deslattes, W. C. Sauder
and A. Henins
(Center for Absolute Physical Quantities)

and

W. Schwitz
(University of Fribourg)

and

(Swiss National Science Foundation)

and

L. Jacobs
(IKS Leuven/SCK, Mol, Belgium)

A class of high resolution double crystal transmission spectrometers are used at NBS to measure wavelengths of gamma- and x-ray standards. The unique features of these instruments are: 1) crystals whose lattice spacings are calibrated by x-ray/optical interferometry, and 2) angle measuring interferometers calibrated by use of an optical polygon. The first of these features permits the connection of gamma- and x-ray wavelengths with optical wavelengths and the Rydberg constant, R_∞. The second of these features eliminates the need for an artifact angle standard or an assumed value for a particular wavelength. More experimental details are given in references 1, 2.

During the past year the analyses of measurements on Yb-169, Tm-170, and W Kα_1 x-ray have been completed. Wavelength and energy values for nine prominent reference lines in Yb-169, for the 84 keV line in Tm-170 and for the W Kα_1 x-ray line have recently been published.[3,4] The results are summarized in table 1. These lines together with previously published lines[2] in Au-198 and Ir-192 provide precise optically based wavelength standards in the 50 keV to 1.1 MeV range.

Also during the past year preparations were completed for an attempt at the measurements of the wavelength of the electron-positron annihilation radiation (511 keV). This line is narrowed by magnetically mixing the short lived singlet state with the longer lived triplet state and by thermalizing the positronium in a cryogenic He gas.[5] The positrons are produced in the radioactive decay of a Cu-64 10 kilocurie source.

A Cu source was irradiated in the NBS reactor and withdrawn into a transfer cask equipped with manipulators for inserting the source into the He dewar. The irradiation was troubled by two difficulties. The copper wire, although contained in an aluminum can, was in contact with the irradiation thimble water. A small amount of copper went into the solution so that the thimble water became slightly radioactive. Secondly, the mechanism used to load the source into the dewar failed so that insertion of the source into the dewar was impossible. The source and the transfer mechanisms have undergone some design changes and a new attempt at this measurement will be made in the near future.

A second generation transmission double-crystal spectrometer was also completed during the past year. This instrument differs from the original spectrometer in that it has a larger angular range, can measure radiation from a stationary source, and is completely controlled by a computer. The computer is interfaced to the spectrometer via a CAMAC system and the software programs are written in FORTRAN. The spectrometer has been calibrated and has demonstrated the capability of 0.1 ppm angle measurements.

The new spectrometer was first used to measure the K absorption edge of erbium which lies at approximately 57.5 keV. The interest in this measurement stems from the use of the erbium K edge as an energy standard and discriminant in the study of kaonic potassium by Lum and Wiegand.[6] The 6-5 transition in kaonic potassium is coincident with the Er K edge and these researchers have measured the mass absorption with the Er K edge and these researchers have measured the mass absorption coefficient of Er for this kaonic x-ray. The Er foils used in their measurement were sent to us for direct measurement. We determined the mass absorption coefficient as a function of energy in the region of the

Table 1. Wavelength and energy values for Yb-169 and Tm-170 gamma-rays and the W Kα_1 x-ray. σ_m is the measurement uncertainty and σ_T is the total uncertainty. Energies were obtained from wavelengths by use of the voltage wavelength conversion factor 1.2398520 x 10^{-6} eV·m.

	Wavelengths (pm)	Energies (keV)	σ_m (ppm)	σ_T (ppm)
^{169}Yb	19.642536	63.12077	1.33	1.34
^{169}Yb	13.244140	93.61514	1.23	1.25
^{169}Yb	11.293983	109.77987	0.42	0.47
^{169}Yb	10.490313	118.19018	1.52	1.53
^{169}Yb	9.4990577	130.52368	0.16	0.25
^{169}Yb	6.9963540	177.21402	0.23	0.30
^{169}Yb	6.2632112	197.95788	0.22	0.30
^{169}Yb	4.7489623	261.07851	1.21	1.23
^{169}Yb	4.0289264	307.73757	0.21	0.29
^{170}Tm	14.71543	84.25523	0.86	0.88
W Kα_1	20.90135	59.319233	0.89	0.90

K absorption edge. Because of the unique features of our spectrometer, the wavelength or energy scale is in terms of the Rydberg constant, R_∞. When the measured energy of the kaonic transition is compared to theoretical predictions, the mass of the kaon can be deduced. Lum and Wiegand estimate that a kaon mass value accurate to ∿ 80 ppm should be determined. A 150 keV tungsten target x-ray tube provided the continuum radiation for the absorption measurement. Absorption measurements with several different foil thicknesses have been recorded and final analyses of the data is nearing completion.

The new spectrometer has recently been moved to a 4 MeV electron Van de Graaf in order to measure high Z K x rays. The measurement of K x rays over a wide Z range will permit tests of accurate self consistent field calculations.[8] The spectrometer is completely installed at the Van de Graaf and a few initial measurements on Au K x rays have been made.

---

1. R. D. Deslattes, Proc. Int. School of Physics 'Enrico Fermi', Course 68 (1976) to be published. A more detailed manuscript on instrumentation and procedures is in preparation.

2. E. G. Kessler, Jr., R. D. Deslattes, A. Henins and W. C. Sauder *Phys. Rev. Lett.* 40, 171 (1978).

3. E. G. Kessler, Jr., L. Jacobs, W. Schwitz and R. D. Deslattes, *Nucl. Instr. and Meth.* 160, 435 (1979).

4. E. G. Kessler, Jr., R. D. Deslattes and A. Henins, *Phys. Rev.* A 19, 215 (1979).

5. W. C. Sauder and R. D. Deslattes, *Jour. Res. NBS* 71A, 347 (1967).

6. G. K. Lum and C. E. Wiegand, *Bull. Am. Phys. Soc.* 23, 64 (1978).

7. R. D. Deslattes, E. G. Kessler, Jr., L. Jacobs and W. Schwitz, *Phys. Lett.* 71A, 411 (1979).

8. See for example, K-N. Huang, M. Aoyagi, M. H. Chen, B. Crasemann and H. Mark, At. Data Nucl. Data Tables 18, 243 (1976) and references cited therein.

D. REACTOR OPERATIONS AND SERVICES

The NBSR continued its leadership as one of the best utilized research reactors in the country with 25 simultaneously operable facilities surpassing that of any other major facility. Operated round-the-clock by the smallest staff of any comparable reactor, it again produced an outstanding operating record. It supports many extensive and diverse programs carried out by more than 150 scientists and engineers from within and outside NBS. These programs range from the development of standard reference materials, neutron standards and dosimetry, trace analysis of foods and artifacts, the development of energy resources, and the use of neutron radiography as an NDE tool for the determination of the structure and properties of technologically important materials. In all, 18 NBS Divisions and offices, 27 federal agencies, industrial and national laboratories, and more than 24 universities depend on the NBS reactor for vital programs.

The upgrade of the reactor power to 20 MW is progressing. The higher power will greatly enhance reactor utilization and versatility. Arrangements for the long-term supply of nuclear fuel have been completed through use of Department of Energy facilities and contractors, and delivery should commence by December, 1979.

1. Reactor Operations

All aspects of reactor operations continued to be excellent. Once again, outstanding on-line performance, reactor utilization and fuel efficiency were achieved until the forced shutdown. A summary of overall statistics is presented in the following table for the period July 1, 1978-June 30, 1979.

NBSR OPERATING SUMMARY 1979

No. of days at 10 MW	280
On-line time at 10 MW	77%
Average U-235 burnup	52%
No. of Irradiations	2040
Hours of Irradiations	3020
Hours per Irradiation	1.5

2. Irradiation Services

Again tens of thousands of samples were irradiated involving many important and diverse programs. These include trace analysis of foods, drugs, and environmental samples, forensic investigation, development of energy resources and minerals, and the analysis of archaeological treasures and moon rock samples. In addition, over half of the standard reference materials issued by the Bureau have been characterized using the reactor. The work in these areas at the NBSR surpasses that of any other research reactor in the U.S.

Many important new programs have been initiated. They include: the establishment of a national Environmental Sample Bank which will provide real-time monitoring data for pollutant trend evaluation as well as allow for more precise measurements in the future; the development of state-of-the-art measurement techniques and standards for nuclear material safeguards; image enhancement of underdeveloped photographic film; and finally the analysis of waste materials being fed to animals for their toxic effect on the food chain.

E. SERVICE PROGRAMS

ACTIVATION ANALYSIS PROGRAM OF THE FOOD AND DRUG ADMINISTRATION AT THE NBSR

J. T. Tanner and W. B. Stroube, Jr.
(Food and Drug Administration, Washington, DC)

The activation analysis unit of the Food and Drug Administration (FDA) is located at the National Bureau of Standards in the Reactor Building. Neutron activation analysis (NAA) has been used by the FDA for trace metal analysis of foods, drugs, hair, laundry aids, and cosmetics. The service of this group is available to anyone within the FDA both in the headquarters laboratory and in the field. The following projects are representative of the work of the NAA unit.

1. Aid to Field Laboratories

In support of FDA field operations, impurities from a boxcar load of oats were analyzed. Apparently the load of oats was introduced into the boxcar before it had been cleaned thereby resulting in contamination. The samples were analyzed by three different analytical methods; neutron activation analysis, electron excited x-ray fluorescent, and fluoride diffusion with detection by ion selective electrode. Results by neutron activation are given below.

The suspected contaminent was Na_2SiF_6. Activation analysis was used to determine the elemental composition of the samples and to determine the amount of each element present. Silicon was not detected by NAA.

Pure Na_2SiF_6 should have an elemental composition of 24.5% Na, 60.6% F and 14.9% Si. The percentage composition obtained by NAA for the Na_2SiF_6 standard sample is in excellent agreement with the calculated composition. Samples 79-193-304 and 79-193-451 appear to have the same major elemental composition as the Na_2SiF_6 (including a trace of aluminum). The results in the table are averages of several samples and the low value for 79-193-304 reflects one subsample which had an unusually low F content.

Sample 79-164-001 contained Ca and Cl (determined by XRF). It did not contain Na, F, or Si. Although the identity of this sample is not known, it is definitely not Na_2SiF_6.

The results were combined with the other analytical results and conveyed to the Field Laboratory. They in turn were able to contribute the cause of numerous cattle deaths and low milk production to the feeding of oats contaminated with Na_2SiF_6 to the cattle.

Elemental Determination by NAA

Sample	Na*	F*	Al*
Na_2SiF_6	24.5%	60.3%	83 ppm
79-193-304	24.5%	46.8%	66.5 ppm
79-193-451	25.9%	69.9%	308 ppm
79-164-001	ND	ND	975 ppm

*Averaged values.

2. Liver Copper Response of Swine Fed Graded Levels of Copper

The FDA proposed in 1973 to limit supplemental copper for swine diets to 15 ppm. Recognizing the problem in identifying dietary copper sources, it was desirable to establish a dietary tolerance above a level expected to result from feed ingredients plus supplemental copper. The literature suggested this would be approximately 40 to 60 ppm. A dose-response study was undertaken to establish the dietary copper level which would elevate copper residues in swine liver.

In the first study conducted in this project, one hundred-twenty weanling, crossbred pigs were used in a dose response study to determine the effect of 7.5, 15, 30, 60, 120, and 240 ppm dietary copper on copper and iron stores in selected tissues. Dietary copper levels of 7.5, 15, 30, and 60 ppm had no significant effect on copper and iron content of liver and kidney. However, 120 and 240 ppm dietary copper increased liver copper 5 and 18 fold and decreased liver iron 2 and 3 fold respectively. A fit of liver copper and iron data to linear plateau models gave an inflection point of 60 ppm dietary copper. These data indicate that an elevation of dietary copper above 60 ppm will cause a change in the normal liver copper and iron concentrations. However, additional data points are needed to more accurately determine the inflection point.

The objectives of the current study were to (a) determine the maximum level of dietary copper which will not result in markedly increased liver and kidney copper, (b) obtain tissue residue data in feeder pigs withdrawn from supplemental dietary copper at 75 pounds body weight, and (c) establish a data base for some mineral levels in swine tissue.

A total of 108 pigs were used in this study. Feed intakes were measured and diets analyzed periodically for copper content. At sacrifice the liver and left kidney were removed, weighed, homogenized, and sampled for mineral analysis. These tissue samples were analyzed by activation analysis for Cu, Fe, Zn, Mn, Mg, Al, Se, and Co. The results are currently being tabulated.

PHOTOGRAPHIC IMAGE INTENSIFICATION BY NEUTRON ACTIVATION OF GOLD TONED NEGATIVES

C. D. Bond
(Naval Research Laboratory, Washington, DC)

A gold-toning neutron-activation process has been developed at NRL for the purpose of intensifying or amplifying the contrast in extremely weak images in photographic negatives where the exposure level may be as low as 1.5% of optimum. Such contrast enhancement of photoreconnaissance and intelligence films allows the recovery of image information which may be taken under adverse lighting or obscured in the shadows and which might otherwise be lost by conventional methods using chemicals/photographic or densitometer/computer techniques. This process can also be extremely valuable in the enhancement of weak images in other disciplines that use photographic film as detectors, e.g., low intensity spectroscopy, faint images in astronomy, and radiation dose reduction in diagnostic medical x rays by reduction of required exposure.

When standard commercial silver halide film is underexposed and chemically developed with resulting atomic silver concentration of $\leq 10^{-5}$ g/cm^2, ordinary chemical enhancement and light transmission techniques are inadequate for satisfactory image formation. An image-silver density of 10^{-5} g/cm^2, however, can still contain a large amount of information (i.e., $\sim 10^7$ silver-grains/cm^2. Several nuclear and ion beam techniques can detect silver in light substrates in the 10^{-6} to 10^{-9} g/cm^2 range which is well below normal optical densitometer sensitivity. However, this sensitivity is not fully utilized because presently all contrast enhancement techniques, whether by nuclear or computer methods, reach a limiting condition imposed by the grain statistics and signal to noise ratio as the image density approaches the fog level.

All of the present nuclear enhancement techniques employ some procedure for causing the silver grains in the photographic negative to emit charged particles or other ionizing radiation. The intensity of the induced activity is proportional to the density of the silver image. Both radiochemical toning[1,2] and direct neutron activation[3,4] have been used to make the silver grains emit electrons. The radioactive image can be rendered visible and enhanced by placing the activated film in pressure contact with a new unexposed film which is exposed by the ionizing radiation rather than light (i.e., contact autoradiography). Thus the electrons from each grain in the original weak image can be made to cause numerous grains to be made developable in the autoradiographic. This is the amplification or enhancement mechanism.

The radiochemical toning techniques can be quite hazardous and require trained radiochemists. Also, the autoradiographic exposure times require typically seven (7) to eighty (80) hours. Direct neutron activation of the silver image, without toning, has several disadvantages. The principle difficulty is that the two silver isotopes which are produced by neutron activation have half-lives that are either too short (2.4 min.) for easy reproducible control of exposure or too long (252 days) for convenient exposure.

The gold-toning neutron-activation process, developed at NRL, differs significantly from the previously described nuclear methods of photographic image enhancement in two important ways: (a) A non-radiochemical toning solution and complexing wash are used to gold plate the image silver grains before activation. This procedure eliminates all hazards of handling radioactive solutions. (b) The neutron activation of the gold image is far superior to either direct activation of the silver image or radiochemical toning of the silver image both with regard to the efficiency of image activation and the speed and ease of producing autoradiographs. The reason for this can be seen in table 1.

The method involves three main steps: (A) gold toning of the negative, (B) neutron activation of the gold image and (C) image intensification by autoradiographic reproduction.

The photographic negative to be enhanced is placed in a gold chloride and ammonium thiocyanate toning solution. Here, the gold is plated out onto the silver grains in the image. The film must be washed in an ammonium thiocyanate complexing solution to remove excess non-image gold deposited in the emulsion.

The film is then placed in the NBS thermal neutron port for activation. The neutron flux at this port is ∿ 10^{13} neutron/s/cm^2 and consists of ∿ 98% thermal neutrons. The film can be adequately activated in 1 to 5 minutes with no detectible damage to the emulsion or backing. The neutron capture by the gold and silver components of the image produce the radioisotopes Au-198, Ag-108 and Ag-110. The film pack is allowed to cool for ∿ 1 hour to dissipate the 2.42 min.

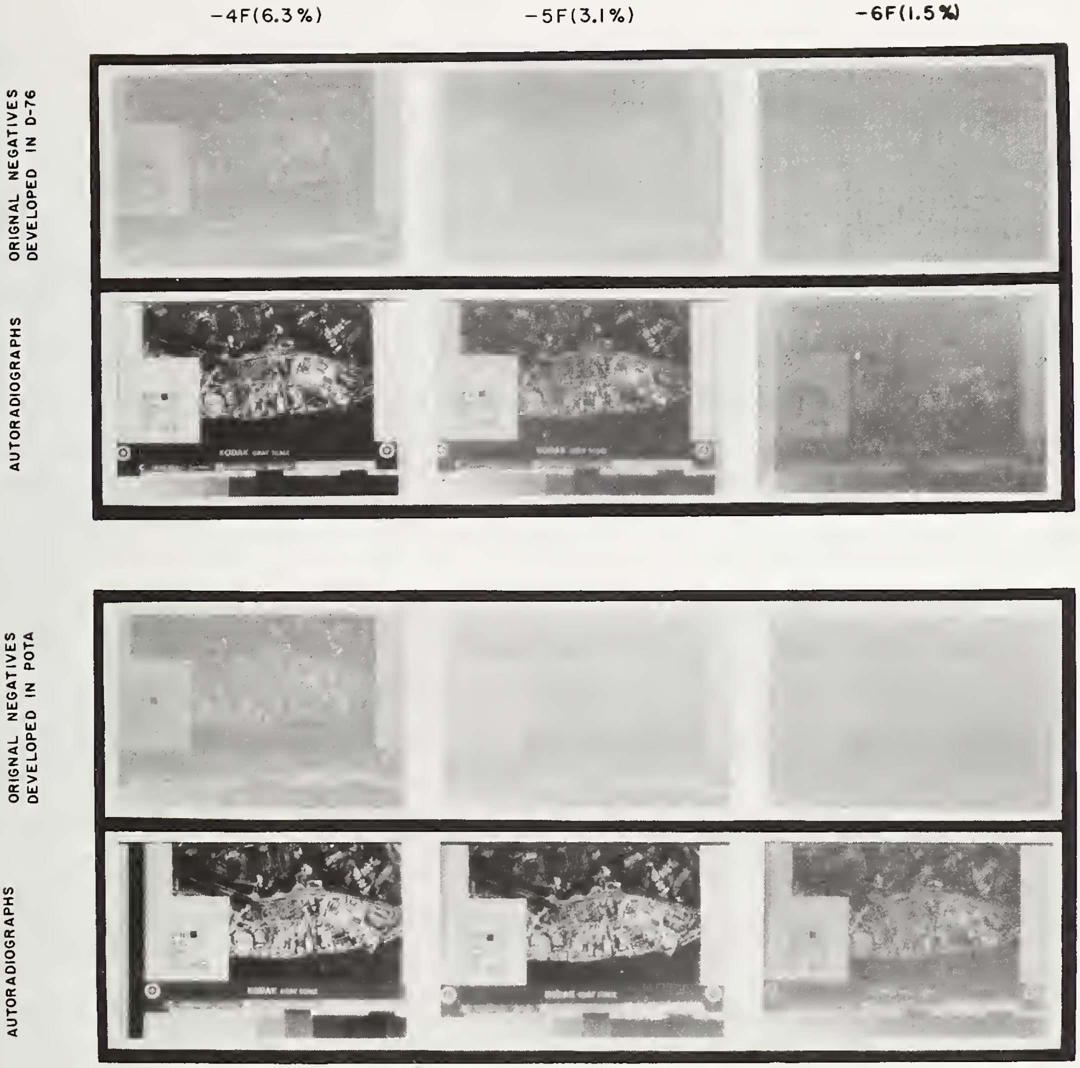

Figure 1. The first and third rows show optimized prints made from the original negatives taken at 4F, 5F and 6F stops below optimum exposure. The second and third rows show optimized prints made from the corresponding autoradiographs.

Ag-108 activity. The gold Au-198 has a 2.69 day half-life and is now the dominant β active component. The Ag-110 has a 252 day half-life and ∿ 1/1000 of the activity of the gold.

An intensified reproduction of the β active gold image is obtained by placing the film in pressure contact with an unexposed autoradiographic film. The two films must have their emulsion surfaces in intimate contact and under ∿ 2 lb/in^2 pressure in order to obtain good resolution in the reproduction. The exact autoradiograph exposure time required will depend on the optical density of the original image, the level of contrast amplification desired and on the lapsed time from neutron activation. The average normal times range from 5 minutes to ∿ 1 hour if autoradiography is carried out within a few hours of activation. Additional autoradiographs and exposures can be conveniently produced from original negatives for several days for ease of image optimization. Because of the relatively high specific activity induced in the gold toned image as compared to the radiochemical toning, it is possible to get good results using rapid process autoradiograph film. Generally, x-ray film is used to achieve useful optical density in the autoradiographs.

Some examples of this process are shown in figure 1. Our test image is composed of an aerial view of the NRL Laboratory, a tribar resolution target at left and a gray scale at bottom. This standard scene is photographed with correct optimum exposure and then succeeding photographs are taken at 1 through 6 F-stops below optimum. (At 6 F-stops below normal the film is receiving only 1.5% of normal illumination and the image density is quite near the base fog level. Such images,

Table 1. Neutron activation of gold toned film

REACTION	1(%)	$\sigma A^{(BARNS)}$	$T_{1/2}$	RADIATION
$^{107}Ag(n,\gamma)^{108}Ag$	51.8	45.0	2.42 M	β1 (96%) 1.64 meV γ (.632, .618, .511, .433) meV
$^{109}Ag\ (n,\gamma)^{110}Ag$	48.2	3.2	252 D	β1 (31%) 0.529 meV β2 (67%) 0.087 meV γ (1.5, 1.38, .937, .884, .657) meV
$^{197}Au\ (n,\gamma)^{198}Au$	100	98.8	2.7 D	β1 (99%) 0.96 meV γ 0.411 meV

depending on the developer, are generally not visible to densitometers or to the eye.) The top row shows a set of optimized prints made from the original negatives (developed in D-76) using high contrast paper and exposed to obtain the best contrast and detail obtainable from each negative. (Only the lowest three exposures are shown.) The second row shows identically made optimized prints, but made from the corresponding autoradiographic film.

The third row also shows a set of optimized prints made from the original negative but developed in POTA; a special wide latitude developer giving a better signal to noise ratio near the base fog level.[5] (A weak image is detectable even at the -6F-stop level.) The fourth row again shows a set of optimized prints made from the corresponding autoradiographic films.

The contrast intensification is clearly apparent in all of the autoradiographs. However, at the -6F-stop level (1.5% of optimum exposure) the image density in the original negatives is generally below or near the sensitivity limit of both analytical or scanning densitometers. For example, at the -6F-stop level in the POTA original negative, densitometers can detect only one gray scale step above the base fog, while six steps above the base fog can be detected in the corresponding autoradiograph. This difference can also be seen in the two lower right comparison prints.

---

1. M. Thackray, D. Roman, E.L.R. Hetherington and H. H. Brian, *International Journal of Applied Radiation and Isotopes*, 23, 79 (1972).
2. Barbara S. Askins, *Applied Optics*, 15, No. 11, 2860 (1976).
3. Eugene Ostroff, *Science*, 154, 119 (1966).
4. R. M. Chatters and Camille Jacobs, *Photographic Applications in Science, Technology and Medicine*, p. 26 (1970).
5. Marilyn Levy, *Photographic Science and Engineering*, 11, No. 1, 46 (1967).

ATF'S ACTIVATION ANALYSIS PROGRAM

W. Kinard
(U.S. Treasury Department, Rockville, MD)

Neutron activation analysis (NAA) continues to be a valuable tool in the crime laboratory. Its ability to analyze microscopic amounts of evidentiary material non-destructively is a distinct asset in those cases where evidentiary materials must be preserved for courtroom presentation.

During FY79, 205 case-related samples were analyzed by NAA. These samples consisted of inks, hair, bullet leads, paints, glass, paper, unknown metal alloys and soils.

In addition to our use of NAA for forensic purposes, wines and distilled spirits were examined for their trace elemental content using the NAA technique. This work was done in connection with our regulatory enforcement program of monitoring the composition of alcohol containing products.

During the fiscal year 1979, the following types of evidentiary materials were examined by NAA. The irradiation time shown represents the total reactor utilization for samples of each type.

Sample/Type	Number of Samples	Total Irradiation Time (Hours)
Hair	140	186
Paint	10	42
Inks	20	10
Explosives	8	4
Glass	6	1
Bullet Lead	85	30
Paper	30	2

On-going research using NAA includes the examination of printing inks and pencil entries for the purpose of identifying the product, its manufacturer, and the date of production.

The value of examining paints and human hair is being critically assessed. Collection of additional data with regards to these materials will be reported in mid 1980.

USGS ACTIVATION ANALYSIS PROGRAM

J. J. Rowe, J. W. Morgan and P. A. Baedecker
(U.S. Geological Survey, Reston, VA)

The Radiochemistry, Reston project applies activation analysis to geochemical studies related to 1) behavior of volatiles to study petrogenetic modeling; 2) partitioning coefficients to study petrologic history; 3) characterization of magmatic and tectonic setting; 4) magma chamber eruptive sequences; 5) mechanisms of ore deposition; 6) alteration studies; 7) origin of coals and peats; 8) compilation of a comprehensive baseline of coal compositions; and 9) trace element studies to assist other geologic or geochemical investigations.

1. Instrument Neutron Activation Analysis

The Geological Survey has an ongoing program of automated INAA, which provides data for 24 to 30 elements in 3000 to 4000 rock, mineral, and coal samples per year (Baedecker, 1979). Thermal neutron irradiations are utilized for special problems using the JEEP-II reactor in Kjeller, Norway. During the past year we have extended the INAA techniques to the analysis of microscopic metal grains from dendritic meteorites weighing from 5 to 100 micrograms. We are able to determine 11 element including As, Au, Ga, and Ir at the ppm level to study the factors controlling the distribution of siderophile elements in meteorites, and to look for trace element mobility in meteorites which have been reheated due to shock (Baedecker *et al.*, 1979).

2. Radiochemical Neutron Activation

Ultratrace determination of siderophile elements (Au, Ge, Ir, Ni, Os, Pd, Re) and volatile elements (Ag, Bi, Cd, In, Sb, Se, Te, Tl, Zn) in lunar and terrestrial rocks.

a.

Lonar Crater, India. The Lonar Crater is the only known terrestrial impact crater in basalt. Impact glasses are significantly depleted relative to parent basalts in Re and Se, and the loss is directly correlated with degree of shock. Volatilization under oxidizing conditions appears to be responsible for the depletion, and is probably peculiar to impacts on planets with Earth-like atmospheres (Morgan, 1978).

b.

Australites are aerodynamically-shaped glass of probable impact origin, which are found over wide areas of Australia. The similarity in trace element pattern between a siderophilerich australite and the "cometary" component in lunar soil 61220 tends to suggest an origin for australites by cometary impact (Morgan, 1978).

c.

Lunar orange and black glasses. The orange soil at the Apollo 17 site, found by Harrison Schmitt (now U.S. Senator for Arizona) is composed almost entirely of orange glass spheres. It is underlain by black soil, which is made up of black glass spheres identical in composition to the orange glasses, but devitrified by more gradual cooling. The origin of these glasses has generally been thought to be a lava fountain similar to those seen in terrestrial volcanoes. The siderophile element pattern found in the glasses resembles a type IIB iron meteorite, however, and suggests that the orange and black glasses may have been formed either by impact into a lava lake, or by a lava fountain induced by impact superheating (Morgan and Wandless, 1979a).

d.

Lunar breccias 73215 and 73255. These Apollo 17 melt rocks are the result of multiple impacts during the early history of the Moon, culminating in the large event, which excavated the basin now forming Mare Serenitatis. The fine-grained matrix material (aphanite) from both breccias has identical siderophile patterns apparently derived from the Serenitatis impacting body. Inclusions (or "clasts") of a different rock type (anorthositic gabbro) all have a distinctly different siderophile pattern introduced by a much earlier impact (Morgan and Petrie, 1979).

e.

Terrestrial upper mantle. Direct sampling of the Earth's mantle has not been carried out by drilling, but fragments of the mantle are found in kimberlite pipes and in basalts. The rather high and uniform abundances of highly siderophile elements found in a world-wide sampling of mantle rocks are in approximately the same proportions as in chondritic meteorites. Because these elements have very high metal/silicate partition coefficients, they would have been quantitatively removed by formation of the Earth's core. We infer that a further addition of primitive material (perhaps 0.5% to 1% of the Earth's mass) was added after core separation (Morgan and Wandless, 1979b).

3. Group Separations of Rare Earth Elements (REE) in Rocks and Minerals

a.

Hydrothermal minerals. The distribution of REE in such simple oxygen-containing minerals as anhydrite ($CaSO_4$), barite ($BaSO_4$), and siderite ($FeCO_3$) appears to be controlled very strongly by the ionic radius of the major cation. Abundances of REE in galena (PbS) are very low (La, Sm ≃ 0.5 ppb, remaining REE below detection limits), and reflect the very weak chalcophilic (≡ sulfur-loving) tendencies of REE (Morgan and Wandless, 1979c).

b.

Rocks and separated silicate minerals. The large INAA program of service analysis for U.S.G.S. geologists is supplemented by radiochemical analyses in those cases where the REE abundances are very low (i.e. less than about 10 times abundances in chondritic meteorites), or where the available sample weights are very small.

---

1. Baedecker, P. A. "The INAA program of the U.S. Geological Survey (Reston), in Computers in Activation Analysis and Gamma-Ray Spectroscopy," *Proceedings of the American Nuclear Society Topical Conference* (to be published).

2. Baedecker, P. A., Morgan, J. W., and Goldstein, J. I., "Siderophile element fractionation in the initial phase of the Knyahinya chondrite," *Lunar and Planetary Science X,* part 1, 54-56 (1979).

3. Morgan, J. W., "Lonar crater glasses and high magnesium australites: Trace element volatilization and meteoritic contamination," *Proc. Lunar Planet. Sci. Conf. 9th,* (1978).

4. Morgan, J. W. and Petrie, R. K., "Breccias 73215 and 73255: Siderophile and volatile trace elements," *Proc. Lunar Planet. Sci. Conf. 10th,* (to be published).

5. Morgan, J. W. and Wandless, G. A., "Siderophile elements match IIB iron meteorite pattern," *Proc. Lunar Planet. Sci. Conf. 10th* (to be published).

6. Morgan, J. W. and Wandless, G. A. "Terrestrial upper mantle: Siderophile and volatile trace elements," *Lunar and Planetary Science X,* 855-857 (1979).

7. Morgan, J. W. and Wandless, G. A., "Rare earth element distribution in some hydrothermal minerals: Evidence for crystallographic control," (to be published).

F. STAFF ROSTER

REACTOR RADIATION DIVISION

566

R. S. Carter, Chief
T. M. Raby, Deputy Chief
E. C. Maxwell, Admin. Officer*
E. Simms, Receptionist
L. Sprecher, Secretary*

Division Staff

R. Casella
B. Mozer
F. Shorten

Reactor Operations
T. M. Raby
J. F. Torrence
C. Freedman, Secy.

<u>Reactor Operators</u>

R. Beasley
M. Bell
N. Bickford
H. Brake
J. Browning
D. Cea
A. Chapman
H. Dilks
W. Mueller
D. Nelson
J. Ring
R. Stiber
D. Wilkinson
B. Young

Engineering Services
J. H. Nicklas

<u>Mechanical Design</u>

E. Guglielmo
J. Sturrock

<u>Electronics</u>

R. Conway
J. Darr
R. Hayes

Neutron S-S Physics
J. J. Rush
S. Long, Secy.

<u>Crystallography</u>

E. Prince
A. Santoro
C. Choi (GW)
A. Tudgay (1/2)
D. Fravel (1/2)

Metal Hydrides and
<u>Molecular Materials</u>

J. Rowe
A. Cinquepalma
D. Fravel (1/2)
W. Rymes (1/2)
G. Fish (PD)
C. Glinka

<u>Biological Materials</u>

A. Wlodawer
A. Tudgay (1/2)

Magnetic and
<u>Amorphous Materials</u>

J. Rhyne
H. Alperin (GW)
N. Koon (GW)
R. Williams (GW)
J. Lynn (GW)

<u>Metastable Materials</u>

H. Prask (GW)
S. Trevino (GW)
W. Rymes (1/2)

Neutron Radiography
D. A. Garrett

M. Dorsey
M. Ganoczy
T. Cheng

*Part-time
PD - Postdoctoral
GW - Guest Worker

NON-RRD NBS STAFF LOCATED AT REACTOR

Division 354

- P. Cassidy
- K. Eggert
- T. Hobbs
- F. Moore
- J. Shubiak

Division 532

- M. Baier
- R. A. Dallatore
- C. Eisenhauer
- D. Gilliam
- J. A. Grundl
- E. McGarry
- I. G. Schroder
- R. Schwartz
- W. Slater
- V. Spiegel

Division 501

- H. Berger

Division 506

- D. Becker

Division 551

- J. Bailey
- J. Blackman
- C. Blundell
- B. Carpenter
- R. Fleming
- T. Gills
- S. Harrison
- J. Koskoris
- R. Lindstrom
- G. Lutz
- J. Maples
- J. Mitchell
- T. Mitlehner
- L. Pilione
- R. Zeisler

GUEST WORKERS AND COLLABORATORS

Division 520

- R. Deslattes
- A. Henins
- L. Jacobs
- E. Kessler
- W. Sauder
- W. Schwitz

Division 522

- R. Dove
- H. Marshak

Division 532

- R. Caswell
- A. Wasson

Division 541

- R. Kavanagh
- J. Kelly
- T. Madey

Division 544

- S. Greer
- D. Tsai

STAFF ROSTER

Division 553

H. Rook

Division 563

R. Bowen
C. Han

Division 562

B. Christ
J. Early

Division 564

R. Reno

Division 741

P. Brown

Argonne National Laboratory

R. Armani
T. Brun
R. Dunlap
H. Flotow
O. Hinks
S. Susman
J. Viccaro

Battelle, N. W.

W. Nicholson

Brookhaven National Laboratory

D. Richter

Federal Bureau of Investigation

R. Asbery
D. B. Davies
J. Haverkost
J. W. Kilty
E. Mitchell
C. Peters
J. P. Riley
M. Graves

Food and Drug Administration

W. Stroube, Jr.
J. Tanner
D. Daly

Harry Diamond Laboratory

C. Heimbach

NASA-Langley Research Center

R. Buckingham

National Gallery of Art

B. Miller
C. Parkhurst
J. Olin

National Institutes of Health

D. Davies
R. Frank
W. Hagins
W. Robinson
J. Weinstein

Naval Air Defense Command

M. Stellabotte
W. Williams

Naval Research Laboratory

C. Bond
P. D'Antonio
A. Ehrlich
D. Forester
M. Fatemi
R. Kaplan
J. Karle
N. Koon
F. Kuchas
K. Murray
V. Rath
L. Pecoia

STAFF ROSTER

Picatinny Arsenal

C. S. Choi
H. J. Prask
S. Trevino

Carnegie Institute of Washington

B. K. Kothari

Smithsonian Institution

M. Blackman
T. Chase
J. Mishara
S. O'Dell
J. Olin
L. Zacherman

U. S. Geological Survey

P. Baedecker
J. Morgan
J. J. Rowe

U. S. Treasury Department

J. M. Hoffman
W. Kinard

American University

J. Ferrick
R. A. Segnan

Colorado State University

C. E. Patton

Howard University

G. A. Ferguson

Iowa State University

R. Shelton

Israel Institute of Technology

Y. Segal

Massachusetts Institute of Technology

B. Averbach

Reed College

W. Parker

University of Antwerp

K. Michel

University of Arizona

R. Salemme
P. Weber

University of Alabama

J. Segrest

University of Arkansas

D. Wolfman
T. Rolnick

University of California (Lawrence Livermore Laboratories)

J. Browne
S. Hankins

University of Chicago

E. Anders
R. Wolf

University of Houston

S. Moss

STAFF ROSTER

University of Maine

H. Patterson

University of Maryland

D. Anderson
G. Barley
W. Cunningham
M. Failey
M. Germani
I. Gokmen
G. Gordon
J. Lynn
I. Olmez
J. Phelan
J. C. Roy
A. Sigleo
M. Small
W. Walters
J. Weber
J. Winer
M. Yiu
W. Zoller

University of Missouri (Rolla)

W. James

State University of New York (Stoneybrook)

H. Herman

University of Paris

B. Le Meindre

University of Pittsburgh

S. Sankar
W. Wallace
R. Buttera

University of Rhode Island

S. Pickart

Virginia Poly Technic Institute

R. Peterson
G. Gibbs

University of Wisconsin

J. Hinkley
H. Yu
J. Perpeso

Allied Chemical Corporation

G. Leibowitz
A. Maeland

B-K Dynamics

N. Chesser

Fedders Air Conditioning Company

W. Simpkins

General Electric Company

F. Luborsky
J. Walter

IBM Corporation

D. Bouloin

Metronic, Inc.

P. Slarstad

Monsanto Research Corporation

W. Brotherton

OLDELFT Corporation

D. Bracher

Sandia Corporation

J. Harris

STAFF ROSTER

Wilson Greatbach, Ltd.

R. Steinbring

Nuclear Energy Center, Mol, Belgium

A. Fabry

G. PUBLICATIONS

COLLABORATIVE PROGRAMS

ABBUNDI, R., RHYNE, J. J., SWEGER, D. M., and SEGNAN, R., "Magnetic Relaxation Phenomena in Dy-Sc Alloys", *Physical Review B*, 18 3313 (1978).

ALPERIN, H. A., and GILLOMOR, W. R. PICKART, S. J. and RHYNE, J. J., "Magnetization and Neutron Scattering Measurements on Amorphous $NdFe_2$", *J. Appl. Phys* 50 1958 (1979).

ALPERIN, H. A., PICKART, J., RHYNE, J. J., "Small Angle Neutron Scattering from Rare Earth Iron Alloys", *J. Applied Crystallography* 11 648-49 (1978).

CASELLA, R. C., "Neutron Scattering from Coherent Admixtures of Phonons with Libronic Excitations of Dictomic Imprintion", Phys. Rev. B (to be published).

CHOI, C. S., PRASK, H. J., and TREVINO, S. F., "Nondestructive Investigation of Texture by Neutron Diffraction", *J. Appl. Cryst.*, (to be published).

CHOI, C. S., PRINCE, E., "1, 2, 3, Triaminoguanidinium Nitrate by Neutron Diffraction", *Acta Cryst.* B35, 761-3 (1979).

DOMBECK, T. W., LYNN, J. W., WERNER, S. A., BURN, T., CARPENTER, J., KROHN, V., RINGO, R., "Production of Ultracold Neutrons Using Doplar-Shifted Bragg Scattering and an Intense Pulse Neutron Spallation Source", *Nuclear Instruments and Methods*. (to be published).

FISH, G. E., RHYNE, J. J., BURN, T., VICCARO, P. J., NIARCHOS, D., DUNLAP, B. D., SHENOY, G. K., SANKAR, S. G., WALLACE, W. E. "Neutron Scattering Studies of Hydrides of the Laves Phase Rare Earth Compounds RFe_2", *The Rare Earths in Modern Science and Technology, Vol. 2*, Plenum Press, (to be published).

FISH, G. E., RHYNE, J. J., SANKAR, S. G., WALLACE, W. E., "Effect of Hydrogen on Sublattice Magnetization of Laves Phase Rare Earth Iron Compounds", *J. Appl. Phys.* 50, 2003 (1979).

FORESTER, D. W., KOON, N. C., SCHELLERG, J. H., and RHYNE, J. J., "Amorphous YFe_2 - A Concentrated Spin Glass", *J. Appl. Phys.* (to be published).

FORESTER, D. W., KOON, N. C., SCHELLING, J. H., RHYNE, J. J., "Spin-Glass and Magnetic Blocking Transitions in Amorphous YFe_2", *Solid State Commun.*, 30, 177-180 (1979).

PUBLICATIONS

GARRETT, D. A., "ASTM Recommended Practice for Thermal Neutron Radiography of Materials", American Society for Testing and Materials (to be published).

GLINKA, C. J., ROWE, J. M., LUBOWITZ, G. G., MAELAND, A., "Neutron Crystal-Field Spectroscopy of $\mathrm{CeD}_{2.12}$", *J. Phys. C* (to be published).

KOON, N. C. and RHYNE, J. J., "RPA Theory of Magnetic Excitations in Rare Earth-Transition Metal Compounds: Application to ErCo_2 and ErFe_2", *Intl. Journal of Magnetism* (to be published).

KOON, N. C. and RHYNE, J. J., "Excited State Spin Waves in ErFe_2", *Solid State Commun. Vol. 26,* pp 537-540 (1978).

LYNN, J. W. and SHELTON, R. N., "Neutron Scattering Studies of Magnetic Superconductors", *J. Magnetism and Magnetic Materials* (to be published).

LYNN, J. W., MONCTON, D. E., PASSELL, L., THOMLINSON, W., "Magnetic Correlations and Crystal Field Levels in the Superconductor $(\mathrm{Ce}_{\,3}\mathrm{Ho}_{27})\mathrm{Ru}_2$", *Phys. Review B* (to be published).

LYNN, J. W., GLINKA, C. J., "Magnetic Properties of the Superconducting Alloy System $(\mathrm{Ce}_{1-c}\mathrm{Ho}_c)\mathrm{Ru}_2$-A Neutron Scattering Study", *Journal of Magnetism and Magnetic Materials* (to be published).

LYNN, J. W., SHELTON, N., "Neutron Scattering Studies of Crystal Field Excitation in $(\mathrm{RE})\mathrm{Mo}_6\mathrm{Se}_8$", *J. Appl. Phys.* 50 1984 (1979).

PRINCE, E., CHOI, C. S., "Ammonium Azide." *Acta Cryst.* B35, 761-3 (1979).

PRINCE, E., WLODAWER, A., SANTORO, A., "Flat-Cone Diffractometer Utilizing a Linear Position-Sensitive Detector", *J. Appl. Cryst.* 11, 173-178 (1978).

PLACIOUS, R. Ç., GARRETT, D. A., BERGER, H., KASEN, M. B., "Dimensioning Flaws in Gas Pipe Welds By Radiographic Methods", (to be published).

RHYNE, J. J., "Amorphous Magnetic Rare Earth Alloys", *Handbook on the Physics and Chemistry of Rare Earths,* CH 16, (1979).

ROWE, J. M., RUSH, J. J., HINKS, D. G., SUSMAN, S., "Neutron Scattering Study of the Dynamics of $(\mathrm{KCN})_{0.5}(\mathrm{KBr})_{0.5}$", *Phys. Rev. Letters* (to be published).

PUBLICATIONS

RHYNE, J. J., and KOON, N. C., "Ground State Excitations in $HoCo_2$", *Intl. Journal of Magnetism* (to be published).

RHYNE, J. J., and KOON, N. C., "Magnetic Excitations in Rare Earth Laves Phase Iron Compounds", The Rare Earths in Modern Science and Technology, Vol. 2 (to be published).

RHYNE, J. J., FISH, G. E., SANKAR, S. G., W. E., "Magnetic Properties of Laves Phase Rare Earth Hydrides", *Journal De Physique* C5-209 (1979).

RHYNE, J. J., LYNN, J. W., LUBORSKY, F. E., and WALTER, J. L., "Spin Excitation in Amorphous Transition-Metal Boron Glasses", *J. Appl. Phys.* 50, 1583 (1979).

RUSH, J. J., and ROWE, J. M., "Neutron Quasielastic Scattering Study of ND_4^+ Orientational Fluctuations in B-Phase Nd_4Br", *J. Chem Phys* 69 2928-2930 (1978).

SANTORO, A., WLODAWER, A., "Absorption Correction for Weisenberg Diffractometers", *Acta Cryst.* (to be published).

SANTORO, A., MIGHELL, A., RODGERS, J., "Lattice Relationships: The Determination of Matrices That Will Relate Any Given Pair of Lattices", *Acta Crystallographica* (to be published).

SANTORO, A., ROTH, R. S., MINOR, D., "Neutron Powder Diffraction Study of Ta_2WO_8", *Acta Cryst. B* (to be published).

SANTORO, A., MAREGIC, M., ROTH, R. S., MINOR, D., "Neutron Powder Diffraction Study of The Structure of $CeTaO_4$, CeN_6O_4, and $NdTaO_4$", *Journal of Solid State Chemistry* (to be published).

SANTORO, A., "Use of Derivative Lattices in the Indexing of Powder Patterns", *Acta Crystallographica* (to be published).

SHORTEN, F. J., "NBS Reactor: A Summary of Activities, July 1977 to June 1978", *NBS Technical Note 995,* (1979).

SLEENBERGER, C., RUSH, J., "Neutron Scattering Study of the Methyl Group, Reorientations and the Low Temperature Phase Transition in $(CH_3)_2SF_2$", *J. Chem Phys.* 70 50-56 (1979).

TREVINO, S. F., RYMES, W. H., "A study of Methyl Reorientation in Solid Nitromethane by Neutron Scattering", *J. Chem Phys.* (to be published).

PUBLICATIONS

TREVINO, S. F., "An Observation of One-Dimensional Reorientational Tunnel Splitting of the Ground and First Excited State in a Low Barrier System: Solid Nitromethane", *J. Chem Phys.* (to be published).

TREVINO, S. F., PRINCE, E., HUBBARD, C. R., "Refinement of the Structure of Solid Nitromethane", *J. Chem Phys.* (to be published).

WLODAWER, A., SEGREST, J. P., CHANG, B. H., CHIONETTE, R. and WEINSTEIN, J. N., "High Density Lipoprotein Recombinants: Evidence for a Bicycle Tire Micelle Structure Obtained by Neutron Scattering and Electron Microscopy", *FEBS Letters* (to be published).

WLODAWER, A., "Studies of Ribonuclease-A by X-ray and Neutron Diffraction", *Acta Crystallographica B* (to be published).

INDEPENDENT PROGRAMS

BARNES, I. L., GRAMLICH, J. W., DIAZ, M. G., and BRILL, R., Possible Change of Lead Isotope Ratios in the Manufacture of Pigments: A Fractionation Experiment, Archaelogical Chemistry II, 273 (1978).

BLACKMAN, M. J., "The Mineralogical and Chemical Analysis of Banesh Period Ceramics from Tal-e-Malyan, Iran," Proceedings of the 19th International Symposium on Archaeometry and Archaeological Prospection, London, U. K., (to be published).

CAPAR, S. G., TANNER, J. T., FRIEDMAN, M. H., and BOYER, K. W., "Multi-element Analysis of Animal Feed, Animal Wastes, and Sewage Sludge," *Environmental Science and Technology*, 12, 785-790 (1978).

CARPENTER, B. S., SAMUEL, D., WASSERMAN, I., and YUWLER, A., The $^{17}O(n,\alpha)^{14}C$ Reaction as a Tool for Determining the Location and Rate of Turnover of Monoamines in the Brain", (to be published).

CARPENTER, B. S., D'AGOSTINO, M. D., and YULE, H. P., Editors, "Computers in Activation Analytical Analysis and Gamma-Ray Spectroscopy", (to be published).

CARPENTER, B. S., PILONE, L. J., SCHRODER, I. G., ROE, J. W. and SANATANI, S., "Evaluation of Reactor Trace-Etch Power Monitor," Proceedings of the Conference "Measurement Technology for Safeguards and Materials Control," (to be published).

FAILEY, M. P., ANDERSON, D. L., ZOLLER, W. H., GORDON, G. E., and LINDSTROM, R. M., "Neutron Capture Prompt Gamma Ray Activation Analysis for Multi-Element Determination in Complex Samples," (to be published).

FLEMING, R. F., and BICKFORD, N. A., "Silicon Irradiation Facilities in the NBS Reactor," *Neutron Transmutation Doping in Semiconductors*, J. M. Meese, ed., (1979).

GILLS, T. E., GALLORINI, M., "The Determination of Trace Elements in New Food Grain SRM's Using Neutron Activation Analysis, *J. of Radioanal. Chem.*, 46, 21-25, (1978).

GREENBERG, R. R., "Trace Element Characterization of the NBS Urban Particulate Matter Standard Reference Material by Instrumental Neutron Activation Analysis, (to be published).

PUBLICATIONS

GREENBERG, R. R., GALLORINI, M., and GILLS, T. E., "Cadmium Analysis by Radiochemical Neutron Activation Analysis," *Environmental Health Perspectives*, 28, 1 (1979).

KESSLER, E. G., JR., JACOBS, L., SCHWITZ, W., and DESLATTES, R. D., "Precise γ-ray Energies from the Radioactive Decay of ^{170}Tm ^{169}Yb", *Nucl. Instr. and Meth.* 160, 435 (1979).

KESSLER, E. G., JR., DESLATTES, R. D., and HENINS, A., "Wavelength of the W $K\alpha_1$ X-ray Line", *Phys. Rev. A* 19, 215 (1979).

DESLATTES, R. D., KESSLER, E. G., JR., JACOBS, L., and SCHWITZ, W., "Selected X-ray Data for Comparison with Theory," *Phys. Lett.* 71A, 411 (1979).

KAMPS, L. TROTTER, W. J., YOUNG, S. CARSON, L. J., ROACH, J. A. G., SPHON, J. A., TANNER, J. T., MCMAHON, B., "Polychlorinated Quadraphenyls Identified in Rice Oil Associated with Japanese Yusho Poisoning," *Bulletin of Environmental Contamination and Toxicology*, 20, 589-91 (1978).

LINDSTROM, R. M., "Measuring Trace Elements in Semiconductors: Methods and Pitfalls," (to be published).

LINDSTROM, R. M., and FLEMING, R. F., "Optimized Measurement of Aluminum in High-Purity Silicon," *Proc. 3rd Int. Conf. Nucl. Methods in Env. and Energy Res.*, (1979).

LINDSTROM, R. M., HARRISON, S. H., and HARRIS, J., "Accurate Calibration of Gold Film Standards by Neutron Activation and Gravimetry," *J. Appl. Phys.*, 49, 5903 (1978).

ROOK, H. L., MOODY, J. R., PAULSEN, P. J., and RAINS, T. C., "Stability of Elemental Components in a Multitrace-Element Water Standard," *Proceedings of Symposium on Environmental Chemistry and Cycling Processes*, D. C. Adriano and I. Lehr Brishbin, Jr., eds, (1978).

SIMPSON, R. E., SHUMAN, F. G. D., BARATTA, E. J., and TANNER, J. T., "Population Dose Commitment Associated with Various Radionuclides in Foods," (to be published).

SORAN, P. D., LABAUVE, R. J., EISENHAUER, C. M., GEORGE, D. C., "Neutronic Analysis of the NBS Intermediate-Energy Standard Neutron Field (ISNF), *Trans Am Nuc. Soc.* 32, 777 (1979).

PUBLICATIONS

SCHWARTZ, R. B., "NBS Reference Neutron Fields for Personnel Dosimetry Calibration" *"Proceedings of the Seventh DOE Workshop on Personnel Neutron Dosimetry,"* (to be published).

TANNER, J. T. and BARATTA, E. J., "Radionuclides in Foods, The Food and Drug Administration Program," *Proceedings of the TVA Workshop on Factors Affecting Power Plant Waste Heat Utilization,* (to be published).

ZEISLER, R., LUX, F., SEIDENBERGER, H., SCHONENBERGER, H., BECK, W., "Studies on the Distribution of Platinum in Tumor-Bearing Rats After the Application of Platinum Coordination Complexes Used in Cancer Chemotherapy", *Proc. Internation Symposium on Nuclear Activation Techniques in the Life Sciences,* (1978).

NBS-114A (REV. 9-78)

U.S. DEPT. OF COMM.
BIBLIOGRAPHIC DATA SHEET

1. PUBLICATION OR REPORT NO.
NBS Tech. Note 1117

2. Gov't. Accession No.

3. Recipient's Accession No.

4. TITLE AND SUBTITLE
NBS Reactor: Summary of Activities
July 1978-June 1979

5. Publication Date
April 1980

6. Performing Organization Code

7. AUTHOR(S)
F. J. Shorten, Ed.

8. Performing Organ. Report No.

9. PERFORMING ORGANIZATION NAME AND ADDRESS

NATIONAL BUREAU OF STANDARDS
DEPARTMENT OF COMMERCE
WASHINGTON, DC 20234

10. Project/Task/Work Unit No.

11. Contract/Grant No.

12. SPONSORING ORGANIZATION NAME AND COMPLETE ADDRESS *(Street, City, State, ZIP)*
Same as block 9.

13. Type of Report & Period Covered
Final

14. Sponsoring Agency Code

15. SUPPLEMENTARY NOTES

☐ Document describes a computer program; SF-185, FIPS Software Summary, is attached.

16. ABSTRACT *(A 200-word or less factual summary of most significant information. If document includes a significant bibliography or literature survey, mention it here.)*

This report summarizes all those programs which depend on the NBS reactor. It covers the period from July 1978 through June 1979. The programs range from the use of neutron beams to study the structure and dynamics of materials through nuclear physics and neutron standards to sample irradiations for activation analysis, isotope production, radiation effects studies, neutron radiography, and nondestructive evaluations.

17. KEY WORDS *(six to twelve entries; alphabetical order; capitalize only the first letter of the first key word unless a proper name; separated by semicolons)*

Activation analysis; crystal structure; diffraction; isotopes; molecular dynamics; neutron; neutron radiography; nondestructive evaluation; nuclear reactor; radiation.

18. AVAILABILITY ☒ Unlimited

☐ For Official Distribution. Do Not Release to NTIS

☒ Order From Sup. of Doc., U.S. Government Printing Office, Washington, DC 20402

☐ Order From National Technical Information Service (NTIS), Springfield, VA. 22161

19. SECURITY CLASS (THIS REPORT)
UNCLASSIFIED

20. SECURITY CLASS (THIS PAGE)
UNCLASSIFIED

21. NO. OF PRINTED PAGES
236

22. Price
$6.00

USCOMM-DC

U. S. GOVERNMENT PRINTING OFFICE : 1980 311-046/52

NBS TECHNICAL PUBLICATIONS

PERIODICALS

JOURNAL OF RESEARCH—The Journal of Research of the National Bureau of Standards reports NBS research and development in those disciplines of the physical and engineering sciences in which the Bureau is active. These include physics, chemistry, engineering, mathematics, and computer sciences. Papers cover a broad range of subjects, with major emphasis on measurement methodology and the basic technology underlying standardization. Also included from time to time are survey articles on topics closely related to the Bureau's technical and scientific programs. As a special service to subscribers each issue contains complete citations to all recent Bureau publications in both NBS and non-NBS media. Issued six times a year. Annual subscription: domestic $17; foreign $21.25. Single copy, $3 domestic; $3.75 foreign.

NOTE: The Journal was formerly published in two sections: Section A "Physics and Chemistry" and Section B "Mathematical Sciences."

DIMENSIONS/NBS—This monthly magazine is published to inform scientists, engineers, business and industry leaders, teachers, students, and consumers of the latest advances in science and technology, with primary emphasis on work at NBS. The magazine highlights and reviews such issues as energy research, fire protection, building technology, metric conversion, pollution abatement, health and safety, and consumer product performance. In addition, it reports the results of Bureau programs in measurement standards and techniques, properties of matter and materials, engineering standards and services, instrumentation, and automatic data processing. Annual subscription: domestic $11; foreign $13.75.

NONPERIODICALS

Monographs—Major contributions to the technical literature on various subjects related to the Bureau's scientific and technical activities.

Handbooks—Recommended codes of engineering and industrial practice (including safety codes) developed in cooperation with interested industries, professional organizations, and regulatory bodies.

Special Publications—Include proceedings of conferences sponsored by NBS, NBS annual reports, and other special publications appropriate to this grouping such as wall charts, pocket cards, and bibliographies.

Applied Mathematics Series—Mathematical tables, manuals, and studies of special interest to physicists, engineers, chemists, biologists, mathematicians, computer programmers, and others engaged in scientific and technical work.

National Standard Reference Data Series—Provides quantitative data on the physical and chemical properties of materials, compiled from the world's literature and critically evaluated. Developed under a worldwide program coordinated by NBS under the authority of the National Standard Data Act (Public Law 90-396).

NOTE: The principal publication outlet for the foregoing data is the Journal of Physical and Chemical Reference Data (JPCRD) published quarterly for NBS by the American Chemical Society (ACS) and the American Institute of Physics (AIP). Subscriptions, reprints, and supplements available from ACS, 1155 Sixteenth St., NW, Washington, DC 20056.

Building Science Series—Disseminates technical information developed at the Bureau on building materials, components, systems, and whole structures. The series presents research results, test methods, and performance criteria related to the structural and environmental functions and the durability and safety characteristics of building elements and systems.

Technical Notes—Studies or reports which are complete in themselves but restrictive in their treatment of a subject. Analogous to monographs but not so comprehensive in scope or definitive in treatment of the subject area. Often serve as a vehicle for final reports of work performed at NBS under the sponsorship of other government agencies.

Voluntary Product Standards—Developed under procedures published by the Department of Commerce in Part 10, Title 15, of the Code of Federal Regulations. The standards establish nationally recognized requirements for products, and provide all concerned interests with a basis for common understanding of the characteristics of the products. NBS administers this program as a supplement to the activities of the private sector standardizing organizations.

Consumer Information Series—Practical information, based on NBS research and experience, covering areas of interest to the consumer. Easily understandable language and illustrations provide useful background knowledge for shopping in today's technological marketplace.

Order the **above** *NBS publications from: Superintendent of Documents, Government Printing Office, Washington, DC 20402.*

Order the **following** *NBS publications—FIPS and NBSIR's—from the National Technical Information Services, Springfield, VA 22161.*

Federal Information Processing Standards Publications (FIPS PUB)—Publications in this series collectively constitute the Federal Information Processing Standards Register. The Register serves as the official source of information in the Federal Government regarding standards issued by NBS pursuant to the Federal Property and Administrative Services Act of 1949 as amended, Public Law 89-306 (79 Stat. 1127), and as implemented by Executive Order 11717 (38 FR 12315, dated May 11, 1973) and Part 6 of Title 15 CFR (Code of Federal Regulations).

NBS Interagency Reports (NBSIR)—A special series of interim or final reports on work performed by NBS for outside sponsors (both government and non-government). In general, initial distribution is handled by the sponsor; public distribution is by the National Technical Information Services, Springfield, VA 22161, in paper copy or microfiche form.

BIBLIOGRAPHIC SUBSCRIPTION SERVICES

The following current-awareness and literature-survey bibliographies are issued periodically by the Bureau:

Cryogenic Data Center Current Awareness Service. A literature survey issued biweekly. Annual subscription: domestic $25; foreign $30.

Liquefied Natural Gas. A literature survey issued quarterly. Annual subscription: $20.

Superconducting Devices and Materials. A literature survey issued quarterly. Annual subscription: $30. Please send subscription orders and remittances for the preceding bibliographic services to the National Bureau of Standards, Cryogenic Data Center (736) Boulder, CO 80303.

U.S. DEPARTMENT OF COMMERCE
National Bureau of Standards
Washington, D.C. 20234

OFFICIAL BUSINESS

Penalty for Private Use, $300

POSTAGE AND FEES PAID
U.S. DEPARTMENT OF COMMERCE
COM-215

SPECIAL FOURTH-CLASS RATE
BOOK